7
Particle Formulation in Spray Fluidized Beds

Mirko Peglow, Sergiy Antonyuk, Michael Jacob, Stefan Palzer, Stefan Heinrich, and Evangelos Tsotsas

7.1
Introduction

Chapter 6 has shown that particles with desired properties can be produced by spray drying. In spray drying, the formation of the particles is a result of evaporation of the solvent from a solution or suspension. Product quality depends on the properties of the materials used, the operating conditions, and – to a certain extent – also on the equipment design.

Instead of spraying the droplets into an otherwise empty device, one can also spray them onto fluidized particles. In this way, a large family of spray fluidized bed formulation processes is obtained. Since these are wet processes, they are intimately coupled to, and strongly dependent on drying. Similarly to spray drying, product quality depends on material properties, operating conditions and equipment design. This creates, on the one hand, numerous opportunities for manipulating product properties in the desired direction. On the other hand, due to the large number of interacting involved parameters, it makes process design difficult. Even the observation and characterization of the particle system pose serious challenges.

Recent progress in experimental methods for observation and characterization of the particle system were presented in Chapter 5 of Volume 2 of this series. As for design methods, it has been pointed out, in Chapter 6 of Volume 1 of this series, that population balance equations can be used. However, such equations contain kinetic terms for birth, growth and death of particles, which must be reliably known for practical application. Moreover, they are continuous, macro-scale representations that – by definition – cannot directly account for micro-scale physics.

It is, therefore, easy to understand that the goal of the present chapter is not to offer a complete theory of spray fluidized bed processes – which does not yet exist – but to provide an overview of the processes and the opportunities that they offer, highlighting some recent advances. First, general principles will be discussed and terminology concerning agglomeration, granulation and coating will be defined in Section 7.2. Then, the influences of material properties, operating conditions and apparatus

Modern Drying Technology Volume 3: Product Quality and Formulation, First Edition.
Edited by Evangelos Tsotsas and Arun S. Mujumdar.

design will be treated with the help of selected examples in Sections 7.3, 7.4 and 7.5, respectively. The discussion of the influence of material properties (Section 7.3) will focus on why particles adhere to each other, how strong they become, how they break, and how primary particle properties can be considered in population balance modeling. Section 7.4 will exemplify the influence of operating parameters on the properties of particles produced by granulation. Section 7.5 will first identify aspects of apparatus design that can have a serious influence on product quality. This general discussion will then be exemplified by analyzing the influence of apparatus design on the residence time distribution of the solids, which, in turn, has an influence on, for example, deactivation of ingredients or particle size distribution (PSD). In a second example, we will show that different PSDs can be obtained even in devices that – at first glance – look like perfectly mixed vessels. Finally, discrete particle modeling (DPM) will be introduced as a promising method for connecting apparatus design to the process and the product. Concerning this connection, DPM is not the only possible method. Apart from the already mentioned population dynamics, empirical approaches and stochastic discrete models are also possible. The former will be treated in Section 7.6 with an example of aroma encapsulation, the latter in Section 7.7, focusing on the unique potential of discrete Monte Carlo simulations to explain the influence of drying on the kinetics of spray fluidized bed agglomeration. Finally, Section 7.8 will give a short summary and an outlook.

7.2
General Principles of Particle Formulation in Spray Fluidized Beds

Various definitions and names are used, in the scientific literature and in industrial applications, for spray fluidized bed processes and for the products which are manufactured using these processes. To clarify the terminology, Fig. 7.1 is used here. Figure 7.1 distinguishes between agglomeration, granulation and coating by means of schemes for the underlying principles and the resulting product structures.

Agglomeration is, in terms of population balances, an aggregation that combines small primary particles to give larger structures (Fig. 7.1a). A binding mechanism is necessary for agglomeration to happen. In the simplest case, sprayed water (or solvent) dissolves the surface of the primary particles. Collisions between the particles create liquid bridges, which can – due to the dissolved material – be transformed to solid bridges by drying. Weak solidified bridges are broken by further collisions, whereas those which are strong enough survive and provide the final product. If the primary particles are not soluble, binder must be added to the sprayed liquid. Further adhesion and bridge formation mechanisms are possible and will be discussed in Section 7.3.1.

In granulation (Fig. 7.1b), the atomized liquid spreads on the surface of fluidized particles and creates, depending on the thermal conditions and material properties, a more or less uniform liquid layer, which dries and solidifies. Repetition leads to successive layering of solidified shells and, finally, to an onion-like structure. The process, which is a growth process, starts with small particles (seeds) produced

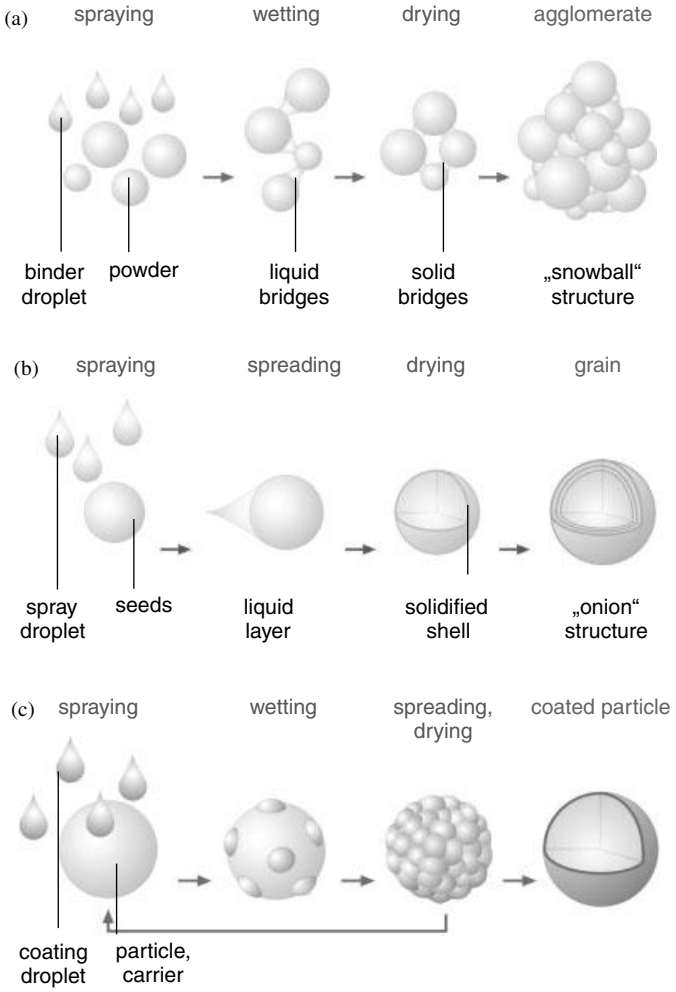

Fig. 7.1 Basic principles of spray fluidized bed processes: (a) agglomeration, (b) granulation (layering), (c) coating.

internally (by particle breakage or attrition, or by droplets dried during their flight from the atomization nozzle to the bed – the so-called overspray) or externally (by sieving-milling-circuits that recycle undersized or milled oversized fractions). Consequently, both seeds and granulated particles consist of the material dissolved in the spray. The properties of particles produced by layering granulation are compared to the properties of agglomerates in Tab. 7.1.

Coating (Fig. 7.1c) is essentially the same as layering granulation, with the difference being the placing of a more or less thin layer of another material on fluidized cores (carrier particles). The coating can increase the stability of the core during storage, prevent the uptake of moisture or the loss of volatiles, mask taste or

Tab. 7.1 Properties of particles produced by agglomeration or granulation.

Property	Agglomeration	Granulation
absence of dust	good	good
free flow	good	excellent
dosing	good	good
re-dispersion	good	good
instant behavior	excellent	
solubility		good
tabletting	easy	
porosity	high	low to very low
bulk density	low	high
surface	open	rather closed
hygroscopicity		reduced
sphericity	medium	high
PSD	rather wide	rather narrow
abrasivity	rather high	low

odor, or adapt the surface structure, appearance and solubility. Typically, the spray droplets are smaller, the viscosity of the spray liquid is lower, and the fluidization conditions are more turbulent in coating than in layering granulation. Both processes compete with agglomeration, because droplets can dry after their deposition on particles, or they can form liquid bridges. The transition between agglomeration and layering is usually described by the so-called Stokes criterion, which will be discussed in Section 7.7.

A possibility to deposit large amounts of coating material in a short period of time is provided by the so-called powder layering or dry coating process. Here, the coating material is fed in powder form and distributed on the (much larger) carrier particles, as shown in Fig. 7.2. Layer uniformity and the avoidance of agglomeration of powder particles with each other are important product quality issues that require special apparatus design.

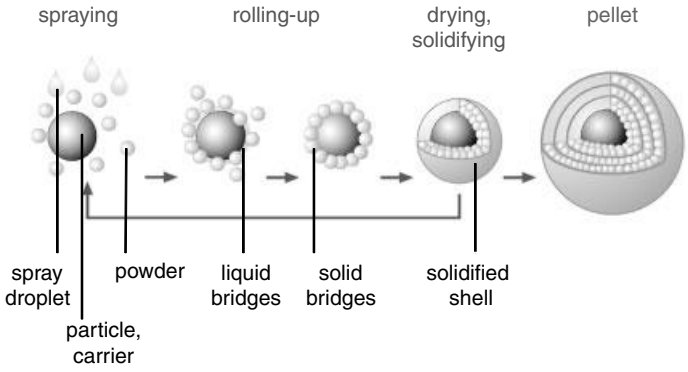

Fig. 7.2 Basic principle of powder layering (dry coating).

Tab. 7.2 Grains vs. powder vs. liquids.

Grains compared to Powders	Powdery Solids compared to Liquids
less dust	less volume
improved flowing properties	less weight
easy to dose	no sedimentation or settlement
easy to transport	easy to ship
decreased handling hazards	

All the discussed processes can, in principle, also be operated by spraying a melt instead of a solution or suspension. Hot melt coating, granulation or agglomeration has, if possible in terms of the materials to be used, energetic advantages. The reason is that solid phase formation takes place by cooling the melt, without the need to evaporate water or another solvent. In the case of coating, higher amounts of material can be deposited, and carrier particles sensitive to water or solvent can be treated.

Irrespective of how they have been produced, granular solids have some typical advantages in comparison to powders, and powdery solids have typical advantages in comparison to liquids. These advantages are summarized in Tab. 7.2.

Despite Tab. 7.2, powders can be the preferred product form for various applications, due, for example, to their high volume-specific surface area and the resulting high reactivity. Even ultra-fine powders can be produced in spray fluidized beds. For this purpose, one follows Fig. 7.1c. However, the coating is created with the sole purpose of its subsequent *in situ* destruction by particle–particle collisions. The material created by attrition is now the real product of the process, which is carried out of the fluidized bed by the gas and can be collected in a cyclone or in filter bags. The core particles are carriers for the coating and, simultaneously, the promoters of its destruction, so that they have to be heavy and rigid. Metallic carrier particles can be heated by wall contact or by induction, so that the creation of ultra-fine powder can be combined with its thermal treatment.

7.3 Influence of Material Properties

7.3.1 Adhesion Mechanisms and Mechanical Strength of Agglomerates

Composition and process conditions determine the nature of the adhesion forces holding the primary particles of agglomerates together. The following adhesion forces are relevant for agglomeration during drying:

- Van der Waals forces increasing after deformation of plastic particle surfaces,
- Capillary forces generated by liquid bridges between particles,
- Viscous forces in sinter bridges between amorphous particles.

The different adhesion forces are highly dependent on the material properties which are a function of the material structure. Thus differences in material structure and properties are explained before the three mentioned adhesion principles are discussed.

7.3.1.1 Material Structure and Properties

In view of adhesion principles and their dependence on the material properties one can distinguish mainly two different groups of water-soluble materials: amorphous and crystalline substances (Palzer, 2005, 2009). In an amorphous matrix the molecules are arranged statistically (as in a liquid), whereas the molecules in crystalline structures are highly ordered in repeated three-dimensional geometrical patterns. The two substance groups are characterized by different material properties such as hygrocapacity, hygrosensitivity, and mechanical properties. The hygrocapacity quantifies the ability to bind water by absorption into the molecular matrix and adsorption on the free surface area. The hygrosensitivity of a material describes to what extent its viscosity is affected by the absorbed water. In terms of hydrocapacity and hydrosensitivity both material groups exhibit completely different behavior.

While increasing the relative humidity of the surrounding air, crystalline materials do not absorb significant quantities of water. Only a limited amount of crystal water is embedded in the molecular matrix. Once a substance-specific relative air humidity (or water activity) is reached, the crystals dissolve layer by layer. In contrast, amorphous water-soluble substances absorb significant quantities of water when exposed to an increasing relative humidity of the surrounding air. The amount of absorbed water is a function of the water activity that can be described by various types of isotherm equations (Guggenheim, Anderson and de Boer (GAB), Brunnauer, Emmett and Teller (BET), see Weisser (1986)).

Water included in crystalline structures in the form of crystal water will not change significantly the mechanical properties of the crystals. Water stored in the amorphous matrix has a plasticizing effect on the amorphous structure. The viscosity and elasticity of the material decrease with increasing water content. In parallel, the glass transition temperature decreases, due to the action of absorbed water as a plasticizer. This decrease in the glass transition temperature can be described using the Gordon and Taylor (1952) equation:

$$T_g = \frac{(1-w)T_{g,dry} + wkT_{g,w}}{(1-w) + wk} \tag{7.1}$$

$T_{g,dry}$ represents the glass transition temperature of the (dry) solid, $T_{g,w}$ the glass transition temperature of water, w the water content (wet-based) and k the so-called Gordon–Taylor constant.

In parallel with the decrease in glass transition temperature, a decrease in viscosity is also observed. This decrease in viscosity can be described by applying the superposition principle known from polymer physics. Following the time–temperature superposition principle, all relaxation mechanisms have the same temperature dependence (Williams *et al.*, 1955; Markovitz, 1975; Ferry, 1980). Thus,

viscoelastic data (like viscosity or modulus) obtained for one temperature and time or frequency can be extrapolated to a different temperature by multiplying the logarithmic time or frequency values with a temperature-dependent shift factor a_T. Williams *et al.* (1955) suggested Eq. 7.2 for estimating the viscosity shift factor:

$$a_T = \frac{\mu T_0 \varrho_0}{\mu_0 T \varrho} \tag{7.2}$$

The viscosity shift factor relates the viscosity μ of the solid material to the density ϱ and the temperature T. By applying the assumption that the product of absolute temperature and density is roughly constant, the Williams, Landel and Ferry (WLF) equation (Williams *et al.*, 1955) is obtained:

$$\log a_T = \log \frac{\mu}{\mu_0} = \frac{-C(T - T_g)}{B + (T - T_g)} \tag{7.3}$$

T_0 is a reference temperature, which is commonly chosen as the glass transition temperature of the solid, C and B are constants. Williams, Landel and Ferry found that the parameters $C = 17.4$ and $B = 51.6$ K were suitable for most polymers they investigated. Changes in viscosity due to an increase in temperature and/or moisture above T_g can be estimated using the WLF equation, if the glass transition temperature is known.

The mechanical properties (viscosity, elasticity) change drastically if the glass transition temperature is exceeded. In the amorphous glassy state substances react more elastically while exposed to any stress. Due to glass transition, the viscosity decreases from, for example, 10^{12} Pa s to $10^8 - 10^9$ Pa s (Sperling, 1986). Thus, amorphous solids become first rubbery and, finally, more plastically deformable (Roos and Karel, 1991; Slade and Levine, 1991).

Agglomeration during drying does not involve high compression forces. Particle collisions or application of moderate stress in a particle bulk are sufficient for a lasting deformation of the surface enabling adhesion of particles. Thus at least a part of the particle surface has to be well above the glass transition temperature in order to provide adhesion points on the particle surface.

7.3.1.2 **Van der Waals Forces**

Van der Waals forces are only relevant if the surface of the primary particles in contact with each other is significantly deformed and can be the forces responsible for initiating the contact prior to sintering. Van der Waals forces are based on temporary load shifts in neighboring surfaces. The van der Waals forces between particles can be estimated by calculating the electrostatic forces between two parallel circular plates with a diameter x according to Lifshitz (1956) or Hamaker (1937) using Eq. 7.4:

$$F_{vdW} = A\frac{x^2}{a^3} \quad \text{with} \quad A = \frac{h\varpi}{8\pi} = \frac{H}{6} \tag{7.4}$$

A is a constant valid for parallel circular contact areas and a is the distance between the contacting surfaces. A can be calculated using the Lifshitz-van der Waals constant $h\varpi$ ($= 10^{-20} - 10^{-18}$ J) or the Hamaker constant H ($= 10^{-19} - 10^{-18}$ J).

The van der Waals force between a sphere and a plate is significantly smaller than a typical capillary force. For spherical particles smaller than 5 μm, the van der Waals forces exceed gravity. For significant van der Waals forces particles have to be close (force proportional to a^{-3}) and the contact area has to be large enough (force proportional to x^2). Thus a deformation of drying particles is a prerequisite for generation of significant van der Waals forces.

Since the van der Waals forces depend strongly on the distance a between the particles and on the interparticle contact area, they can be increased by decreasing the former and/or increasing the latter (Eq. 7.4). This can be achieved by plastic or viscoelastic deformation of particle surfaces which depends on the mechanical material properties.

The adhesion force between two plastically deformed spheres can be calculated according to Rumpf *et al.* (1976):

$$F_{\mathrm{vdW}} \approx \frac{P_{\mathrm{vdW}}}{P_{\mathrm{pl}}} F_{\mathrm{t}} \quad \text{with} \quad P_{\mathrm{vdW}} = \frac{F_{\mathrm{vdW}}}{\pi x^2} = \frac{h\varpi}{8\pi^2 a^3}, \quad a \cong 0.4\,\mathrm{mm}, h \cdot \varpi \cong 5\,\mathrm{eV} \tag{7.5}$$

Here, F_{t} is the force with which the particles are pressed together and P_{pl} is the plastic yield pressure. The distance a is assumed to be approximately 0.4 nm when the particles are in contact (Rumpf *et al.*, 1976).

However, amorphous water-soluble materials, such as food materials, deform viscoelastically. The deformation and relaxation behavior of such materials can be described by means of various viscoelastic models. Depending on the nature of the stress/strain applied, either the storage and loss modulus or the elasticity and the viscosity are included as material parameters in these models. These rheological material parameters depend on the temperature and the water content as well as on the applied strain rate. The viscoelastic deformation enlarges the contact area and decreases the distance between the particles (see Fig. 7.3). If the stress decreases once again, the achieved deformation is partially reversed (structural relaxation).

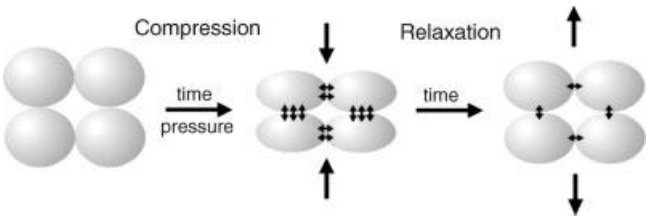

Fig. 7.3 Viscoelastic deformation and relaxation of food particles.

According to Rumpf *et al.* (1976) the contact area between two spherical particles which are viscoelastically deformed can be calculated using Eq. 7.6:

$$\left(\frac{x}{d}\right)^2 = \left(\frac{3}{32}\frac{F_t}{d^2}\right)^{2/3}\left(\frac{t}{\mu}+\frac{1}{E}\right)^{2/3} \tag{7.6}$$

F_t is the force with which the particles are pressed together, t the compression time, μ and E the viscosity and elasticity, respectively; x the diameter of the circular contact area and d the particle diameter. Combining Eq. 7.5 and 7.6 yields a relationship that enables calculation of the van der Waals forces between two viscoelastically deformed spheres:

$$F_{vdW} = \frac{h\varpi d^2}{8\pi a^3}\left(\frac{3}{32}\frac{F_t}{d^2}\right)^{2/3}\left(\frac{t}{\mu}+\frac{1}{E}\right)^{2/3} \tag{7.7}$$

As Eqs. 7.6 and 7.7 show, sufficient time and/or significant forces are necessary for agglomeration by plastic or viscoplastic deformation. During drying the forces are either a result of particle impact or of the weight of a particle bed. In many drying processes, such as spray drying or fluidized bed drying, the time that colliding particles are in contact with each other is relatively small. Thus the viscosity at the particle surface has to be low enough to allow yielding of the material in the short contact time. For instance, this is the case if amorphous material is not entirely dry. In spray drying or drying in fluidized beds, high temperatures and moisture contents may lead to low viscosities and thus agglomeration can occur even at short contact time.

Furthermore, agglomeration due to van der Waals forces will occur even if the viscosity of the material is in the medium range and the force applied is low, provided that the contact time between two neighboring particles is sufficient to develop significant adhesion forces. This is typically the case for drying on belts or shelves or during storage of particles with high residual moisture content.

The shorter the contact time and the higher the applied pressure, the more important is the viscoelastic deformation for developing adhesion forces between particles. After initial contact and adhesion a growing viscous bridge might be formed between the particles due to sintering. At long interparticle contact time and moderate pressure, sintering dominates the strength of the final agglomerate (Rumpf *et al.*, 1976). Sintering will be further discussed in Section 7.3.1.4.

7.3.1.3 Capillary Forces Due to Liquid Bridges Between Particles

Liquid bridges are the most important adhesion mechanism in spray or fluidized bed drying. In the case of spray granulation of food liquids, an aqueous concentrated solution is sprayed onto the fluidized particles and simultaneously dried. Droplets are deposited on the particle surface and can build liquid bridges between colliding particles, as will be discussed in more detail later. During spray drying one starts with droplets. Collisions of semidried droplets with dry particles lead to coating of particles. Once these coated particles collide with each other or with dry particles liquid bridges are established between the collision partners. The collision of semi-dried particles will also lead to the formation of agglomerates.

In the case of water-soluble crystalline substances with a low molecular weight the viscosity and stability of the liquid bridges will be low. Thus, the strength of the liquid bridge depends mainly on capillary forces. The capillary pressure P_c in a liquid bridge can be calculated using Eq. 7.8; γ is the surface tension, θ the wetting angle, s the radius of the meniscus of the liquid bridge and x the diameter of the cross-section area of the bridge:

$$P_c = \gamma \cos\theta \left(\frac{2}{x} - \frac{1}{s}\right) \tag{7.8}$$

The negative capillary pressure between the particles causes an adhesion force F_c between the particles. This adhesion force can be calculated according to Eq. 7.9 (Fisher, 1926; Willett *et al.*, 2007):

$$F_c = \frac{\pi d \gamma}{1 + \tan(\beta/2)} \quad \text{with} \quad F_{c,max} = \pi d \gamma \tag{7.9}$$

The parameter β represents the angle from the center of the particle to the segment wetted by the liquid bridge.

The capillary forces between two particles may also be calculated based on the energy of the system (Rabinovich *et al.*, 2005).

With time, the concentration of solids in a liquid bridge may increase because of drying (evaporation of water), migration of water into the particles (by capillarity or, in the case of amorphous solids, by diffusion) or dissolution of solids from the particles in the liquid of the bridge. Consequently, the stability of the bridge, initially dominated by capillary forces, is increasingly governed by viscous forces. Gradually, the relatively weak liquid bridge is transformed into a stable solid bridge. If the liquid bridge contains substances of lower molecular weight crystallization might occur. If the liquid contains a high amount of dissolved molecules with a medium or high molecular weight a viscoelastic amorphous bridge is obtained. The mechanical properties of such a bridge can be described through a complex shear or elongation modulus.

7.3.1.4 Viscous Forces in Sinter Bridges Between Amorphous Particles

Particles composed of amorphous substances might sinter together if their viscosity is low enough. Sintering is, therefore, for many undesired agglomeration processes occurring during drying, the main adhesion principle.

Amorphous substances have a liquid-like supramolecular structure. Like liquid droplets, two amorphous particles in contact with each other tend to adopt a spherical shape. Accordingly, molecules are transported to the contact point between the two particles. The capillary and vapor pressure gradients between the particle volumes and the contact point between the two particles are the driving force for these transport processes. Linked to these local differences in capillary and vapor pressure different molecular transport mechanisms are observed. The molecules can be transported via the surrounding gas phase (evaporation and sublimation), diffusion on the surface (surface diffusion/grain boundary diffusion) or diffusion

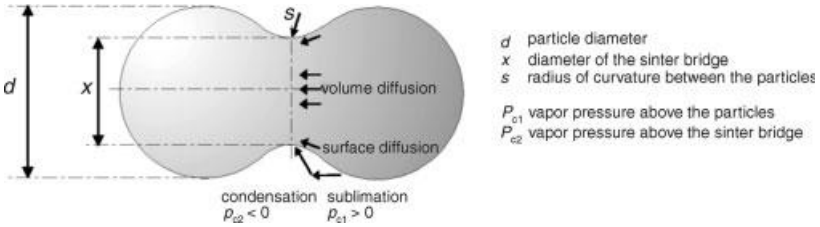

Fig. 7.4 Sintering mechanisms.

of the bulk amorphous material (volume diffusion/viscous flow) (Kuczynski, 1949; Schatt, 1992; Wagner, 1997). Substances having a medium or high vapor pressure can be transported via the gas phase surrounding the particles while substances with low vapor pressure (e.g., composed of larger molecules) exhibit volume diffusion.

Knowing the surface tension γ of the material, the primary particles of diameter d, the sinter bridge diameter x and the radius of meniscus curvature s, the capillary pressure gradient can be calculated through Eq. 7.10:

$$\Delta P_c = P_{cl} - P_{c2} = \frac{4\gamma}{d} - \gamma\left(\frac{2}{x} - \frac{1}{s}\right) \tag{7.10}$$

Here, P_{c1} represents the capillary pressure in the volume of the particles and P_{c2} is the capillary pressure in the sinter bridge.

Figure 7.4 illustrates the different sintering mechanisms. However, as mentioned earlier, volume diffusion remains for most amorphous substances (e.g., food substances) the most relevant sintering mechanism.

The kinetics of transport by volume diffusion depends on the diffusion coefficient, which is a function of viscosity. The viscosity of water-soluble amorphous substances, and thus also the diffusion coefficient in amorphous matrices, depends on the temperature as well as on the water content of the material. In Fig. 7.5 the surface of a

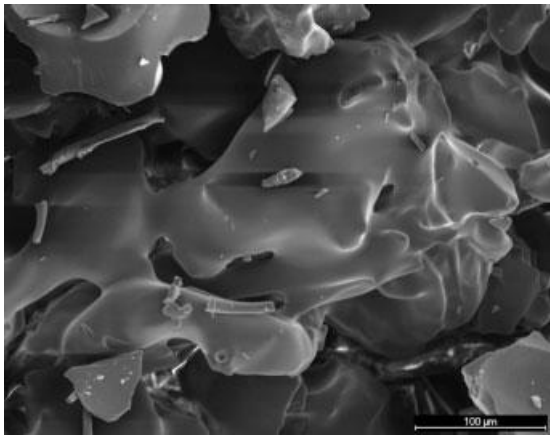

Fig. 7.5 Plasticized surface with sinter bridges of a maltodextrin (DE 17-20) agglomerate.

maltodextrin (DE 17–20) particle is shown. Areas which were humidified with water, and thus exhibit a significantly lower viscosity, are visible as smooth surfaces. While these areas are still wet they act as potential adhesion points during agglomeration.

Sintering of organic particles by viscous flow can be modeled using the equations of Frenkel (1945) (see Eq. 7.11) or Rumpf *et al.* (1976) (see Eq. 7.12):

$$\left(\frac{x}{d}\right)^2 = \frac{1}{6}\frac{\gamma}{d}\frac{t}{\mu} \tag{7.11}$$

$$\left(\frac{x}{d}\right)^2 = \left(\frac{4}{5}\frac{\gamma}{d} + \frac{2F_t}{5\pi d^2}\right)\frac{t}{\mu} \tag{7.12}$$

Rumpf *et al.* (1976), who assumed a punctual contact between the particles, neglected changes in particle geometry during the process, and applied the Navier–Stokes equations for viscous flow. In the two equations d is the particle diameter, x the diameter of the sinter bridge, t the contact time, γ the surface tension, μ the viscosity of the organic substance, and F_t represents the force with which the particles are pressed together.

Due to the assumption of non-deformed particles/unchanged geometry these equations are valid only for the initial period of the sinter process. For non-spherical particles the diameter d has to be estimated based on the curvature radius at the contact point between the particles. A prerequisite for the sinter process is molecular contact between the particles. Such contact can be established through particle collisions or by the pressure caused by the weight of particles in a bed. However, the impact of the force F_t on sinter kinetics can often be neglected. While variations in surface tension are commonly small, the viscosity often varies by orders of magnitude during drying due to large changes in temperature and moisture content. According to Palzer (2009) the growth of the sinter bridge during the time t_{max} can be calculated through Eq. 7.13.

$$\left(\frac{x}{d}\right)^2 = \int_{t=0}^{t_{max}} \left(\frac{4}{5}\frac{\gamma}{d} + \frac{2F_t}{5\pi d^2}\right)\frac{1}{\mu} 10^{\frac{-C\cdot(T-Tg(t))}{B+(T-Tg(t))}} dt \tag{7.13}$$

Figure 7.6 shows the calculated and measured bridge diameters for sintering of two dextrose sirup particles stored at 30 °C and 70% RH. Despite various simplifications, Eq. 7.13 allows a satisfactory estimation of the sinter kinetics. The accuracy might be further improved by taking into account in the solution of the Navier–Stokes equations viscosity gradients that arise from moisture gradients in the agglomerating particles, and a more precise estimation of viscosity which is the main influencing variable.

As one can see in Eq. 7.13, sintering kinetics depends on the difference between the process temperature T and the glass transition temperature T_g. Approaching the glass transition temperature sintering is drastically accelerated.

The importance of glass transition for, for example, food or pharmaceutical products has been highlighted in several previous chapters of this volume. It arises

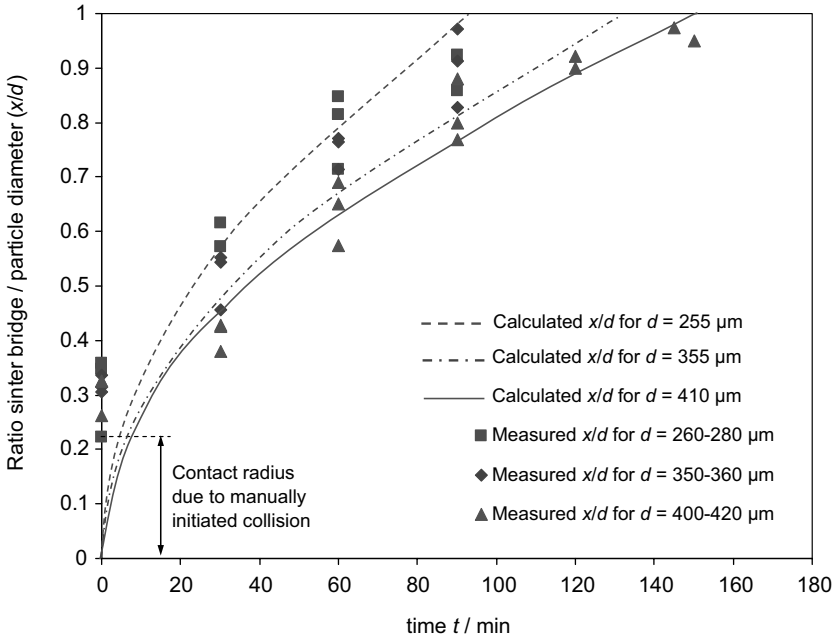

Fig. 7.6 Comparison between calculated and measured sinter bridge/particle diameter ratio for pairs of spray dried dextrose sirup particles (DE 21) stored at 30 °C and 75% RH ($T_g = -4$ °C; $\gamma = 70\,m\text{N m}^{-1}$, $\mu = 106$ Pa s).

from a shift in the mechanical properties of amorphous solids from a rigid glass-like texture to first rubbery and later viscoplastic textures. This shift in texture, which is a result of a dramatic increase in molecular mobility, enables deformation of particle surfaces and facilitates viscous flow of the material during sintering.

Palzer (2009) investigated the influence of moisture and temperature on fluidized bed agglomeration of dextrose sirup (DE 21). The glass transition temperature needs to be exceeded locally during granulation, fluidized bed agglomeration or spray drying in order to create sticky surfaces and to promote agglomeration. Impact of particles on surfaces where the glass transition temperature is exceeded leads to a deformation which increases the van der Waals forces. Following diffusion and capillary condensation a thin material bridge between the particles will be established. Successive rapid sintering will further strengthen the generated interparticle bridge.

However, if the glass transition temperature in the bed is exceeded macroscopically by 25–30 K (humidification with moist air), a collapse of the entire bed caused by the formation of large clumps is observed (Palzer, 2009). At this temperature, the viscosity of the dextrose sirup is in the range 10^7 to 10^8 Pa s which is in good agreement with the results published by Wallack and King (1988), Downtown *et al.* (1982) and Aguilera *et al.* (1993). This reveals one of the main difficulties in controlling the agglomeration of amorphous water-soluble food powders in a

fluidized bed or during any drying process. The moisture distribution must not be too homogeneous, as this will cause the whole to collapse once the sticky point of the particle bulk is exceeded. On the other hand, wet zones inside the bed, as often occur in the vicinity of the spray nozzle, will also produce agglomerates with a wide particle size distribution and undesired oversized particle structures. To avoid temperature/moisture combinations leading to a collapse of the bed or an increasing number of oversize particles during fluid bed granulation and drying, the aqueous binder has to be added with a low spray rate onto the fluidized particles, allowing the current of air to convey the evaporated moisture out of the fluid bed. Alternatively, the total added binder quantity can be reduced. In both cases the relative humidity of the air inside the fluid bed decreases and, hence, the glass transition temperature T_g and the viscosity of the particle surface increase. For spray drying such non-homogeneity of moisture can be achieved by adding back dry particles to the semi-dried droplets.

7.3.1.5 Mechanical Strength of Agglomerates

The strength of agglomerates generated by the different adhesion processes discussed in the previous sections depends on the strength of the respective adhesion forces acting between primary particles. It can be measured by different methods (see Section 6.3.6 in Volume 2 of this series). According to Rumpf (1970), the tensile strength of agglomerates composed of spheres with diameter d can be estimated through

$$\sigma_t = \frac{1-\varepsilon}{\pi d^2} KF, \quad K \approx \frac{\pi}{\varepsilon} \tag{7.14}$$

Here, F is the adhesion force between two spheres, ε the agglomerate porosity, and K the coordination number of the primary particles building the agglomerate. For spherical primary particles K is approximately equal to π/ε.

On this basis, the tensile strength of agglomerates which are stabilized by viscoelastically enhanced van der Waals forces can be estimated according to

$$\sigma_t = \frac{(1-\varepsilon)h\varpi}{8\varepsilon a^3}\left(\frac{3}{32}\frac{F_t}{d^2}\right)^{2/3}\left(\frac{t}{\mu(T,w,\dot{\gamma})} + \frac{1}{E(T,w,\dot{\gamma})}\right)^{2/3} \tag{7.15}$$

The viscosity and the elasticity both depend on the shear or strain rate γ, the temperature T and the plasticizer content w of the amorphous substance.

The tensile strength of agglomerates stabilized by low-viscosity liquid bridges can be estimated according to Rumpf (1958) using Eq. 7.16:

$$\sigma_t = SC\frac{1-\varepsilon}{\varepsilon}\frac{2\gamma}{d}\cos\theta \tag{7.16}$$

Here S is the saturation of the porous agglomerate with liquid (ratio of liquid volume versus total void volume within the agglomerate), C a constant parameter ($C = 6$ for monosized spheres), γ the surface tension of the liquid, and θ the liquid–solid contact angle (cf. Schubert (1975, 1979)).

Liquid bridges containing dissolved solids might dry out and thus the tensile strength of the agglomerates further increase. The tensile strength of such dry agglomerates can be calculated according to Rumpf (1958) by applying Eq. 7.17:

$$\sigma_t = \frac{V_{diss}}{V_{agg}}(1-\varepsilon)\sigma_s \tag{7.17}$$

V_{diss} is the volume of solid dissolved within the entire agglomerate, V_{agg} the volume of the entire agglomerate, and σ_s the tensile strength of the solid substance building the bridge after drying.

Combining Eqs. 7.13 and 7.14 the tensile strength of sintered agglomerates can be estimated according to Eq. 7.18:

$$\sigma_t = \frac{(1-\varepsilon)\pi}{\varepsilon}\sigma_s(T, w, \dot{\gamma}) \int_{t=0}^{t_{max}} \left(\frac{4}{5}\frac{\gamma}{d} + \frac{2F_t}{5\pi d^2}\right)\frac{1}{\mu}10^{\frac{-C(T-T_g(t))}{B+(T-T_g(t))}} \tag{7.18}$$

However, in practice it remains difficult to predict the tensile strength of sintered agglomerates because the primary particles are normally non-spherical and exhibit various geometries. Furthermore, the tensile strength of the viscoelastic bridges also depends on deformation speed, which makes it difficult to define and determine a stability parameter.

Apart from experimental results (Schubert, 1975), numerical simulations by Yang *et al.* (2008) that use the discrete element method (DEM) are also in good agreement with the model of Rumpf (Eq. 7.14). Note that, according to Eq. 7.14 the coordination number of primary particles decreases with increasing porosity (Smith *et al.*, 1929; Bika *et al.*, 2005), so that the strength of the agglomerates also decreases. A decrease in elasticity modulus and Poisson ratio with increasing porosity has been observed for both porous materials (ceramics, glass, polymers, cement clinkers) and composites (Boccaccini, 1994; Avar *et al.*, 2003).

An alternative to Eq. 7.14 has been proposed by Kendall *et al.* (1987) who considered a balance between the strain energy of compressed elastic primary particles of spherical shape with the potential energy of the applied load and the interface energy, assumed an empirical correlation for the coordination number, and introduced the parameter a as the maximal size of defects limiting the strength of agglomerates to obtain

$$\sigma_t = 3.7(1-\varepsilon)^4 \frac{F_t}{d\sqrt{d\,a}} \tag{7.19}$$

Bika *et al.* (2005) have extended the models of Rumpf and Kendall to agglomerates with solid bridge bonds between primary particles. The solid bridge bonds are formed by evaporation of a liquid bridge and precipitation of dissolved solids. It is assumed that the liquid bridge conserves its shape as it shrinks and solidifies.

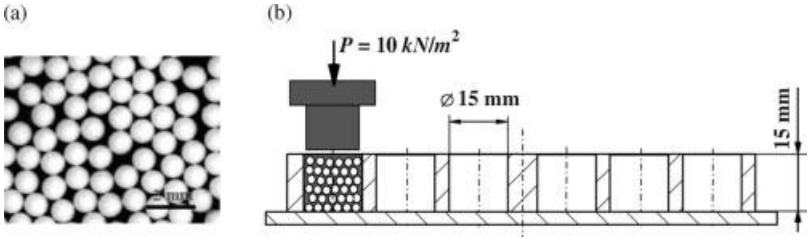

Fig. 7.7 (a) γ-Al_2O_3 primary particles used to produce the agglomerates, (b) scheme of agglomerate preparation.

The tensile strength of the agglomerate can be obtained from the strength of the solid bridge neck $\sigma_{br,s}$ by the relationship:

$$\sigma_t = \pi b^2 \frac{1-\varepsilon}{\varepsilon} \left[\frac{8 x_b V_{br}}{\varrho_p d^3} \right]^{2c} \sigma_{br,s} \tag{7.20}$$

where x_b is the mass fraction of solids in the liquid bridge, that is, the binder content, and V_{br} is the liquid bridge volume. The quantities ϱ_p and d are the primary particle density and diameter; b and c are numerical coefficients.

A simpler equation for agglomerate strength, namely

$$\sigma_t = \sigma_s (1-\varepsilon)(x_b - x_{b,min}) \tag{7.21}$$

was proposed by Tomas (1983). Equation 7.21 is similar to Eq. 7.17. It describes the strength of the agglomerate as a linear function of porosity and binder strength σ_s. A minimal mass fraction of binder $x_{b,min}$ in the solution is considered to be necessary in order to stick together the primary particles with solid bridge bonds after drying.

This model showed good agreement with experiments performed with dry cylindrical agglomerates (Antonyuk and Tomas, 2008; Antonyuk *et al.*, 2011). The agglomerates were prepared from spherical γ-Al_2O_3 particles ($d_{50} = 1.0$ mm) with a water solution of hydroxypropyl methylcellulose (HPMC) by compaction in a cylindrical die (Fig. 7.7) and drying for 1 h at 80 °C. The binding agent was heated to 40 °C and added to the primary particles in a mixer. For all agglomerates produced, the mass ratio of the solid particles to the water solution of the binder was maintained at a constant value of 1.42. However, solutions with different HPMC concentrations (6, 10, 13 and 16 wt%) were used in order to investigate the influence of binder ratio on the mechanical properties of the agglomerates. After compaction and drying the mass fraction of HPMC in the agglomerates, that is, the binder content x_b, was 4.0, 6.5, 8.3 and 10.1 wt%, respectively. Compaction was done in the direction of the principal axis. In order to vary the agglomerate height, different cylindrical dies with heights of 8, 12 and 15 mm and constant inner diameter of 15 mm were made.

Compression tests were performed on single primary particles and agglomerates by using the Granule Strength Measuring Device (Etewe GmbH, Germany) at a constant stressing velocity of 0.04 mm s^{-1}. Fifty agglomerates of each binder content

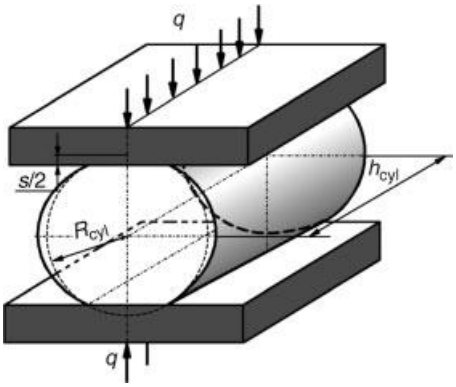

Fig. 7.8 Scheme of compression tests with diametral loading condition.

and size were tested in order to increase the statistical significance of the measurement. The compression test was carried out laterally to the principal axis of the cylinder (Fig. 7.8).

The typical force–displacement curve of a primary spherical particle (γ-Al_2O_3) in Fig. 7.9a shows clearly both elastic and plastic displacement ranges. The elastic displacement of the spherical particle up to the yield point F was described using the Hertz contact theory of spheres (Hertz, 1882; Antonyuk *et al.*, 2011) according to

$$F_{N,el} = \frac{1}{6} E^* \sqrt{d \cdot s^3} \tag{7.22}$$

The effective modulus of elasticity E^* in Eq. 7.22 refers to both the particle (without index) and the punch (index w for wall), and is given by:

$$E* = 2\left(\frac{1-\upsilon^2}{E} + \frac{1-\upsilon_w^2}{E_w}\right)^{-1} \tag{7.23}$$

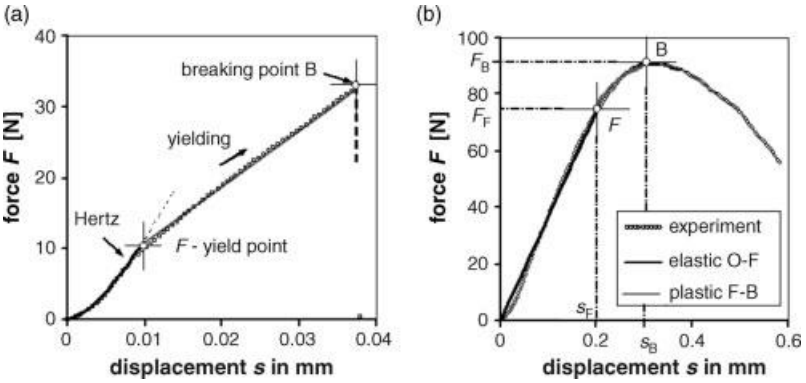

Fig. 7.9 Typical force–displacement curves during compression of (a) spherical primary particles (γ-Al_2O_3, $d = 1.03$ mm) and (b) cylindrical agglomerates ($d_{cyl} = 15$ mm, $h_{cyl} = 15$ mm) prepared from these γ-Al_2O_3 particles and 4% of HPMC binder.

where υ and υ_w are the Poisson ratios of the particle and the punch (see also Chapter 6 in Volume 2 of this series). The effective contact stiffness of elastic deformation depends on the deformation and particle diameter as:

$$k_{el}^{*} = \frac{1}{4} E^{*} \sqrt{ds} \tag{7.24}$$

With known properties of the punch, the modulus of elasticity and the elastic contact stiffness of the primary particles were determined to be the values given in Tab. 7.3.

Figure 7.9b shows the typical force–displacement curve of a cylindrical γ-Al_2O_3 agglomerate. At the beginning of loading the contacts are elastically deformed. The elastic force–displacement line up to the yield point F can be described using an elastic contact model (Antonyuk and Tomas, 2008):

$$F_{el} = 0.39 \frac{E_{cyl} h_{cyl}}{1 - \upsilon_{cyl}^{2}} s \tag{7.25}$$

where E_{cyl} is the modulus of elasticity of the cylindrical agglomerate, h_{cyl} the height of the cylinder, υ_{cyl} the Poisson ratio, and s the displacement during the deformation.

The modulus of elasticity of the agglomerates is much lower than that of the primary particles (Tab. 7.3). However, the elastic stiffness of agglomerates and primary particles is of the same order of magnitude.

The force–displacement curve changes beyond the yield point from elastic to ideally plastic behavior. The displacement s_F and the force F_F obtained at the yield point of force–displacement curves and the yield pressure P_F were used as model parameters to approximate the plastic force (Antonyuk and Tomas, 2008):

$$F_{pl} = F_F + 2 P_F h_{cyl} \sqrt{R_{cyl}(s - s_F)} \tag{7.26}$$

where R_{cyl} is the radius of the cylinder.

Compared to the rapid force drop during the breakage of a primary particle (point B, Fig. 7.9a), the force decrease after the primary breakage of agglomerates (Fig. 7.9b) occurs not so clearly because of deformation and secondary breakage of the fragments which were constrained between the two plates.

Figure 7.10a shows the influence of binder mass traction x_b in the agglomerate on its compression strength σ and elastic stiffness $k_{cyl,el}$. The increase in binder content increases the strength of agglomerates. Point A indicates the minimum binder content which is necessary to stick together the primary particles by solid bridge bonds (here, $x_{b,min} = 1.9$ wt%). Agglomerate strength was described as a linear function of this minimum necessary binder content and binder strength σ_b using Eq. 7.21. With increasing binder content the elastic stiffness also increases. Equivalent to Eq. 7.21, a linear relationship between the stiffness and the binder content can be used, $k_{cyl,el} = k_{br,s}(1 - \varepsilon)(x_b - x_{b,min})$, where $k_{br,s}$ is the stiffness of the solid bridge bond.

The fracture plane of the examined agglomerates coincides with the plane of loading, as indicated in Fig. 7.11. Due to maximum tensile stresses, the cracks

Tab. 7.3 Mechanical properties of cylindrical agglomerates ($d_{cyl} = 15$ mm, $h_{cyl} = 15$ mm, binder content $x_b = 4$ wt%) and their primary particles (γ-Al_2O_3, $d = 1.03 \pm 0.06$ mm).

Material	yield point		modulus of elasticity E (kN mm^{-2})	elastic stiffness k_{el} ($F = F_F$) (kN mm^{-1})	plastic stiffness k_{pl} ($s = 0.98 s_B$)(N mm^{-1})	breakage point	
	F_F (N)	s_F (µm)				F_B (N)	s_B (mm)
Primary particles	10.5	9.4	25 ± 0.7	2.6 ± 0.21	885 ± 31	32.5	0.033
Agglomerate	75.5	200	0.08 ± 0.02	1.1 ± 0.27	144.4 ± 25	93	0.33

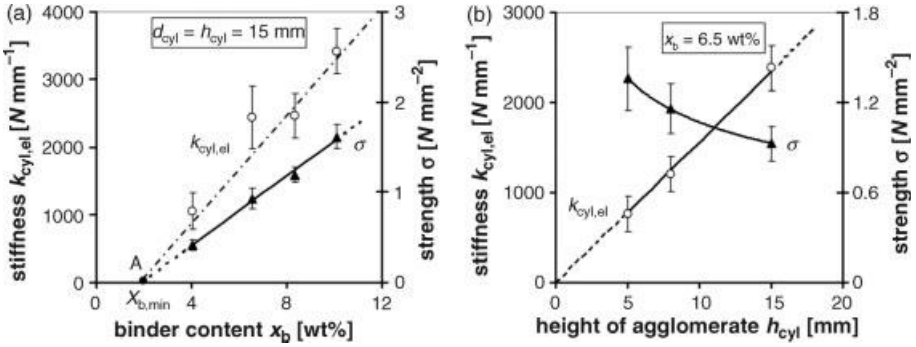

Fig. 7.10 Effects of (a) binder content x_b and (b) height h_{cyl} of cylindrical γ-Al_2O_3 agglomerates on their elastic stiffness $k_{cyl,el}$ and strength σ during compression.

propagate in the loading direction and separate the agglomerate into two approximately equal fragments. On the micro level, interparticle breakage occurs, that is, only the solid bridge bonds break but not primary particles because of their higher strength in comparison with the binder.

The breakage probability at different binder contents is plotted in Fig. 7.12 versus the mass related breakage energy. As expected, the curve shifts to the right with increasing mass concentration of binder in the agglomerate. Compared to the agglomerates, the breakage energy of the primary particles is much larger ($W_{m,10} - W_{m,90} = 730$–$1230\,J\,kg^{-1}$).

Agglomerates formed with the help of highly viscous liquids and agglomerates with high saturation levels show a dependence of the tensile strength on capillary pressure (Schubert, 1975). Porosity and pore size distribution have a large effect on the breakage behavior – similar to the effect of the size distribution of defects on the breakage of crystalline materials. The pores in agglomerates can be seen as crack release zones with high stress concentration.

As a consequence of wetting, chemical reactions can occur within agglomerates, whereby the original mechanical properties can be changed. To avoid such changes, many experiments were carried out with model binder solutions and primary

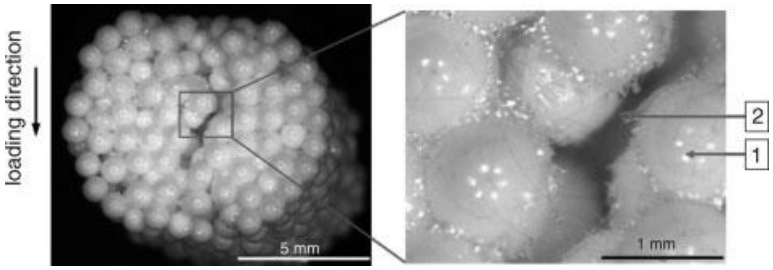

Fig. 7.11 Photos of the cylindrical agglomerate after breakage during compression and of the corresponding crack zone; 1: unbroken primary particles, 2: broken solid bridge bonds.

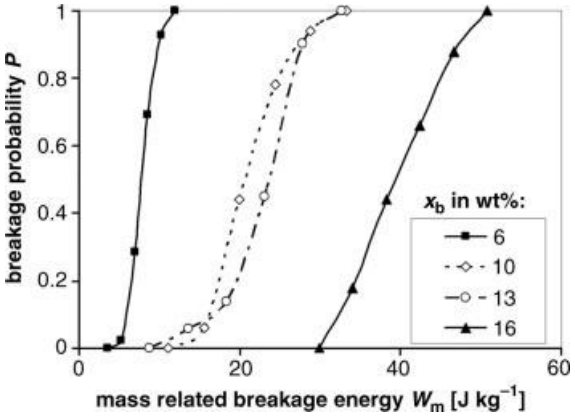

Fig. 7.12 Breakage probability P of γ-Al_2O_3 agglomerates ($d_{cyl} = 15$ mm, $h_{cyl} = 15$ mm, with different binder content x_b) versus mass related breakage energy W_m during compression.

particles, for example, glass beads (Pierrat and Caram, 1997; Iveson and Page, 2001). Briscoe *et al.* (1998), Pepin *et al.* (2001) and Samimi *et al.* (2003) performed compression tests on spherical agglomerates and determined the force–displacement curves. An overview of previous work on the strength of wet agglomerates was given by Simon *et al.* (2001).

Compared to crystalline solids, agglomerates are particle compounds that tend to plastic force–displacement behavior. Depending on the formulation process, internal adhesion is influenced by the superposition of van der Waals interactions between fine primary particles, capillary or solid bridges, high-viscosity binder, organic macromolecules, sintering or interlocking of particles. The mechanical breakage of agglomerates is, therefore, rather determined by these micro-binding mechanisms than correlated with the stress state – as even the earliest systematic investigations of the strength of agglomerates show (Rumpf, 1958; Schubert, 1975; Kendall *et al.*, 1987).

7.3.2
Breakage of Agglomerates and of Granulated Products

After having addressed the breakage of cylindrical agglomerates consisting of large primary particles, the breakage of spherical agglomerates made of much smaller primary particles will be treated in the present section to show that typical patterns of elastic–brittle or elastic–plastic breakage behavior can occur. Additionally, plastic breakage and the breakage behavior of layered granules will be discussed. The contents of the present section may be compared with results from the literature gained with structured materials such as concrete (Tomas *et al.*, 1999; Khanal *et al.*, 2008) or fertilizer granules (Salman *et al.*, 2003). Breakage depends on the loading energy, the material, particle shape and particle roughness. Material behavior, whether elastic or plastic, depends on the stressing intensity and agglomerate size. Fracture can hardly be understood without consideration of particle microstructure.

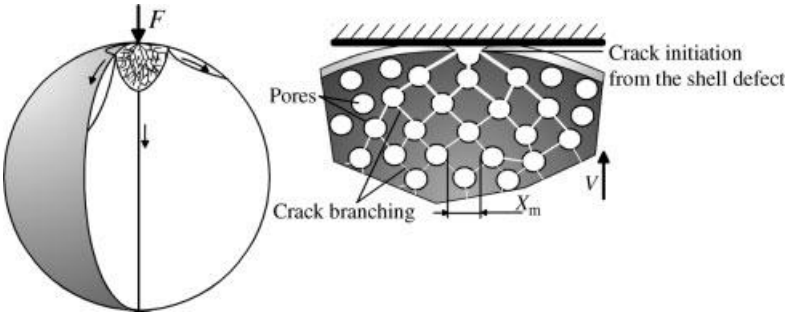

Fig. 7.13 Crack propagation during impact of an elastic γ-Al_2O_3-granule.

7.3.2.1 **Elastic–Brittle Breakage Behavior**

Elastic–brittle breakage behavior is characterized by a failure which begins during elastic deformation and is attended by non-stationary cracks, where no external energy input is needed to grow the cracks with a rapid propagation velocity.

Such behavior was observed by Antonyuk *et al.* (2006) on commercially produced, spherical γ-Al_2O_3 particles. These particles had a thin shell around a porous core. The average distance between two pores was about 0.5 μm, corresponding roughly to the respective primary particle size. The granules were tested by impact with a target (steel wall) using an "air gun" (cf. Chapter 6 in Volume 2 of this series). Breakage during impact was captured with a high-speed camera.

The breakage mechanism is represented schematically in Fig. 7.13. The meridian cracks occur after the contact with the target wall. The cracks initiate from the perimeter of a circular contact area, where a maximum tension stress appears. Small shell defects that arise during production and transportation are the starting point. With a rapid propagation of cracks (divergent to the impact axis), the grains are separated into several meridian fragments (Fig. 7.14). The smooth area of the meridian cracks through the porous γ-Al_2O_3-granules ("1" in Fig. 7.14) clearly refers to brittle fracture, without plastic deformation. In addition, many small cracks occur within the conical contact area ("2" in Fig. 7.14), where the energy density is very high at the moment of impact. The crack propagates from one pore to another, as shown schematically in Fig. 7.13. As a result, many fine particles are formed within the range 0.5 μm (the already mentioned average distance between

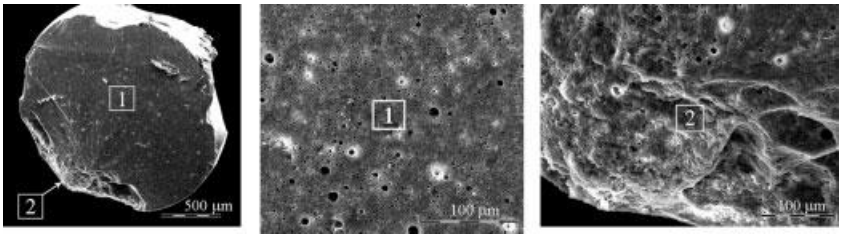

Fig. 7.14 SEM of the fracture surface of a γ-Al_2O_3-granule after impact at 31 m s^{-1} (1: meridian fracture surface, 2: fracture surface in contact area).

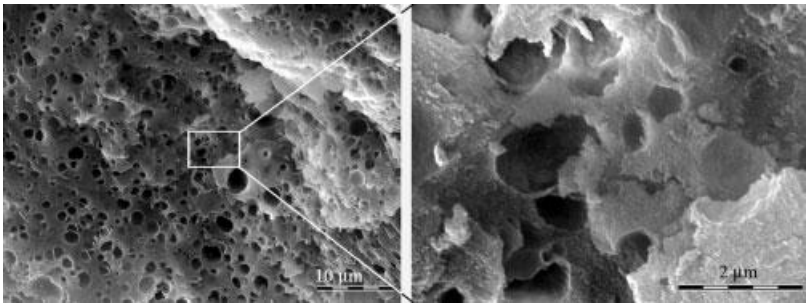

Fig. 7.15 SEM of the fracture surface of a γ-Al_2O_3-granule in the contact area ("2" in Fig. 7.14), resulting from crack branching.

pores, Fig. 7.15) to 100 µm. At high impact velocity, secondary cracks are formed and they are perpendicular to the direction of impact.

7.3.2.2 **Elastic–Plastic Breakage Behavior**

Elastic–plastic breakage is characterized by an amount of plastic deformation before the failure. The plastic deformation usually occurs at the contact point, where the energy concentration and stress are much higher than in the whole particle volume. A typical breakage pattern of elastic–plastic spherical particles is shown in Fig. 7.16 for zeolite agglomerates undergoing impact loading. The flattened surface develops under compressive stress around the contact point and deforms plastically. Then, a sharp, non-fragmented cone penetrates into the agglomerate. The resulting tension leads to the meridian cracks, which separate fragments from the remaining core.

The core (or nucleus) depicted in Fig. 7.16 has to do with the formulation process of the13X synthetic zeolite, which was an aggregate of fine crystals in the size range 1–8 µm. The crystals were agglomerated with clay as the binder and water as the solvent, which form solid bridges between the primary particles after drying. Zeolite primary particles bonded by the binder can be seen on the SEM of the agglomerate surface in Fig. 7.17. Primary particles do not contact each other directly; they are connected by three to six solid bridge bonds for each primary particle, due to inhomogeneous distribution of the binder. Rolling agglomeration in a drum was the

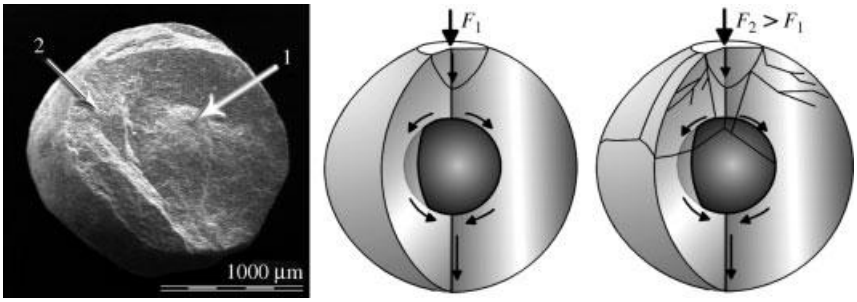

Fig. 7.16 SEM of the fragment of a zeolite agglomerate after impact at 18 m s^{-1} (1: nucleus, 2: shell) and schematic representation of crack propagation at different impact forces.

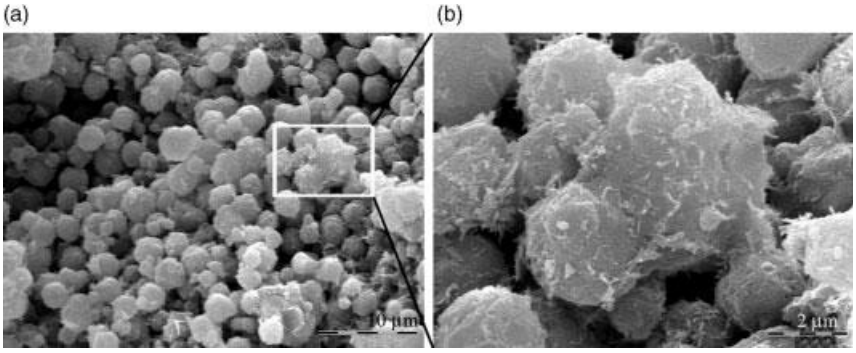

Fig. 7.17 SEM of the zeolite agglomerate before impact: (a) agglomerate surface, (b) solid bridge bonds between primary particles.

formulation process. In this process, nuclei are mixed in a drum with much finer zeolite particles, grow in size by accumulating primary particles and form spherical agglomerates. The layers developing first on the nucleus surface have many defects in solid bridges and large porosity, and hence they are weak. Compared to these layers the nucleus of the agglomerate is closely packed, has a better distribution of binder, and a firmer structure. During the impact, the cracks formed at the plastically deformed contact area propagate through the weakest agglomerate layers towards the nucleus, as shown in Fig. 7.16. The nucleus remains unbroken. The nucleus can be fractured at impact velocities larger than 30–35 m s^{-1} owing to the high inertial forces (right-hand side of Fig. 7.16).

At the micro-level one can distinguish between trans-particle and interparticle breakage (similar to trans- and intercrystalline breakage in the damage mechanics of materials). In the case of trans-particle breakage, primary particles and binder are destroyed. On the other hand, in interparticle breakage the failure appears at the contacts of primary particles. This means that only the solid bridge bonds break. Interparticle breakage was observed in the zeolite agglomerate. The unbroken primary particles with broken solid bridges can be seen in the SEM of the fractured surface in Fig. 7.17 and compared with the structure before the impact in Fig. 7.18.

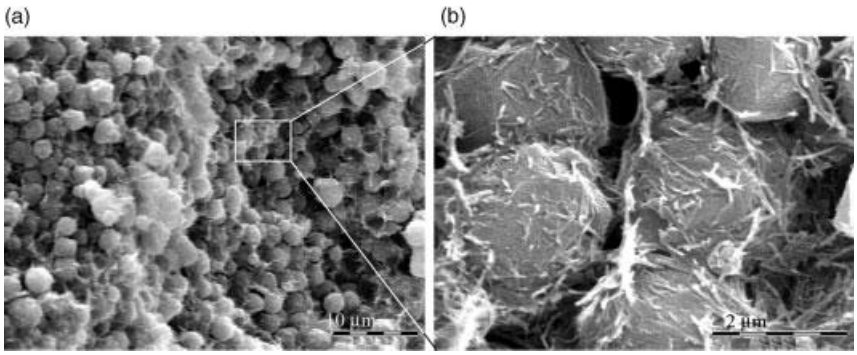

Fig. 7.18 SEM of fractured surface of elastic–plastic zeolite agglomerate after impact at 18 m s^{-1}: (a) fractured surface, (b) broken solid bridge bonds between primary particles.

7.3.2.3 Plastic Breakage Behavior

Plastic breakage is characterized by a large amount of plastic deformation before failure and by stationary crack growth, which means that external energy is permanently necessary for the cracks to propagate. Measurements of the yield point and the breakage strength of dominantly plastic agglomerates are difficult because of the small yield limit. After reaching this limit, irreversible deformation takes place. In many cases, during this deformation no instantaneous drop of the force, which would indicate the breakage point, can be obtained. Moreover, in the case of stationary crack growth the force does not significantly decrease, so that the breakage point can be detected only as a change of momentary stiffness (Fig. 7.19). Therefore, an acceptable limit of shape change, that is, quality loss, can more adequately characterize the breakage behavior than a value of breakage strength.

The force–displacement curve of spherical plastic granules is a straight line along the whole deformation region up to the breakage. Figure 7.20 shows the force–displacement curves of sodium benzoate granules obtained during the uniaxial compression test (Antonyuk *et al.*, 2010). In the case of bigger plastic granules, both the breakage force and the contact stiffness increase. Therefore, the material becomes stiffer with increasing granule diameter. This effect is also valid for elastic granules, see Eq. 7.24.

The increase in the breakage force does not influence the material strength of plastic granules. As an example, for different size fractions of sodium benzoate the average compressive strength is about 10.6 MPa. The yield pressure P_F in the contact is also independent of particle size (about 113 MPa). Assuming ideal plastic deformation with uniform pressure P_F in the contact area, the compressive strength of predominantly plastic granules can be described by the equation

$$\sigma_F = 0.1\, P_F \tag{7.27}$$

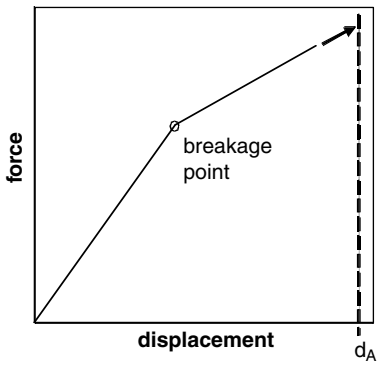

Fig. 7.19 Typical shape of the force–displacement curve for predominantly plastic behavior.

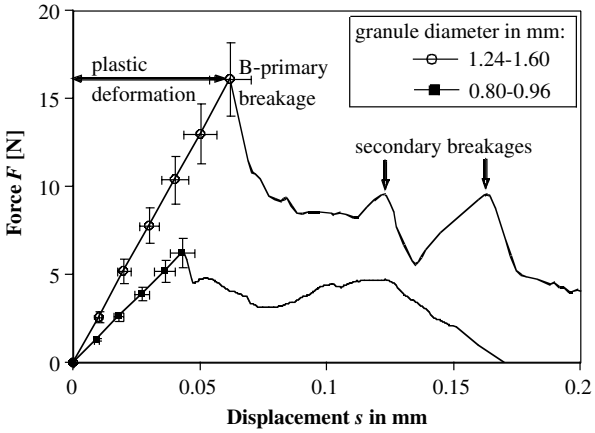

Fig. 7.20 Typical force–displacement curves of sodium benzoate granules during compression (stressing velocity: 0.02 mm s^{-1}).

(Antonyuk *et al.*, 2011). At the same deformation value, the formed contact area increases with increasing particle size.

7.3.2.4 **Breakage of Granules with Layered Structure**

As already discussed in Section 7.2, fluidized bed spray granulation leads to particles with a layered structure. By spraying on cores, particles with a firm nucleus and a soft onion-like shell can be formed. Such a particle made of sodium benzoate is depicted in Fig. 7.21.

During compression testing of the layered structure, the high tensile stress, which is perpendicular to the direction of loading, leads – as before – to the formation of meridian cracks. According to Fig. 7.22, the shell first deforms around the contact point. Then, a crack (1) is released and reaches the surface that separates the stiff nucleus (2) from the shell (3). The force–displacement curve of Fig. 7.23 shows that, after the formation of a meridian crack in the shell (Point B_1), deformation and then

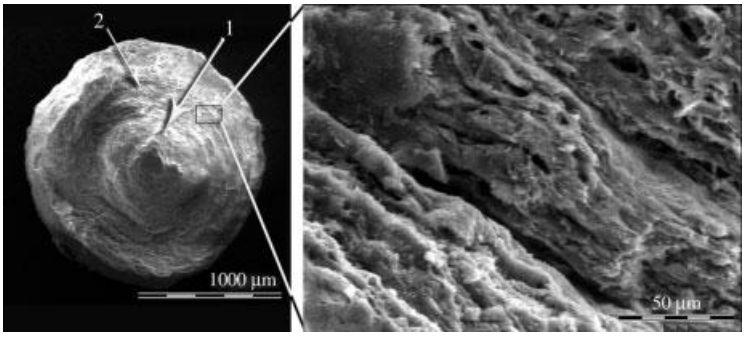

Fig. 7.21 SEM of the cross-section of a sodium benzoate particle produced by fluidized bed spray granulation (1: nucleus, 2: layered shell).

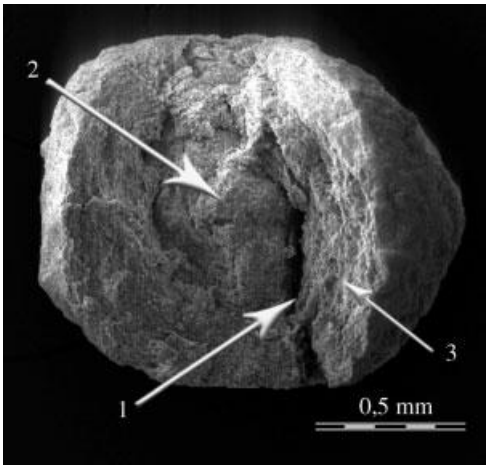

Fig. 7.22 SEM of the fracture surface of granulated sodium benzoate after compression test (1: crack, 2: nucleus, 3: shell).

full breakage of the nucleus take place. The latter leads to a secondary increase in the force (point B_2). In the depicted case the cohesive forces of the first shell layer with the nucleus are substantially weaker than the cohesive forces between adjoining layers in the shell.

7.3.3
Consideration of Primary Particle Properties in Agglomeration

The rate of agglomeration in spray fluidized beds is proportional to the frequency of collisions and the probability that colliding particles will stick together rather than

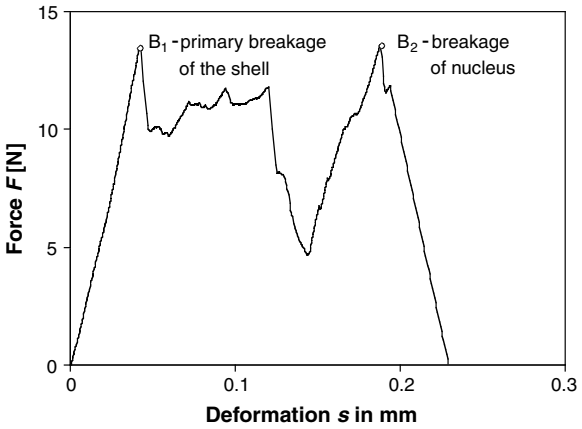

Fig. 7.23 Force–displacement curve of granulated sodium benzoate during compression (stressing velocity: 0.02 mm s^{-1}, $d = 0.87$ mm).

rebound (see Section 7.7). Particles stick together when colliding at wet positions, provided that the liquid film covering such positions can dissipate the energy of the collision impact (Stokes criterion).

It is, thus, evident, that the agglomeration rate depends on the fraction of outer particle surface covered with binder. This fraction does not immediately result from how much liquid is sprayed into the bed, because sprayed liquid may be located both on the surface or in the interior of porous agglomerates. Liquid on the surface can lead to further aggregation, whereas liquid trapped in agglomerate voids is not accessible and, therefore, inactive for agglomeration (steric hindrance). Fractional surface coverage and accessible binder fraction depend on the properties of primary particles, so that these properties are expected to also influence the kinetics of the agglomeration process.

An interesting analysis of the mentioned effects has been provided by Stepanek and coworkers (Stepanek and Rajniak, 2006; Stepanek *et al.*, 2009). The goal of these authors was to quantify the influence of the primary particle properties – especially of primary particle shape, surface morphology and roughness – of four typical powders used as excipients in the pharmaceutical industry on their agglomeration behavior. The four excipients were (Stepanek *et al.*, 2009) Avicel (which is rather smooth and round), lactose and mannitol (of intermediate roughness), and A-Tab (rough and rather irregular primary particles).

First, primary particles were created computationally in the form of so-called Gaussian blobs (Stepanek and Rajniak, 2006), as illustrated in Fig. 7.24. This method distorts more or less strongly the surface of a sphere towards different primary

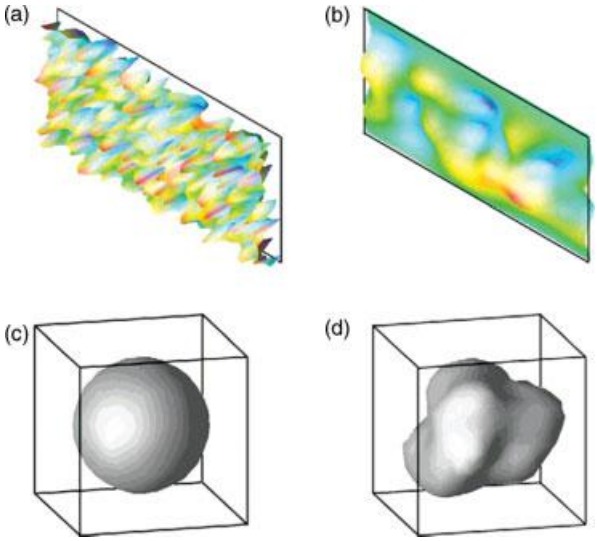

Fig. 7.24 Reconstruction of primary particles of different morphology as "Gaussian blobs" according to Stepanek and Rajniak (2006): (a) field of independent random variables, (b) Gaussian-correlated random field, (c) underlying spherical particle, (d) particle surface modulated by the correlated random field.

particles that can closely mimic the different surface morphologies of the four mentioned real powdery materials. Then, agglomerates, each containing 120 primary particles, were formed and loaded with different amounts of liquid by means of a ballistic deposition algorithm (Coelho *et al.*, 1997).

The results of the evaluation of the obtained wet agglomerates with respect to the fractional surface coverage and the spatial distribution of the binder are presented in Fig. 7.25. The fractional surface coverage is depicted in Fig. 7.25a. It is an increasing function of the volumetric binder/solid ratio in the granule. The curve shows two distinct regions. At lower ratios the fractional coverage is independent of the primary particle shape (wet granule in pendular state). By adding more liquid, a transition to the capillary state occurs, which is highly dependent on the primary particle morphology. The accessible binder fraction (Fig. 7.25b) follows a sigmoidal dependence on granule composition, which can

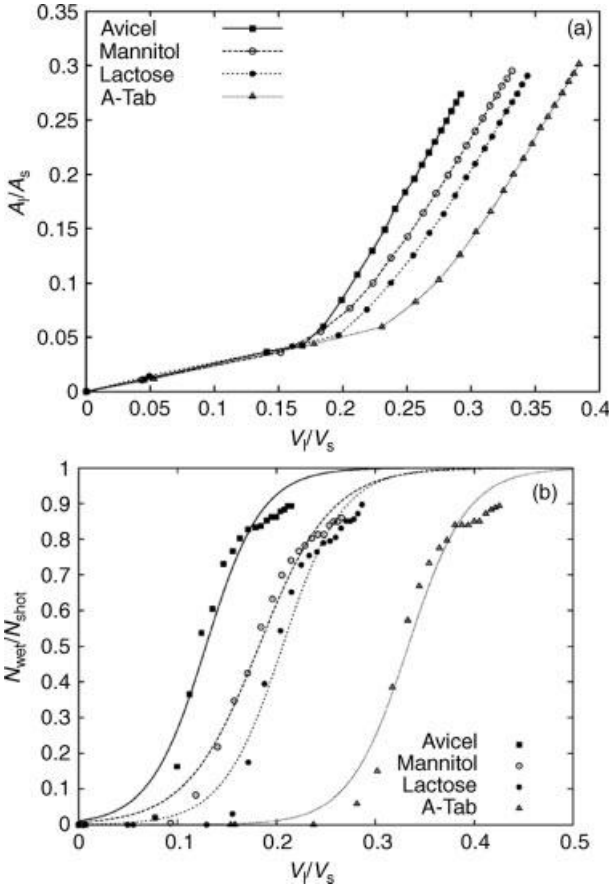

Fig. 7.25 Effect of primary particle shape on (a) the relative fractional coverage with binder and (b) the accessible binder fraction, as a function of granule composition.

be explained as follows: At relatively low binder fractions most of the binder is bound in capillary bridges between primary particles and thus sterically hindered, that is, shielded from other particles colliding with the considered agglomerate. Once a certain, shape-dependent critical value is exceeded, more and more liquid binder volume becomes exposed on the accessible outer surface of the agglomerate. The accessible binder fraction reaches 100% well before the fractional surface coverage.

One manner of using the presented results is to incorporate them in the traditional way of tackling fluid bed granulation theoretically, namely population balance modeling. This can be achieved by expanding the population balance to more internal coordinates than just particle size (see Volume 1 of this series, Chapter 6, Section 6.9.1). The additional property in the case of the present example would be wet agglomerate composition, defined either by the mass fraction of solids within one particle or the binder/solid ratio. The latter can be further split up to account for the spatial distribution – and, thus, accessibility – of the liquid binder and for the thickness of the binder layer on the outer surface of the agglomerate. Alternatively, discrete models of agglomeration (see Section 7.7) could be expanded to account for non-spherical primary particles.

7.4
Influence of Operating Conditions

The previous discussion pointed out that various material properties have a more or less strong influence on particle formulation in spray fluidized beds. Process conditions, such as the spraying rate, gas temperature, or the mass flow rate of the fluidization gas, can also very significantly affect the properties of the resulting particles. This aspect will be illustrated in the present section by means of selected examples.

7.4.1
Mechanical Strength of Granulated Particles

A major quality feature of particles is their mechanical strength. This parameter depends mainly on the material properties but also, as discussed in Section 7.3.2, on the microstructure of the particles. Microscopic changes in the structure, porosity or surface properties of the granules occur under the influence of different process parameters and can lead to major changes in properties on a macroscopic scale, for example breakage and attrition resistance.

To demonstrate the effect of different process parameters on the mechanical strength, granulation experiments were performed in a cylindrical fluidized bed unit with an inner diameter of 250 mm and a fluidization chamber height of about 500 mm. The pilot plant (Fig. 7.26) can be operated with superheated steam or air in batch or continuous mode. The experiments presented here were batch, with 5 kg of synthetic zeolite particles with a Sauter diameter of 2.18 mm as the starting material.

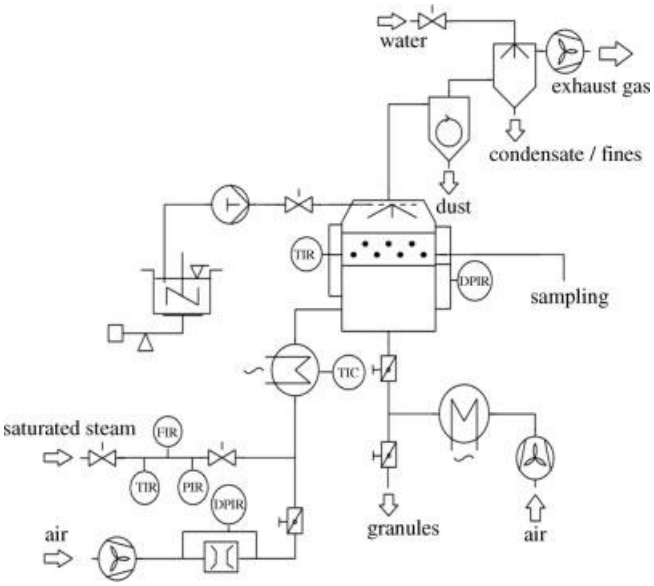

Fig. 7.26 Scheme of pilot plant.

An aqueous solution of sodium benzoate (30 wt%) was sprayed on these particles. The solution also contained different amounts of binder (HPMC, Pharmacoat 606 from ShinEtsu Co.).

During the granulation experiments samples were taken at constant time intervals. For each sample the particle size distribution was analyzed by means of a Camsizer (see Section 5.2.2 in Volume 2 of this series). Additionally, the mechanical strength was determined per uniaxial compression (see Chapter 6 in Volume 2 of this series). The results are visualized by plotting the breakage probability versus the breakage energy, similarly to the plot of Fig. 7.12 of Section 7.3.1.

7.4.1.1 **Influence of Binder Content in the Sprayed Solution**

Figure 7.27 shows the evolution of particle size distribution for a trial with 4 wt% of binder. The hold up material grows with time. Moreover, a fraction of very small particles appears after approximately 2.5 h. This peak is caused by breakage or attrition processes producing internal nuclei.

Figure 7.28 depicts the breakage probability of the granules after 3 h granulation time for different binder mass fractions. The remaining process parameters, such as mass flow rates and temperatures, were kept constant. The measurements show that higher mass fractions of binder lead to lower specific breakage energy. This result seems to correlate with the different shapes of the granules. It is known, that spherical objects have a high breakage resistance. As Fig. 7.29 shows, such particles are obtained for low binder concentrations or without binder. In contrast, high binder content results in a very irregular surface structure of particles which are less strong and easier to break.

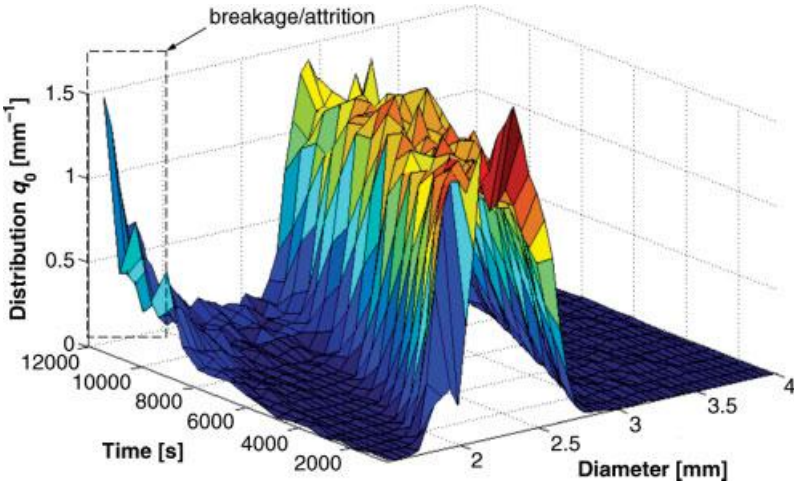

Fig. 7.27 Evolution of the number density distribution of bed material with 4 wt% of binder.

7.4.1.2 Influence of the Particle Retention Time

To analyze the influence of process time on particle strength, tests were performed under dry conditions without liquid injection. In Fig. 7.30 the breakage probability of different samples taken at 5, 10 and 15 min retention time is depicted.

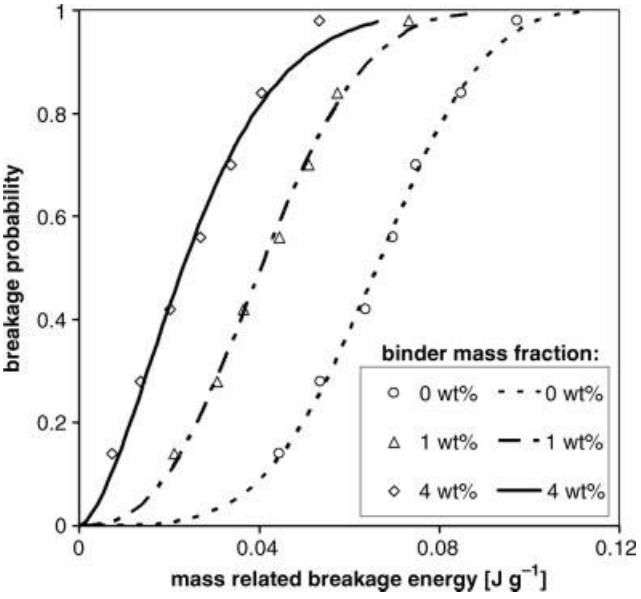

Fig. 7.28 Influence of binder content on the breakage probability after 3 h of granulation ($d_{32} = 2.9$ mm, $T_{bed} = 60\,^{\circ}C$; symbols: experiment, lines: model described in Chapter 6 of Volume 2 of this series).

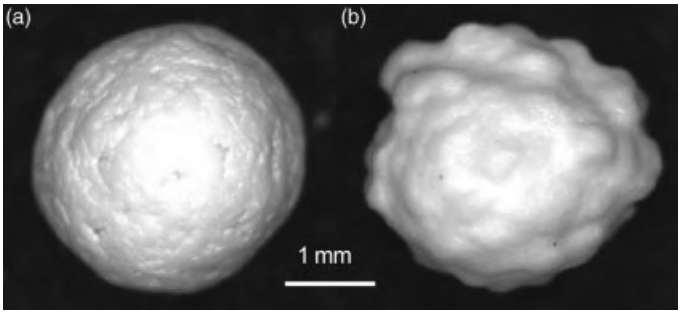

Fig. 7.29 Shape of granules after 3 h granulation: (a) no binder, (b) 4 wt% binder.

The measurements show that the mean specific breakage energy increases with increasing process time. Longer tests reveal that the increase in particle strength stops after about 15 min. These results can be explained by the selection of weak particles, which easily break, out of the particle population.

7.4.1.3 Influence of Process Temperature

Finally, the influence of bed temperature was analyzed by varying this process parameter from 60 to 120 °C at a constant granulation time of 60 min. Figure 7.31 shows that the highest values of granule strength and breakage energy were obtained

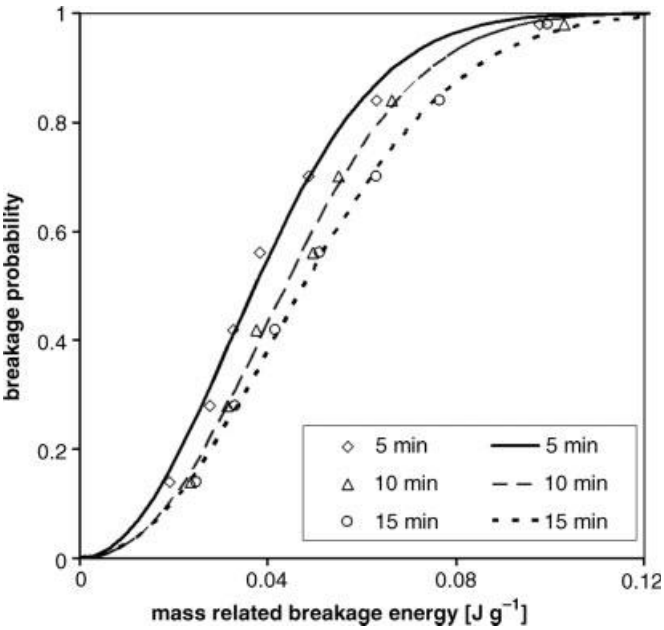

Fig. 7.30 Influence of retention time on the breakage probability ($d_{32} = 2.18$ mm, $T_{bed} = 60$ °C, dry runs; symbols: experiment, lines: model described in Chapter 6 of Volume 2 in this series).

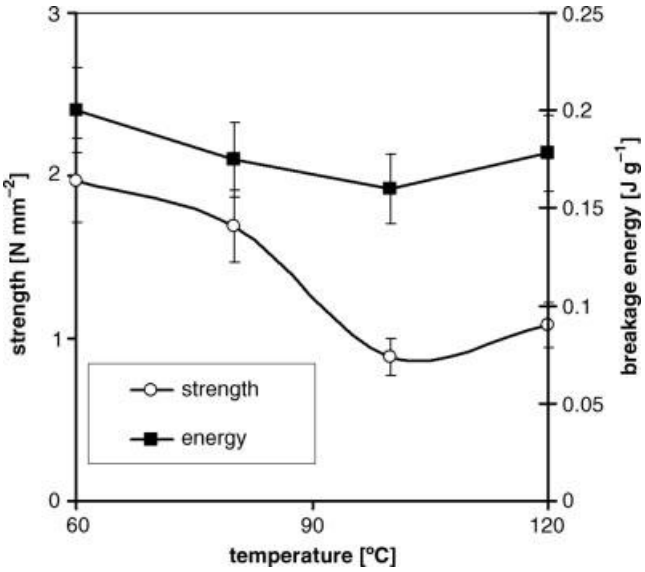

Fig. 7.31 Influence of the process temperature on the mean specific breakage energy and compressive strength of granulated particles (core material: zeolite 4A, shell material: sodium benzoate).

at 60 °C, whereas the lowest values were measured for a process temperature of 100 °C. A slight increase in particle strength was observed for temperatures higher than 100 °C.

A direct comparison of the surface morphology of the granules is presented in Fig. 7.32. Different temperatures result in a different microstructure. At lower gas temperatures a moderate drying rate can be expected, which provides more time for a crystalline, dense structure to evolve. This results in more elastic behavior and the higher particle strength that was observed at 60 °C. Particles granulated at higher temperatures have a smoother surface and seem to be more brittle.

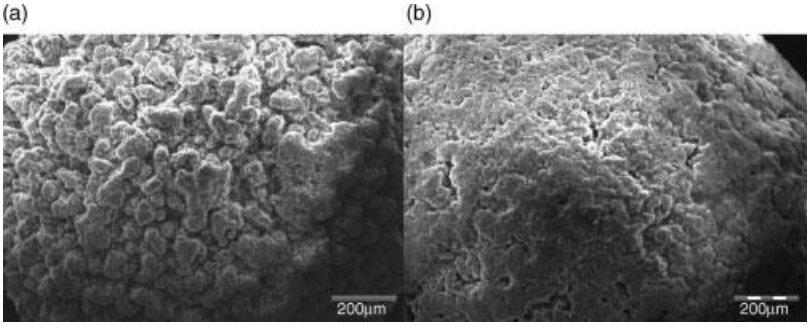

Fig. 7.32 SEM images of particles granulated at different temperatures: (a) 60 °C, (b) 120 °C.

In general, different process parameters have an influence on the solid phase formation around core particles. The structure of this shell influences, in turn, the properties of the resulting product, for example, the mechanical strength.

7.4.2 Catalyst Impregnation in Fluidized Beds

The loading of porous carrier particles with catalytically active ingredients usually requires several steps which have to be realized in several pieces of equipment, namely impregnation in a bath, separation of the solids by filtration, drying, and calcination. Here, the fluidized bed technology provides an alternative that combines all these stages in one apparatus. The studies of Hemati *et al.* (2001, 2003) and Desportes *et al.* (2005) prove the feasibility of manufacturing catalysts by spraying metallic precursor solutions on a porous support in a hot fluidized bed. The authors show that, according to the operation conditions, two different scenarios are possible:

- Soft drying under mild temperature conditions leads to homogeneous impregnation and catalyst deposition over the entire internal pore volume of the carrier.
- Intensive drying under high temperatures results in deposition only on the external surface of the support due to fast evaporation of the liquid.

The process is affected by various apparatus and process variables, such as nozzle configuration, gas inlet temperature, and flow rate, as well as material properties such as contact angle and surface tension, liquid viscosity and the texture of the solid particles. However, as the mentioned authors state, the solute distribution in the porous particles is mainly controlled by the following two time constants:

- The wetting time t_{wet}, which describes the transient penetration of liquid from the surface into the pores towards the particle center; the wetting time can be estimated from

$$t_{wet} = \frac{2\,\mu\,L^2}{\gamma\cos\theta\,r_{pore}}, \tag{7.28}$$

where μ is the liquid viscosity, γ the surface tension, θ the contact angle, L the effective pore length (particle radius multiplied by the tortuosity factor), and r_{pore} is the radius of the capillaries inside the particle.

- The drying time t_{dry} of a particle saturated with pure solvent under fluidized bed conditions.

Desportes *et al.* (2005) conducted experiments with coarse alumina particles (mean diameter 2.4 mm) to show that the homogeneity of solute distribution in the particles depends on the ratio between the two characteristic times t_{dry}/t_{wet}. Two different experimental conditions that correspond to fast drying and to slow drying (low and high values of t_{dry}/t_{wet}, respectively) were realized, as displayed in Tab. 7.4. Manganese nitrate was the precursor material. Material samples were removed after

Tab. 7.4 Experimental conditions for the investigation of solute distribution in porous fluidized particles according to Desportes *et al.* (2005).

Process parameter	Unit	Fast drying	Slow drying
Fluidization gas flow rate	$m^3 h^{-1}$	28	31
Gas inlet temperature	°C	60	78
Bed temperature	°C	45	27
Liquid flow rate	$g h^{-1}$	187	740
Solute mass fraction at the end of impregnation	%	12	40
t_{dry}/t_{wet}	—	4	11
Relative humidity	%	8	70

different processing times (Tab. 7.5) and analyzed by means of particle cross-section micrographs.

Figure 7.33 shows that, in the case of fast drying, the deposition takes place only at the surface of the particles. In the case of soft, slow drying, the solution penetrates into the particles in the form of a front that moves towards the center with increasing processing time. After sufficient time an even, homogeneous distribution of solute is obtained over the entire particle. Concerning the ratio between t_{dry} and t_{wet}, Desportes *et al.* (2005) conclude that for values below 10 a coating layer is deposited around the carrier, while for larger values the whole particle structure is penetrated by functional components of the sprayed solution.

Additional measurements by Desportes *et al.* (2005) indicate that the pore size distribution pattern of the initial support is conserved during increasing catalyst penetration (transition from S1 to S4 in Fig. 7.34). However, pore sizes are reduced, so that the specific surface area and the specific pore volume of the material gradually decrease (Tab. 7.5).

It should be noted that the quality of the products discussed in this section is mainly defined by catalytic activity and catalyst pellet efficiency, the latter being a measure of mass transport limitations within the particle. Depending on the

Tab. 7.5 Sampling time and sample characteristics under different drying conditions (F: fast drying, S: slow drying) according to Desportes *et al.* (2005).

Parameter	Unit	F1	S1	S2	S3	S4
Spraying solution time	h	3	0.5	1	1.5	3
t_{dry}/t_{wet}	—	4	11	11	11	11
Relative humidity	%	8	70	70	70	70
Specific pore volume	$cm^3 g^{-1}$	0.39	0.29	—	0.25	0.22

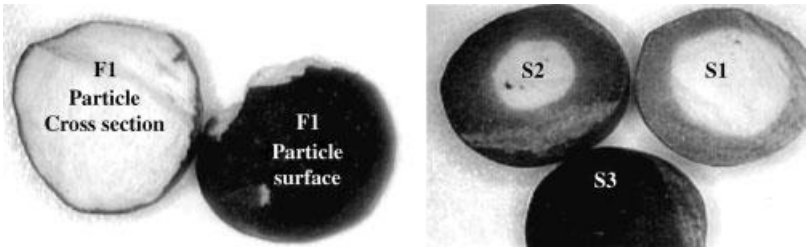

Fig. 7.33 Microscope pictures of alumina carrier particles with a metal precursor obtained under different drying conditions (F: fast drying, S: slow drying) (Desportes *et al.*, 2005).

reaction to be conducted and the type of reactor to be used, a shell catalyst or a full catalyst may be the right solution. As shown, both types of supported catalysts can be produced in spray fluidized beds by adjusting the intensity of drying, which can be easily done by setting relevant operation parameters. Therefore, there is an immediate, direct connection between drying and the quality of the formulated product.

Drying and liquid penetration are also important for the process already discussed in Section 7.3.3, namely spray fluidized bed agglomeration. The reason for this is that agglomeration takes place with the help of droplets sprayed on the particles, so that it slows down when such droplets are lost either by evaporation (drying) or by liquid penetration into the porous substrate. Influences of this kind can be captured very well with the help of respective micro-scale models integrated into discrete simulations, as we will see in Section 7.7.

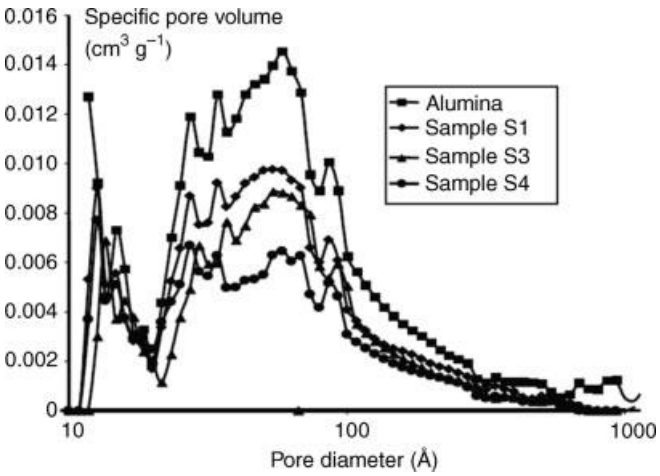

Fig. 7.34 Pore size distribution of alumina support particles under slow drying conditions for different spraying times (Desportes *et al.*, 2005).

7.5
Influence of Apparatus Design

7.5.1
Apparatus Design Features with an Influence on Product Quality

The design of central as well as peripheral elements of spray fluidized bed equipment has been discussed in considerable detail by Jacob (2007), so that it is sufficient to give here a brief summary before focusing on some special aspects of apparatus design with high relevance for product quality.

Important elements of the periphery of spray fluidized beds are:

- Equipment for processing gas handling. Here, one can distinguish between fresh air (single pass) and gas recycling (closed loop) systems. Such systems always include ventilators, pre-filtration and direct or indirect gas heating units. Frequent additional components are de-humidifiers and humidifiers, coolers and final filter units. The number and arrangement of ventilators can be used to adjust the pressure inside the process chamber relative to the ambient in order to, for example, avoid product contamination and guarantee product hygiene or, vice versa, to protect operators from toxic materials. Closed-loop set-ups are mandatory when inert gas (nitrogen) has to be used instead of air to preserve the quality of products sensitive to oxygen, to avoid explosion risks or to fulfill emission limits, especially in regard to odor. Gas recycling is always combined with heat recovery to reduce the total energy demand and provides opportunities for weather independent operation in the case of sensitive processes. The split ratio between fresh and recycled gas is an important parameter for the operation of such systems. Avoidance of undesired condensation, fouling and hygienic risks are crucial issues.
- Outlet gas handling. The most important aspect of outlet gas handling is the removal of dust, which can be achieved by internal filters, external filters or wet scrubbers, or a combination of these. Internal filters are textile bags or cartridges placed in the exhaust chamber of the fluidizing unit. They can be cleaned by mechanical shaking or by reverse gas flow (back-purge), whereby the dust falls down into the fluidized bed. Subdivisions of the exhaust chamber in combination with flaps allow cleaning of some filters while simultaneously operating some others, so that the process need not be interrupted.
- Solids handling facilities. Depending on the mode of operation (batch or continuous), various pieces of equipment can be used for charging or discharging the particulate material, such as flaps, rotary valves, dosing screws, overflows (weirs), discharge pipes, gas distributors that can be folded down or turned aside, exchangeable material containers, chutes, and pneumatic conveying units. However, solids handling is more than simple charging and discharging – especially in continuous spray fluidized bed processes. To guarantee the right particle size of the outlet product classifying discharge systems – such as tubes with counter-current, upwards oriented gas flow or zig-zag-sifters – may be used. Alternatively

or additionally, the outlet solids can be fed to a two-deck sieve that separates oversized and undersized particles from the final product, which is the fraction remaining between the two sieve decks. Undersized grains can be recycled to the process, and the same can be done with the oversized fraction after milling or crushing. This solids recycle is extremely important for granulation processes, because the fine-grained recycle particles serve as seeds (nuclei). Such nuclei are necessary for restarting particle growth and stabilizing the process towards a steady-state particle size distribution at the outlet. Feeding seed material from external sources (usually spray dryers) is the alternative to solids recycle. In both cases, seeds generated in the process chamber by overspray (droplets that dry out before reaching the surface of fluidized particles), attrition or breakage must also be considered.

The main central elements of spray fluidized bed equipment, which have also been discussed by Jacob (2007), are:

- The gas distributor. The gas distributor separates the plenum from the processing chamber of the fluidized bed. It must prevent the passage of particles and have enough mechanical strength to avoid excessive vibrations or deformation. Pressure drop in the distributor should be low, but sufficient for good fluidization of the particles. Common forms of the gas distributor are porous – usually sintered – plates, simple perforated plates or wedge-wire plates, which consist of profiles welded on supporting metallic elements. Distributors can direct the gas flow vertically to their surface (i.e., upwards) or impose another angle, depending on the orientation of their perforation or gaps between profiles. Distributors with a gas flow angle other than 90° blow the particles in a certain direction, providing a conveying or transport effect.
- The process chamber. The chamber where particle fluidization and droplet spraying take place can have different footprint cross-sections, from circular to lengthy rectangular. The cross-sectional area can remain constant or increase in a vertical direction, leading to various conical or prismatic geometries. Furthermore, the process chamber can be uniformly open or divided by partitions in different ways. The gas-inlet chamber and exhaust chamber usually follow the segmentation of the process chamber.
- The spray system, consisting of nozzles and liquid feed lines. Nozzles are usually specified by the average size and size distribution of the droplets that they produce, by their spray pattern (full cone, hollow cone, flat jet), the spray angle, the average and the distribution of droplet velocity, and the range of possible liquid feed rates. Atomization of the liquid takes place by contact with high-velocity gas (pneumatic or binary nozzles) or by expansion from high pressure (hydraulic nozzles). Alternatively, rotating discs or piezoelectric elements that vibrate with a high frequency can be used to disperse the liquid into droplets. Pneumatic nozzles are the commonest type for applications of the fine chemical, pharmaceutical or food industries. The nozzles can be installed to spray from above on, or from below in the fluidized bed (denoted by "top spray" and "bottom spray," respectively). Additional options are provided by horizontal or tangential spray.

Placement and orientation of the nozzles have an influence on the extent of possible overspray as well as on the tendency of – undesired – deposit formation on the atomizing devices and their supporting structure. Moreover, there is a more or less strong interaction between nozzle and fluidization flow. As to the number of nozzles, it can vary from one in small units to dozens in large industrial plants, including the possibility of multi-head nozzles. When many nozzles are used, their arrangement in, for example, arrays, and the distribution of the liquid feed become critical issues. Modern liquid feed systems not only achieve a controllable and safe metering of liquid, but also provide uniform conditions among multiple nozzles and enable the detection of malfunction by, for example, fouling of individual atomizers.

Each of the mentioned main constructive elements of spray fluidized bed equipment can be used to manipulate product properties in the desired direction. For example, droplet size and spray pattern have an influence on the particle wetting and on the local liquid distribution in the fluidized bed – thus also on particle growth kinetics, the type of particle size enlargement (agglomeration in comparison to granulation and coating) and product properties (e.g., particle porosity and density, and surface morphology).

However, even more opportunities for product design result from combining manipulations of the gas distributor, the process chamber and the spray system with each other. In the following, three examples of such combined manipulations will be briefly discussed, which result in Wurster equipment, in so-called ProCell units, and in lengthy rectangular ("horizontal") fluidized beds.

Wurster equipment is named after Dale Wurster – a professor at the Madison-Wisconsin University who worked on particle and tablet coating in the 1950s (see for example, Wurster (1959)). A typical configuration of such equipment is depicted in Fig. 7.35. As the figure shows, it combines the following aspects:

- A slightly conical process chamber with a tubular partition placed in the center of it, at some distance from the distributor plate;

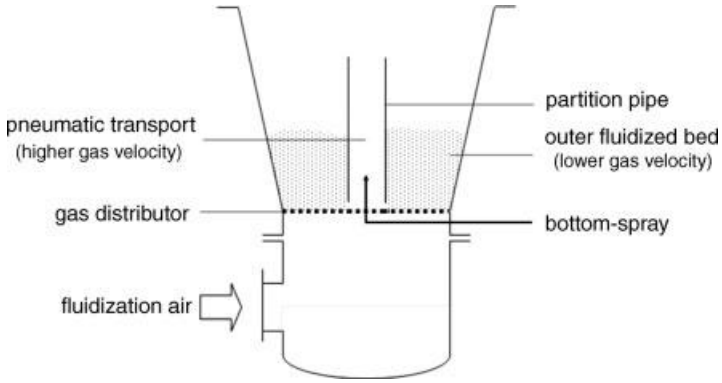

Fig. 7.35 Schematic representation of Wurster coater.

- Bottom spray in the tubular partition;
- A segmented gas distributor plate with higher open cross-section below the Wurster partition than in the outer region of the equipment.

The higher open cross-section in the center of the distributor plate results in a high gas velocity in the Wurster partition. Particles are transported pneumatically in a vertical direction inside the tube, while being sprayed with liquid. The uniform, one-dimensional character of the flow field reduces the number of interparticle collisions and provides similar residence times for all particles in the tube. Consequently, every particle is covered with a liquid film of approximately the same thickness, whereas agglomeration between the particles is suppressed. As soon as the particles leave the tube, they fall in the outer bed region, where they have time to dry under slowly bubbling fluidization conditions due to a much lower gas velocity. Then, the particles return to the Wurster tube through the gap between this tube and the distributor plate, and the cycle is repeated. The process is quite adequate for the application of uniform coatings on particles, so that it finds ample use in, for example, the pharmaceutical industry. The circulation of solids between the two compartments of the equipment (Wurster tube and outer bed) can be controlled by variation of the geometrical parameters.

An even more radical deviation from the classical concept of fluidized beds is realized in units such as those depicted in Figs. 7.36 and 7.37. The design is based on a patent by Mörl *et al.* (2002), which was successfully put on the market by the Glatt Co., Weimar, Germany, under the name ProCell (Jacob, 2009). As the figures show, ProCell does not have any distributor plate. Instead, the air comes in by means of two gaps created between two throttle cylinders (drum or valve rollers) placed symmetrically at both sides of a central profile (partition). Each drum has a flat cut, so that the size of the air inlet gap and the air inlet velocity can be adjusted by simply rotating the drum. The chamber of the equipment is triangularly prismatic. Combination of this

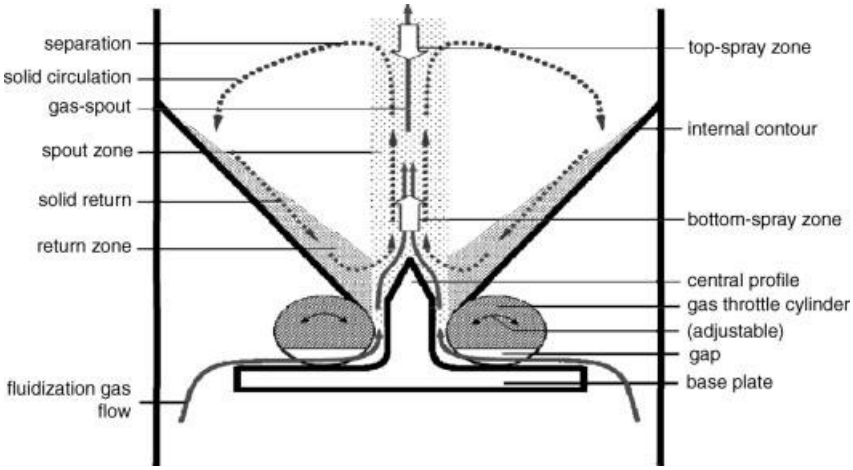

Fig. 7.36 Scheme of ProCell spouted bed apparatus.

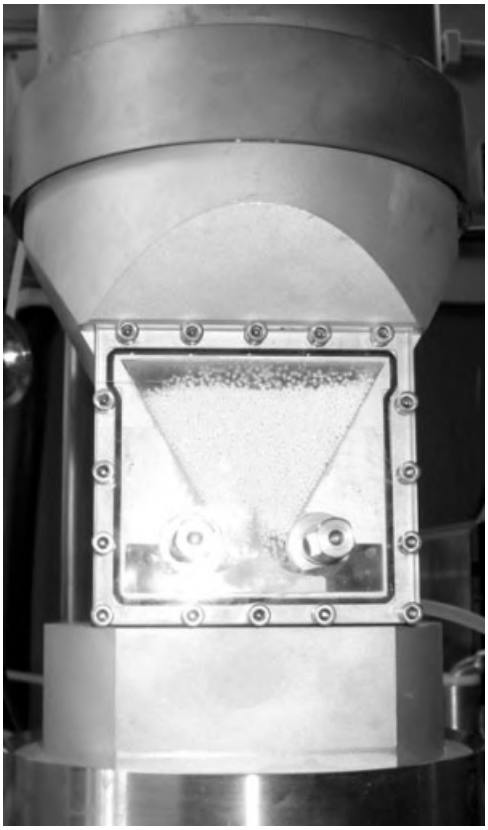

Fig. 7.37 Lab-scale ProCell model, as used by Hoffmann *et al.* (2011) for mass transfer measurements.

specific chamber geometry with the air inlet and the central partition leads to spatially correlated spouted bed flow patterns. The central partition unit combines the gas flow coming from the right with the gas flow coming from the left into a flow field that is symmetrical to the central plane and vertically oriented in the vicinity of this plane, in the typical form of a spout or jet. Spraying is performed in the spout, either from above or – more frequently – from below, at the tip of the partition (Fig. 7.36). The recirculation of solids to the spout is provided by the side contour (planar sides of the triangular prism).

A great advantage of ProCell is that it enables the processing of otherwise untreatable solids: materials with a broad particle size distribution, very small or very large size or density, irregular shape or sticky surface (Jacob, 2009). The apparatus has self-cleaning features. Moreover, it is easy to implement indirect heating at the central partition, or even cooling during the return of solids along the side contour. Due to the triangular shape of this contour, the apparatus can be operated with less hold-up and – in the continuous mode – with less residence time than conventional fluidized bed units, which means less deactivation of

sensitive ingredients. Finally, experiments conducted by Hoffmann *et al.* (2011) show that heat and mass transfer between the particles and the gas in ProCell equipment are – in terms of overall efficiency – much more intensive than in conventional fluidized beds or in conventional spouted beds. This is attributed to the very high air velocities in the gas inlet. Since the apparatus is prismatic, it can be scaled up by prolongation in the third (horizontal) direction. Additionally, the described design can be replicated in the lateral direction by use of more than one partition profile in parallel. To facilitate the construction of lengthy horizontal units one can refrain from the adjustability of the air inlet, using constant width gaps instead of the roller valves. Different zones can be defined in such lengthy equipment by subdivision of the plenum and by schemes of nozzle placement along the device.

Different zones can also be defined in combination with distributor plates, as depicted in Fig. 7.38. Such a horizontal fluidized bed unit has an extended rectangular design of the process chamber. The gas distributor usually has a transport effect, moving the solids from the inlet to the outlet in continuous operation. Segmentation is performed by subdivision of the plenum and by the placement, or not, of nozzles. Since each of the different compartments of the plenum can be equipped with a separate gas supply, it is possible to conduct various sequences of processing steps. For example, a product can be granulated in the first and second segments, dried in the third, and cooled in the final fourth section (Fig. 7.38). The fluidization chamber may be open (as in Fig. 7.38), or it can follow the segmentation of the plenum by means of partitions (weirs). Solids transportation from one segment to the next takes place as overflow or underflow. In the case of underflow, openings that cover all the width of the equipment or just a part of it can be used. Smaller underflow openings (so-called "rat holes") can be placed to the right

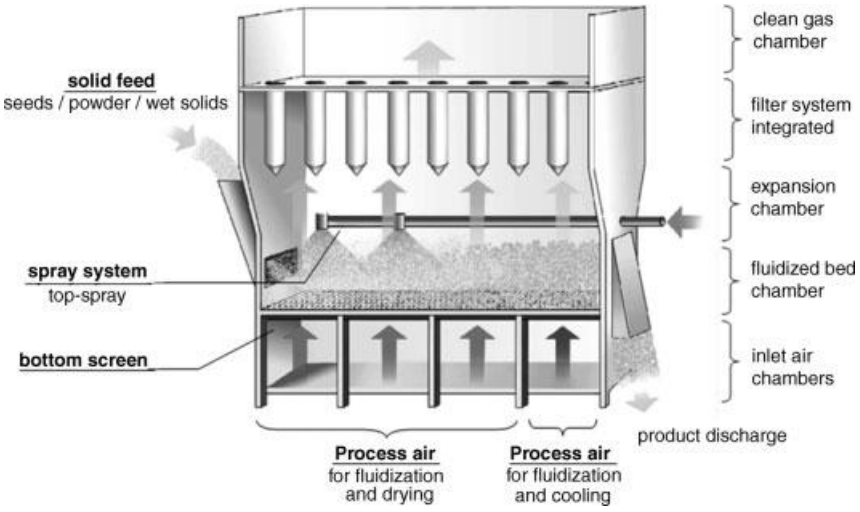

Fig. 7.38 Horizontal fluidized bed unit with segmentation.

and to the left in alternating sequence, in order to create – in combination with appropriately aligned transport distributor pieces – a meander-like path of solids motion. The nozzles can be arranged in top-spray or in bottom-spray, with constant or variable spray rate along the equipment. An important aspect of chamber design and segmentation is that the residence time distribution of the solids can be varied within a broad range – from the well-mixed behavior, which is typical for circular apparatuses, to nearly plug flow conditions. The aspect of residence time distribution will be discussed further in the following section.

7.5.2 Residence Time Distribution

The residence time of particles in fluidized bed processes has a huge influence on the product characteristics. A prominent example is fluidized bed drying, where the residence time determines the product moisture, which is an important factor for storage stability (see Chapter 1 in Volume 2 of this series). Another example is fluidized bed coating. The goal of fluidized bed coating may be to place an active ingredient, for example, an enzyme, on inactive carrier material (Hede *et al.*, 2009). If the residence time of the carrier cores is too short, then only an insufficient amount of active ingredient is deposited, and the resulting product is ineffective. On the other hand, if the residence time is too large, an overdose of active ingredient is applied. Additionally, partial inactivation of the enzyme by thermal exposure or agglomeration can take place. In both cases, the product may not fit the specifications for its application.

Appropriate equipment design is one way to guarantee the desired product properties by manipulation of the residence time of particles in fluidized bed processes. Moreover, it is necessary to identify suitable process inputs with an influence on residence time for use in feedback control loops.

An appropriate design may be that of horizontal equipment, as the one depicted in Fig. 7.38. Due to the fluidization air, particles move along the chamber of such equipment, establishing a complex velocity field. Additionally, rising bubbles of gas mix the solids. The air velocity distribution in a horizontal direction has, therefore, great influence on both the transport and the mixing of particles along the bed. To quantify particle motion, simulations with computational fluid dynamics (CFD) were conducted for a three-dimensional model of an industrial pilot plant within the ANSYS FLUENT environment (version 6.2). No partitions were present in the chamber – in close correspondence to the geometry shown in Fig. 7.38. A Eulerian approach was adopted for the granular phase in the simulations.

In Fig. 7.39 the resulting volume fractions of the disperse phase are shown for different total volume flow rates of air. An increase in the bed height and more uniform bubbling can be observed in the process chamber at higher air velocity. Moreover, the higher intensity of particle movement leads to a significant change in the dynamic behavior of the apparatus: At higher particle velocities more particles are ejected into the freeboard region and are distributed along the whole process

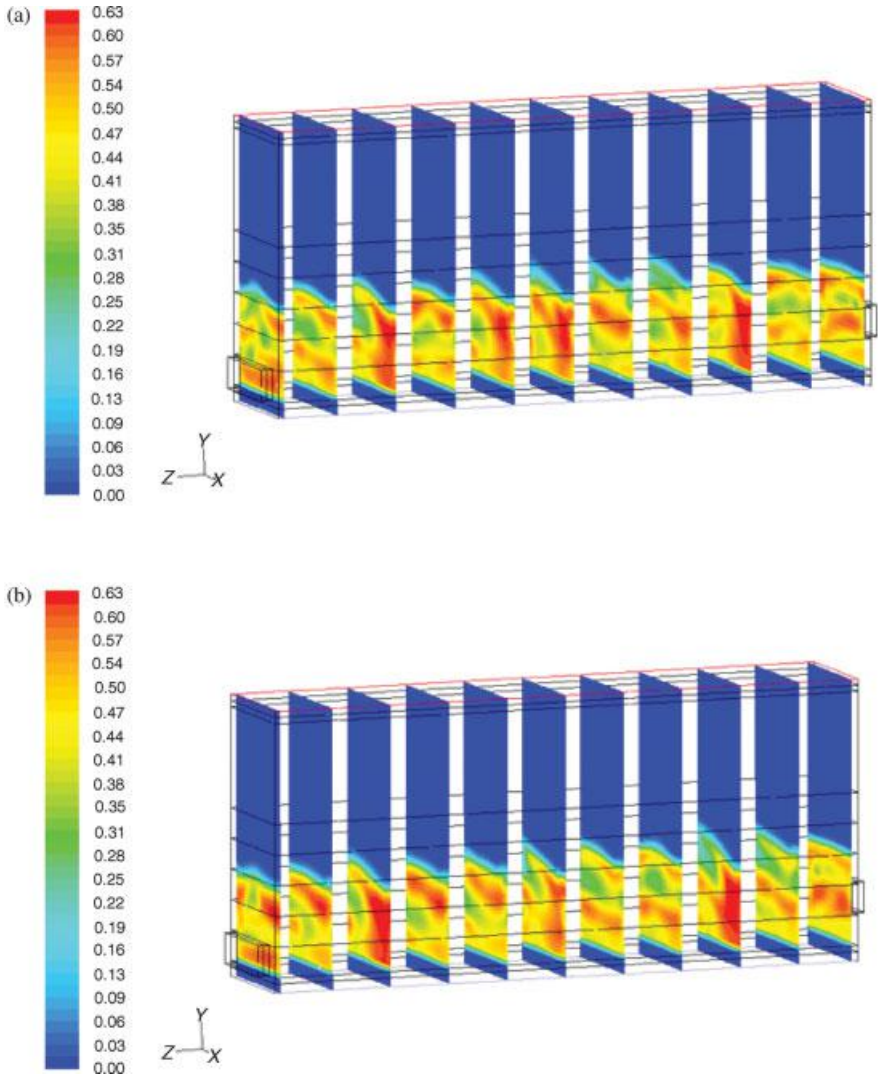

Fig. 7.39 Contours of solids volume fraction in horizontal equipment for volume flow rates of fluidization air at (a) 500 $m^3 h^{-1}$, (b) 700 $m^3 h^{-1}$.

chamber. This will have a direct influence on the residence time of particles in the bed and thus on the product quality at the outlet of the apparatus.

In order to quantify the influence of the gas flow rate on the residence time of the particles a simple model can be used that represents the horizontal apparatus by a series of continuously operated stirred tank reactors (CSTRs). The principle of this model is illustrated in Fig. 7.40. The size (length) and number of the tanks express the intensity of back-mixing (mixing in the direction of solids transport). They are fictitious for an open process chamber (as in Fig. 7.38), but may correspond to

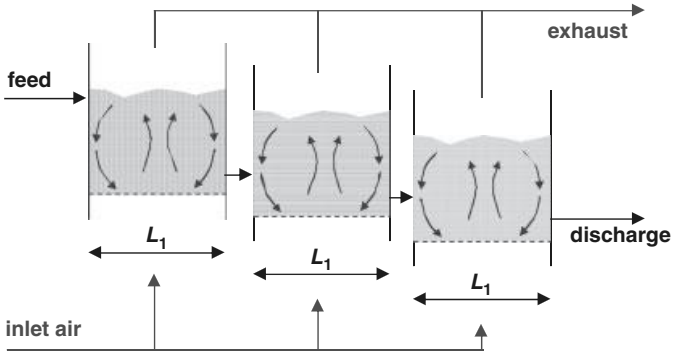

Fig. 7.40 Series-of-tanks model for horizontal equipment.

physically existing individual compartments in the case of built-in partitions (weirs).

The average residence time under continuous, steady-state conditions results from the mass of particles in the fluidized bed M_{bed} and the mass flow rate of solids $\dot{M}_s$:

$$\bar{\tau} = \frac{\dot{M}_s}{M_{bed}} \tag{7.29}$$

Using a correspondingly defined dimensionless residence time

$$\tau_r = \frac{\tau}{\bar{\tau}} \tag{7.30}$$

the normalized residence time distribution $E(\tau_r)$ in a series consisting of N stirred tanks can be derived analytically. It is:

$$E(\tau_r) = \frac{N^N}{(N-1)!}\tau_r^{N-1}\exp(-N\,\tau_r) \tag{7.31}$$

Figure 7.41 shows that very different residence time distributions are obtained for different numbers of tanks in series. In order to obtain a narrow residence time distribution with limited variance a high number of effective or real compartments may be necessary.

To find out the effective number of compartments that corresponds to the horizontal equipment of Fig. 7.38, tracer experiments were conducted. After a prescribed time at steady operating conditions a granular tracer substance was added to the solid feed stream. Samples were taken at the discharge of the plant at defined time intervals and analyzed by means of pH measurement after dissolution in de-mineralized water. The pH value of the solution corresponds to the concentration of tracer, and can be used to calculate residence time curves. Measurements were carried out for the two already mentioned total gas flow rates of 500 and 700 $m^3\,h^{-1}$ under otherwise the same conditions (mass flow rate of solids: 20 $kg\,h^{-1}$, bed mass: 25 kg, tracer mass: 5 kg, test duration: 140–150 min).

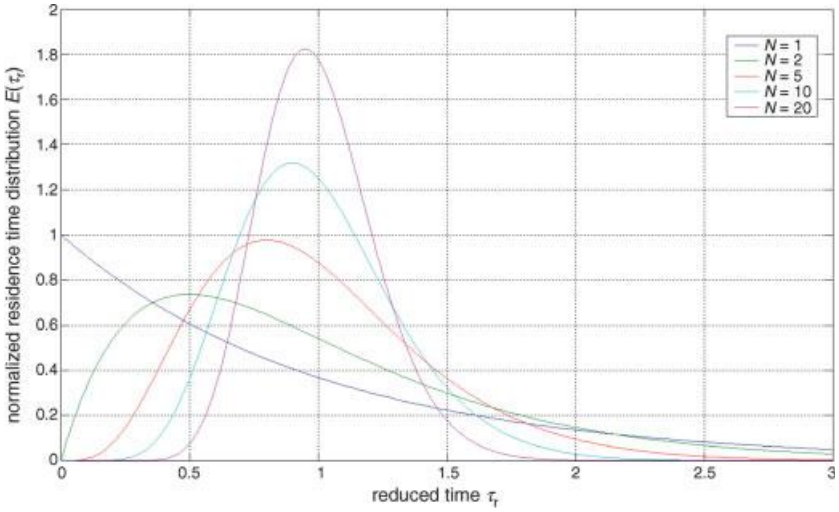

Fig. 7.41 Residence time distributions of perfectly stirred tanks in series, depending on the number of tanks.

The results are plotted in Fig. 7.42 and make clear that the air flow rate has a direct influence on the residence time distribution. With increasing air flow rate (Fig. 7.42b) the fluidization intensity increases and the distribution widens. This is in qualitative agreement with the previously discussed CFD results. Normalization and comparison with the tanks-in-series model in Fig. 7.43 shows a difference in the shape between measured curves and standard residence time distributions. Specifically, there is a time delay at the beginning of the experiments which is independent of fluidization velocity. This behavior is probably related to the fact that the outlet rotary valve of the apparatus was operated at low speed, producing some jam of material in the connection between the bed outlet and the valve. Consequently, tracer particles reached their sampling point immediately after the valve with some delay. Additionally, the shape of the measured curves is modified in comparison to the theoretical curves by a shift of their maxima to lower values of time. A possible reason for this shift is the use of an air distribution plate with transport effect in the experiments. This distributor type is designed to create a horizontal air velocity component pushing the solids to the outlet side of the process chamber. Therefore, distributions of hold-up along the equipment, which have not been accounted for in the evaluation, may have been present.

If one attempts – despite the mentioned qualitative deviations – a guess of the number of effective compartments on Fig. 7.43, something like $N = 2$ would be the outcome. Consequently, the equipment of Fig. 7.38 would perform in the sense of a narrow residence time distribution better than a cylindrical fluidized bed (which corresponds to just one perfectly stirred tank), but would still give quite broad distributions of product properties at the outlet. To squeeze such distributions towards uniformity, partitions (weirs) can be placed in the fluidization chamber. Additionally, the equipment can be further elongated. The combination of both

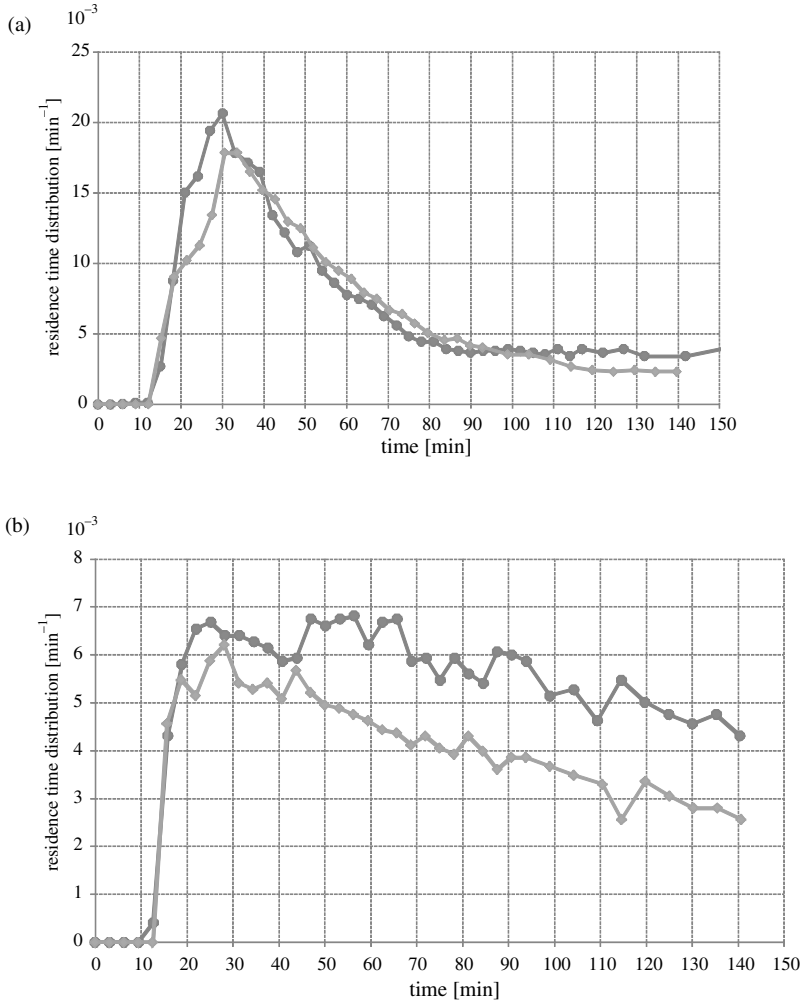

Fig. 7.42 Residence time distributions measured in horizontal equipment for volume flow rates of fluidization air at (a) 500 $m^3 h^{-1}$, (b) 700 $m^3 h^{-1}$; (two measurements for each gas flow rate under essentially the same conditions).

measures leads to horizontal fluidized beds with the residence time behavior of many (10, 20, or more) tanks in series. In fact, Baker and Lababidi (2010) point out that large industrial equipment of this type comes close to the limit of $N \rightarrow \infty$, which would mean plug-flow of the solids. Fyhr *et al.* (1999) report the value of $N = 10$ for a horizontal fluidized bed dryer. Nilsson and Wimmerstedt (1988) use the dispersion model instead of the tanks-in-series model to express the mixing of solids in a longitudinal direction, and present – based on measured data – a correlation for the respective dispersion coefficient. Since the dispersion model and the tanks-in-series model are equivalent to each other, this correlation can be used to estimate the effective number of compartments for technical applications.

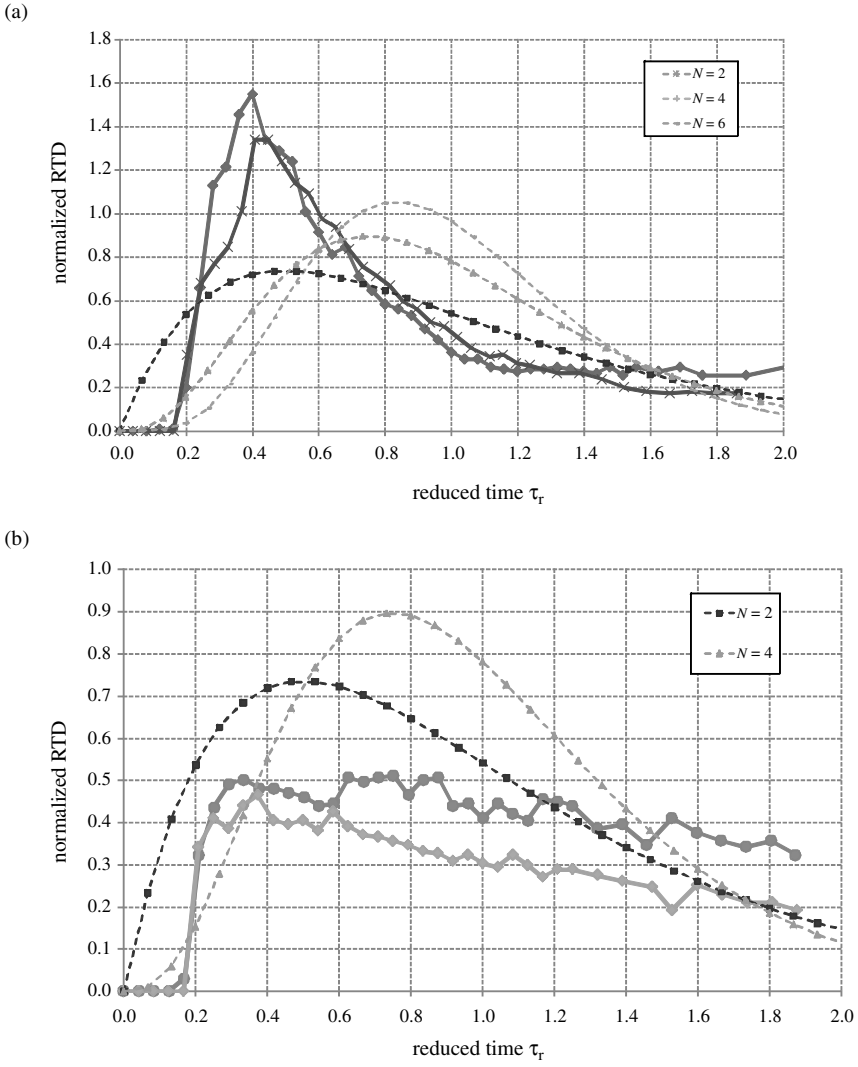

Fig. 7.43 Normalized residence time distributions derived from the measured data of Fig. 7.41 in comparison with the tanks-in-series model at (a) 500 $m^3 h^{-1}$, (b) 700 $m^3 h^{-1}$ of fluidization air.

In addition to partition and elongation, the gas flow rate in the different compartments of horizontal fluidized bed equipment can be used to manipulate the residence time distribution of the particles and, thus, the quality of the outlet product. The use of CFD can support the design of compartments, partitions and weirs. Not only the here briefly presented two-fluid (Euler–Euler) approach, but also Euler–Lagrange approaches (so-called discrete particle models, DPM) can serve this goal, as will be discussed in Section 7.5.4.

7.5.3
Dispersive Growth in Batch Granulation

In many processes, such as coating or layering granulation, the width (or variance) of the particle property distribution is an important measure of product quality. The variance in particle size is directly related to the variance in thickness of the coating layers that has great influence on the product characteristics, for example the release time of active ingredients in pharmaceuticals.

Coating, as well as layering granulation, has a well-established basis in mathematical modeling. Using a population balance approach for the particle property distribution, for example the distribution of size d, yields for the number density n the following type of population balance equation

$$\frac{\partial n}{\partial t} + \frac{\partial (Gn)}{\partial x} = \dot{N}_{\text{in}} - \dot{N}_{\text{out}} + P \tag{7.32}$$

with corresponding initial and boundary conditions. Here, G denotes the growth rates of the particles, $\dot{N}_{\text{in}}$ is the flow density of particles entering the balance volume, and $\dot{N}_{\text{out}}$ is the flow density of particles leaving the system, for example by an outlet. Particle production processes, for example agglomeration and breakage, are collected in the net production density P. In the case of coating (or layering) only, this term is not present in the balance equation.

In modeling, the growth rate G is commonly considered to be independent of the particle property. For example, Mörl *et al.* (2007) assume that the growth velocity of particles is directly related to their surface area in the fluidized bed, to obtain for spherical particles

$$G = 2\frac{\dot{M}_{\text{sus}}}{\varrho_{\text{s}}\,\pi\,\mu_2} \tag{7.33}$$

Here, $\dot{M}_{\text{sus}}$ denotes the mass flow rate of solid material entering the system with the spray, ϱ_{s} is the density of the solidified layers, and μ_2 is the second moment of the particle size distribution, so that $\pi\,\mu_2$ equals the total particle surface area. The population balance equation then reads as

$$\frac{\partial n}{\partial t} + G\frac{\partial n}{\partial d} = \dot{N}_{\text{in}} - \dot{N}_{\text{out}} + P \tag{7.34}$$

This fundamental assumption simplifies the structure of the mathematical problem significantly. Additionally, it is also backed by various experimental results – see for instance the references in Mörl *et al.* (2007).

Under the assumption of property-independent growth of particles, Eq. 7.34 represents a quasi-linear transport equation. Although the transport velocity can vary with process time, it is assumed to be the same for each particle at every point in time. This ultimately results in the effect that the initial distribution (at $t = t_0$) is shifted along the property coordinate, see Fig. 7.44. The shape of the distribution is

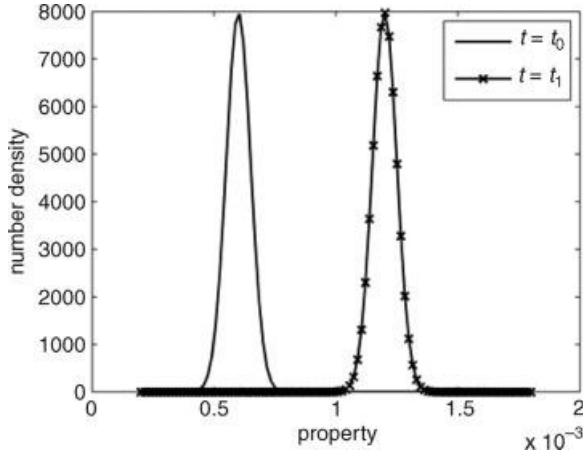

Fig. 7.44 Evolution of particle size distribution under a property independent growth law; the shape of the distribution is conserved.

preserved during this transport, due to the assumption of the property independence of the growth rate.

However, in various coating and granulation experiments a change in the shape of the distribution is observed, for example a dispersion of the distribution. In Fig. 7.45 the results of five different coating experiments are shown, which were conducted in: Wurster equipment, a conventional fluidized bed apparatus (FB) in top and bottom spray configuration, and a spouted bed apparatus (SB) in top and bottom spray configuration. Although identical initial conditions were used and the process conditions are comparable (see Tab. 7.6), different final distributions are achieved. This effect cannot be explained by the common model of Eq. 7.34, but it underlines the influence that different types of equipment with different flow patterns may have on the process result.

In order to capture deviations from property independent growth in terms of the population balance equation, two possibilities are imminent. First is the introduction

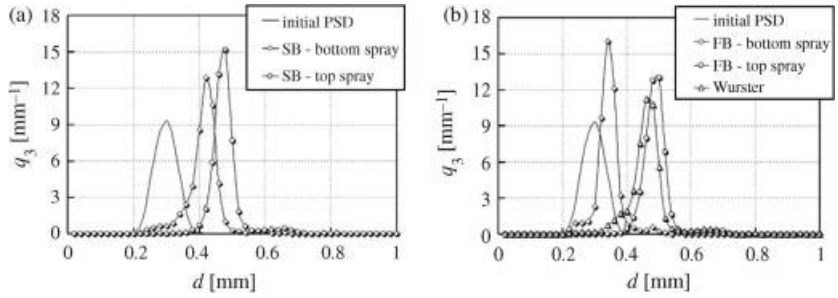

Fig. 7.45 Results of coating processes in apparatuses of different design: (a) spouted bed (SB), (b) Wurster equipment and conventional fluidized bed (FB); Starting from an identical initial distribution, different final distributions are achieved under comparable process conditions.

Tab. 7.6 Process conditions for the fluidized bed coating experiments depicted in Fig. 7.45.

Bed material	Cellets
Solution	Na-benzoate, 30 wt%
Spraying rate	$18\,g\,min^{-1}$
Fluidization gas flow rate	$70\,kg\,h^{-1}$ for Wurster and FB, $100\,kg\,h^{-1}$ for SB
Gas temperature	90 °C
Nozzle pressure	2.5 bar
Initial bed mass	1 kg

of new growth models – of the same structure as Eq. 7.33, but not property-independent – using higher moments of the distribution (Hoffmann *et al.*, 2010). Introducing generalized growth rates

$$G_i = 2\frac{\dot{M}_{sus}\, d^{i-2}}{\varrho_s\, \pi\, \mu_i} \tag{7.35}$$

which are based on an arbitrary moment μ_i of the particle size distribution, the total growth rate of particles G can be defined as:

$$G = \sum_{k=0}^{N} \lambda_k\, G_k \quad \text{with} \quad \sum_{k=0}^{N} \lambda_k = 1 \tag{7.36}$$

The constraint on the choice of the parameters λ_k is due to the required mass conservation in the model. A selection of $\lambda_2 = 1$ leads to the well known surface-proportional growth law (Eq. 7.33).

This approach can come close to experimental results, as Fig. 7.46 shows. The data used for this comparison were measured for batch granulation in a conventional

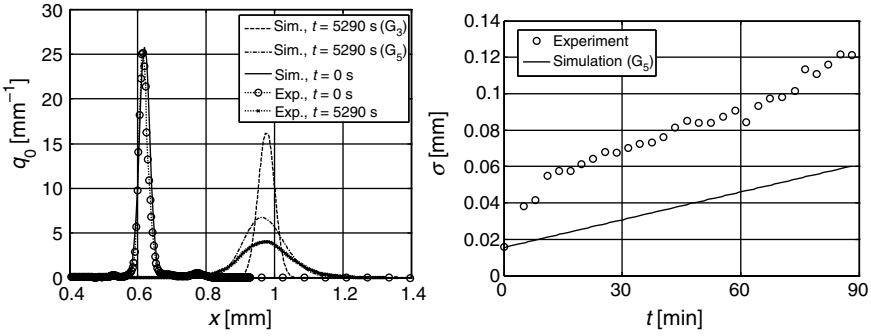

Fig. 7.46 Comparison of experimental and simulation results for higher order growth models. Plotted are the approximations for volume-proportional growth ($\lambda_3 = 1$) and the fifth-order model ($\lambda_5 = 1$), which can be interpreted as mass flux of particles during sedimentation from a suspension.

Tab. 7.7 Process conditions for the experiment depicted in Figs. 7.46 and 7.48, and parameters of the two-compartment model.

Bed material	γ-Al_2O_3
Solution	Na-benzoate, 30 wt%
Spraying rate	$100\,ml\,min^{-1}$
Fluidization gas flow rate	$500\,kg\,h^{-1}$
Bed temperature	80 °C
Atomizing gas flow rate	$50\,kg\,h^{-1}$
Initial bed mass	4 kg
Volume fraction spray zone	2%
Mean residence time spray zone	4 s

top-spray fluidized bed with the process conditions summarized in Tab. 7.7. There is a striking difference between these data and the behavior illustrated in Fig. 7.44, because the size distribution broadens very significantly with time (the standard deviation σ increases). This observation is analogous to the broadening of concentration profiles while moving along a chromatographic column. It can, thus, be denoted by dispersive growth, whereby the dispersion does not take place in space, but along the property coordinate. However, the higher order growth rates used to approach the measured results in Fig. 7.46 are hard to interpret in terms of physical relations. The parameters needed have to be identified and tuned in a cumbersome plant-specific procedure, which complicates statements on the generality and scalability of the results.

The second approach favors the use of compartment models to describe the evolution of the property distribution. It has the virtues of needing only a limited number of new parameters to be applied and using the property-independent growth law to achieve good results.

In the following, a compartment model for the layering granulation of particles in a fluidized bed is presented, based on the recent work of Silva *et al.* (2010). In Fig. 7.47 the principal sectioning of the fluidized bed according to this model into a spraying zone and a drying zone is depicted. The fraction of the total volume occupied by the spraying zone is denoted by α, so that the volume fraction of the

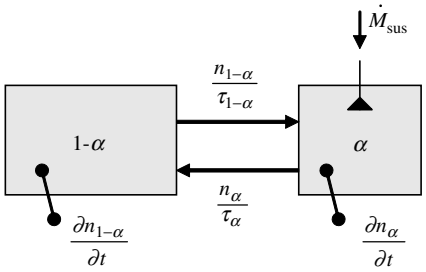

Fig. 7.47 Two-compartment model of a fluidized bed with a spraying zone and a drying zone.

drying zone is $1-\alpha$. Only particles that are inside the spraying zone are sprayed with liquid. Due to the fluidization, these particles are then transported (after a certain mean residence time τ_α) into the drying zone, where the sprayed liquid dries and new solid layers are built up.

In mathematical terms the system of Fig. 7.47 is described by two population balance equations, one for each of the two compartments:

$$\frac{\partial n_\alpha}{\partial t} + \frac{\partial (G n_\alpha)}{\partial x} = -\frac{n_\alpha}{\tau_\alpha} + \frac{n_{1-\alpha}}{\tau_{1-\alpha}} \tag{7.37}$$

$$\frac{\partial n_{1-\alpha}}{\partial t} = +\frac{n_\alpha}{\tau_\alpha} - \frac{n_{1-\alpha}}{\tau_{1-\alpha}} \tag{7.38}$$

where n_α is the particle size density distribution in the spraying zone and $n_{1-\alpha}$ is the distribution in the drying zone of the fluidized bed. The parameters τ_α and $\tau_{1-\alpha}$ are the mean residence times in the spray and drying zones, respectively. They incorporate information on the flow regime (particle exchange rates), and are also directly dependent on apparatus design, for example on nozzle placement and the dimensions of the spraying cone.

As was shown by Silva *et al.* (2010), these model equations can be solved analytically for special initial conditions to gain information on the evolution of the mean and the variance of the initial distribution during the layering process. The same authors also provide analytical solutions for the particle size distributions and experimental results.

Particle size distributions obtained by the two-compartment model are depicted in Fig. 7.48, along with the same experimental results as in Fig. 7.46 (Tab. 7.7). The simulated standard deviation is also compared to the experimental standard deviation in this figure, and a good agreement between the results can be observed.

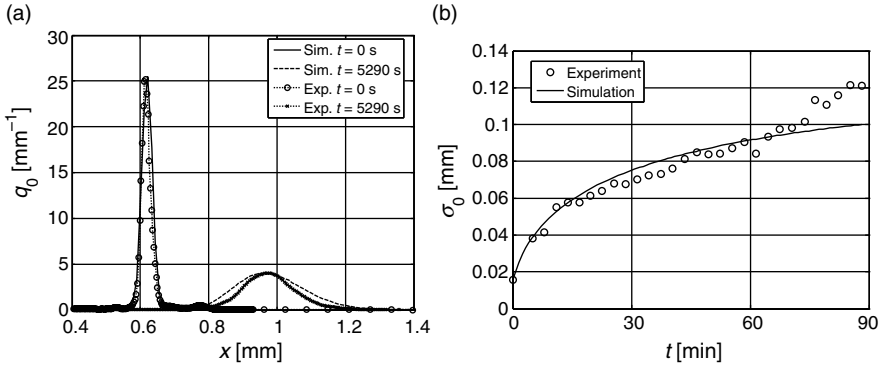

Fig. 7.48 Comparison of experimental and simulation results for the two-compartment model; (a) particle size distribution and (b) standard deviation are described well by the model with parameters as listed in Tab. 7.7.

The parameters to be estimated in this model are α, τ_α, and $\tau_{1-\alpha}$. Here, it is sufficient to know two out of three parameters, as the following equality holds from mass conservation arguments:

$$\frac{\tau_{1-\alpha}}{\tau_\alpha} = \frac{1-\alpha}{\alpha} \tag{7.39}$$

The mean residence times τ_α and $\tau_{1-\alpha}$ can either be calculated by CFD in the apparatus or determined by measurements, for example via particle image velocimetry (PIV, for a detailed description see Chapter 5 in Volume 2 of this series). The volume fraction of the spray zone α can be estimated from the apparatus dimensions, bed porosity, flow conditions, and the spraying cone of the nozzle.

Summarizing, conventional coating and granulation models that utilize property-independent growth laws are often not able to describe the experimentally observed temporal change in the variance of a given initial distribution. One way to extend the existing mathematical models is the introduction of new growth models which use higher moments of the distribution to describe the growth. However, these growth laws are often hard to explain on a physical basis, and the parameters necessary in order to apply the model are difficult to identify. Another way to derive dispersive growth behavior from population balances is to divide the fluidized bed into two interacting zones – a spraying zone and a drying zone – while still relying on the well-established property independent growth rate for the spraying zone. As was shown by experimental results, this approach is able to describe the observed change in the particle size distribution satisfactorily. Also, the necessary parameters can be inferred from the geometry of the apparatus and the hydrodynamic conditions. This leads to the conclusion that compartment models are suitable to describe a large class of coating and granulation processes in which a change in the variance of the property distribution is observed.

7.5.4
Discrete Particle Modeling of a Wurster Coater

As shown in the previous sections, the influence of residence time on the product quality – in particular on the variance of the PSD – can be significant. Moreover, it was shown that the residence time can be controlled by special design of the apparatus in the form of a spouted bed, Wurster coater or horizontal fluidized bed. In Section 7.5.2 a Euler–Euler approach was presented to study the velocity distribution of the solids in a continuously operated, horizontal fluidized bed. Another popular tool for the simulation of disperse systems is the Discrete Particle Model (DPM), which resolves the equation of motion for each individual particle considering the momentum exchange within the disperse phase due to particle collisions and with the gas phase. The DPM has been applied to fluidized bed processes by several authors (Tsuji *et al.*, 1993; Hoomans *et al.*, 1996), including some attempts at discrete modeling of fluidized bed spray granulation processes (Goldschmidt and Kuipers, 2003; Kafui and Thornton, 2008). The DPM method is still limited by the number of particles (order of magnitude: 10^6) that can be considered and process time (order of

magnitude: seconds) that can be simulated. Nevertheless, due to the rapid development of computer speed and memory, the size of the simulated systems has recently been significantly increased, so that now the DPM is a promising method.

7.5.4.1 Principles of the DPM

The fundamental equation of the DPM is the momentum equation of each individual particle with mass M_i and volume V_i, that can be described by Newton's second law

$$M_i \frac{\mathrm{d}\mathbf{v}_i}{\mathrm{d}t} = M_i \frac{\mathrm{d}^2\mathbf{r}_i}{\mathrm{d}t^2} = -V_i \nabla P + \frac{V_i \beta}{1-\varepsilon}\left(\mathbf{u}_g - \mathbf{v}_i\right) + M_i \mathbf{g} + \mathbf{F}_{\mathrm{contact},i} + \mathbf{F}_{\mathrm{pp},i} \tag{7.40}$$

where $\mathbf{v}_i$ is the velocity and $\mathbf{r}_i$ the position of the particle. The forces on the right-hand side of Eq. 7.40 are, respectively, due to the pressure gradient, drag, gravity, contact forces (i.e., forces during collisions) and relatively distant particle–particle interactions (for instance van der Waals forces). The inter-phase momentum transfer coefficient β is frequently modeled by combining the Ergun equation for dense regimes ($\varepsilon < 0.8$)

$$\beta = \frac{\mu}{d^2}\left(150\frac{(1-\varepsilon)^2}{\varepsilon} + 1.75(1-\varepsilon)Re\right) \tag{7.41}$$

and the correlation proposed by Wen and Yu (1966) for the more dilute regimes ($\varepsilon \geq 0.8$)

$$\beta = \frac{\mu}{d^2}\left(\frac{3}{4}c_\mathrm{d} Re \frac{(1-\varepsilon)}{\varepsilon^{2.65}}\right) \tag{7.42}$$

with

$$c_\mathrm{d} = \begin{cases} 24\left(\dfrac{1+0.15\ Re^{-2.65}}{\mathrm{Re}}\right) & \text{if Re} < 1000 \\ 0.44 & \text{if Re} > 1000 \end{cases} \tag{7.43}$$

where Re is the particle Reynolds number and ε is the gas volume fraction (porosity). Hill *et al.* (2001) and Beetstra *et al.* (2007) have developed own drag correlations based on Lattice–Boltzmann simulations, which should give a more accurate representation of the fluid–particle interactions in dense gas–solid flows for the price of higher computational effort. All correlations developed in this way until now are, however, limited to monodisperse or bidisperse (Beetstra *et al.*, 2007) arrays of spherical particles.

In the case of a collision between two particles, the contact forces are calculated according to a contact model based on the theory developed by Hertz (1882) for the normal impact and a non-slip approximation of the model by Mindlin and Deresiewicz (1953) for the tangential part of the contact force, as proposed by Tsuji *et al.* (1992). The normal contact force is

$$\mathbf{F}_{\mathrm{contact,N}} = -k_\mathrm{N} s_\mathrm{N}^{3/2}\mathbf{n} - \mu_\mathrm{N}\mathbf{v}_\mathrm{N} \tag{7.44}$$

Here, $\mathbf{n}$ is the normal unit vector and $\mathbf{v}_N$ is the relative velocity at the contact point. The elastic part of the contact force is represented by a non-linear spring, assumed proportional to the spring stiffness k_N and to $s_N^{3/2}$ (s_N: displacement). Additionally, to account for viscoelastic material properties that cause energy dissipation, a damping factor μ_N related to the coefficient of restitution is included in the model:

$$\mu_N = 2\alpha\sqrt{Mk_N}s_N^{1/4} \tag{7.45}$$

$$\alpha = \begin{cases} \dfrac{\ln e_N}{\sqrt{\pi^2 + \ln^2 e_N}} & \text{if } e_N \neq 0 \\ 1 & \text{if } e_N = 0 \end{cases} \tag{7.46}$$

The normal coefficient of restitution e_N is defined as the ratio of the rebound velocity to the impact velocity:

$$e_N = \sqrt{\frac{E_{kin,R}}{E_{kin}}} = \frac{|v_R|}{v} \tag{7.47}$$

Usually this value can be obtained from experiments. The symbol M in Eq. 7.45 denotes a combined mass. The tangential component of the contact force $F_{contact,T}$ is calculated analogously, as presented by Tsuji *et al.* (1992).

The gas phase is considered as a continuum. Usually, the geometry of the apparatus is discretized in mesh cells and the motion of the gas phase is calculated using volume-averaged Navier–Stokes equations. The influence of particles on the velocity profile of the gas phase is accounted for by adding a sink term to the momentum balance for the gas. To reduce the numerical effort and to avoid local extrema of the solids concentration, the gas flow field is resolved on a relatively coarse grid compared to the particle diameter. The side length of an average Eulerian grid element should be in the range of 10 times the particle diameter (Deen *et al.*, 2007).

7.5.4.2 **Parameters for the DPM Simulation**

A Wurster coater similar to the equipment of Fig. 7.35 was simulated by DPM. The original geometry and the meshed model are shown in Fig. 7.49.

To investigate the influence of design and process parameters on the fluid dynamics in the Wurster coater, DPM simulations were performed in 3D with 150 000 spherical particles. At a particle diameter of 2 mm and an average particle density of 1500 kg m^{-3}, this corresponds to a batch size of 0.94 kg. According to experimental results for γ-Al_2O_3, the coefficient of restitution for particle–particle and particle–wall collisions was set to 0.8 and kept constant during all simulations. The operating variables are summarized in Tab. 7.8. Notice that air comes through the distributor plate in the Wurster tube and in the annulus around this tube. The respective velocities can be different, corresponding to distributor segments with different porosity; they are given in Tab. 7.8 as multiples of the minimal fluidization velocity u_{mf}. Additionally, air is blown in the Wurster tube by a nozzle. Air velocity at the tip of this nozzle is denoted by the atomizer or spout velocity. In a series of case

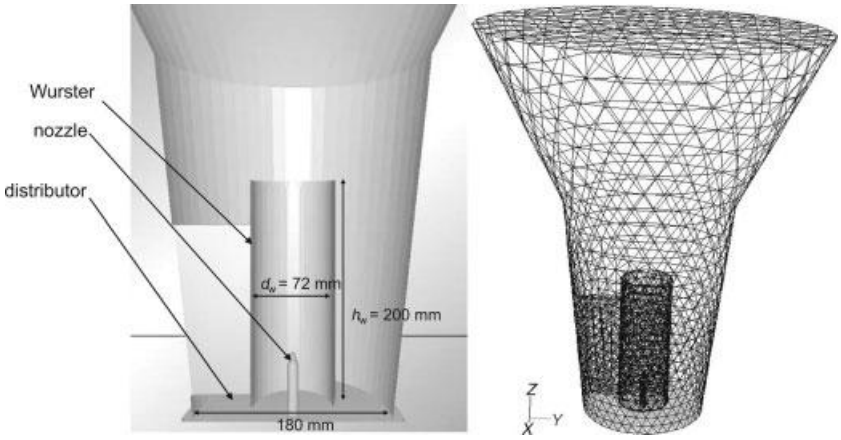

Fig. 7.49 Simplified Wurster geometry and mesh for fluid dynamics simulation (10 000 tetrahedral cells).

studies, the velocity of the nozzle air, the distribution of air between the Wurster and the surrounding annulus, and the height of the Wurster gap were varied. The spraying of droplets in the system has not been accounted for.

7.5.4.3 **Influence of the Spout Velocity**

The simulation results show that the velocity of the air injected via the nozzle has a strong influence on the fluid dynamics of the whole granulator.

In Fig. 7.50, snapshots of the particle positions and their velocities after the same process time are displayed. The granulator is cut vertically in the middle, and the central plane and the parts behind that plane are shown. The color indicates the particle velocity: blue particles move slowly ($v < 0.5\ \mathrm{m\,s^{-1}}$) and red particles are fast ($v > 1.5\ \mathrm{m\,s^{-1}}$). It can be seen from Fig. 7.50 that for all spout velocities the particles are concentrated at the center in the lower part of the Wurster tube. For high spout

Tab. 7.8 Operating variables.

Variable	unit	Case 1	Case 2	Case 3	Case 4	Case 5	Case 6
Particle mass	g	940	940	940	940	940	940
Fluidization air flow	$\mathrm{m^3\,h^{-1}}$	560	560	560	440	440	440
Atomizer air flow rate	$\mathrm{m^3\,h^{-1}}$	0.9	4.5	7.2	7.2	7.2	7.2
Velocity atomizer	$\mathrm{m\,s^{-1}}$	20	100	160	160	160	160
Velocity Wurster	multiples of u_{mf}	10	10	10	10	10	10
Velocity annulus	multiples of u_{mf}	5	5	5	3.8	3.8	3.8
Wurster gap distance	Multiples of d	5	5	5	5	10	15

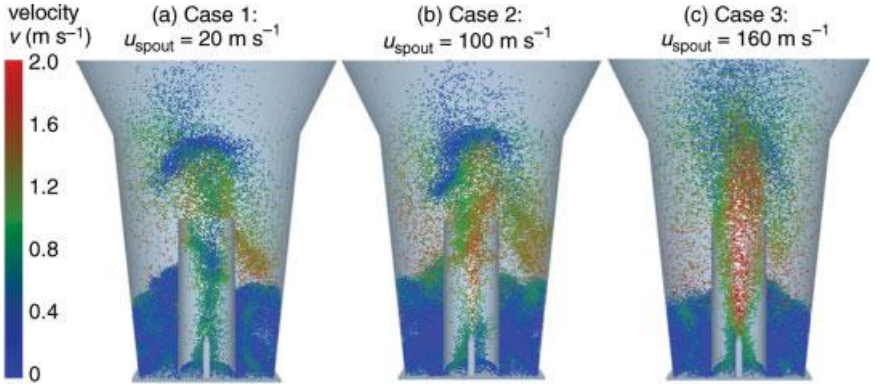

Fig. 7.50 Instantaneous particle positions and velocity distributions inside the Wurster tube at $t = 1.4$ s; colors indicate the velocity magnitude.

velocities (case 3) the particles are accelerated above the nozzle and transported upwards at high speed, which is indicated by red color. The fluidization regime is stable. At lower spout velocities (cases 1 and 2) the particle trajectories do not follow such a clear regular pattern. Slowly moving particles tend to block the upper end of the tube, inducing a slightly pulsating fluidization regime. Contrary to case 3, in cases 1 and 2 the particles already decelerate while they are transported to the upper end of the Wurster tube. The height of the particle fountain increases with higher spout velocity from 430 mm above the nozzle tip in case 1 to 490 mm in case 3.

To assess the radial distribution of particles in the granulator, horizontal slices were cut out of the simulated geometry. This was done at two different heights, as shown in Fig. 7.51. The thickness of each of the slices is 10 mm. The first slice is situated in the lower part of the Wurster tube, just around the tip of the injection nozzle. The second

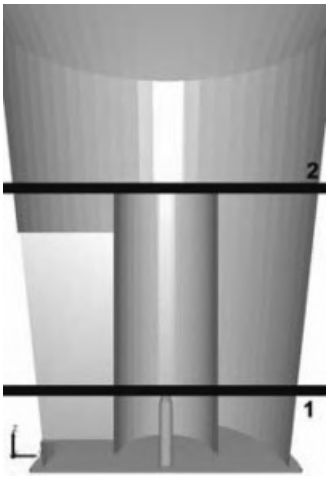

Fig. 7.51 Horizontal slices.

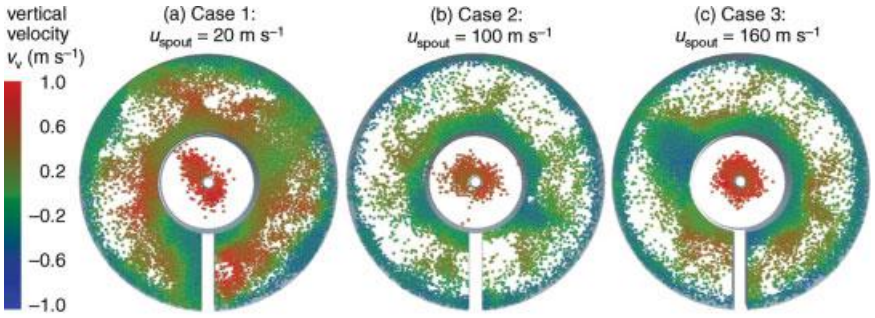

Fig. 7.52 Instantaneous horizontal position and vertical velocity component of the particles in slice 1 at time $t = 1.4$ s.

slice is at the upper border of the tube and allows visualization of the flow conditions of particles entering the expansion zone.

Figures 7.52 and 7.53 show instantaneous particle positions in the two slices, seen from the top. The colors indicate the vertical component of the particle velocity. Red particles are transported upwards, blue particles fall downwards. A comparison can be drawn between the first three case studies to evaluate the influence of the spout velocity on the horizontal distribution of the particles and their vertical velocity component.

It can be seen in Fig. 7.52 (slice 1) that the high spout velocity of case 3 tears particles towards the center of the Wurster tube. Particles coming out of the tube slip downwards along the apparatus walls of the annular part of the equipment. The low spout velocity of case 1 reduces the bed expansion in the annulus. A dense bed is observed, whereas high porosities due to rising bubbles occur in cases 2 and 3. In the middle of the ring the movement of the particles does not follow a clear pattern, as the flow in this zone is dominated by rising bubbles. High spout velocities seem to promote the formation of larger bubbles.

In slice 2, only a few particles are present (Fig. 7.53). Their movement is directed upwards inside the tube and downwards in the annulus in all three cases,

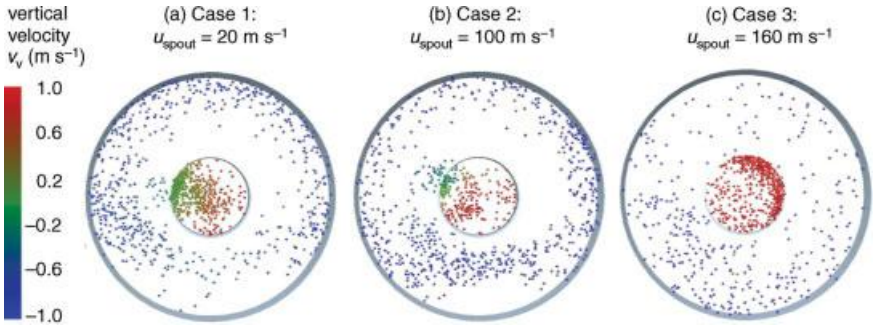

Fig. 7.53 Instantaneous horizontal position and vertical velocity component of the particles in slice 2 at time $t = 1.4$ s.

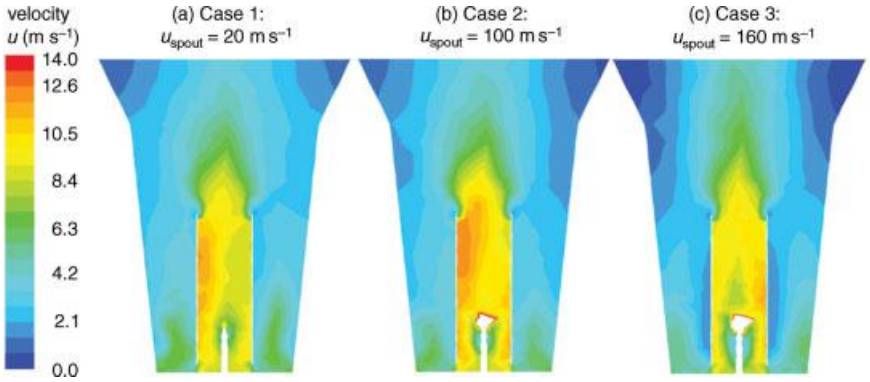

Fig. 7.54 Time-averaged fluid velocity distribution in the coater; colors indicate the velocity magnitude.

indicating that the circulating regime is intact over a wide fluidization range. Along the border of the Wurster tube, a deceleration of the particles can be observed in case 1, whereas at high spout velocity all particles move upwards at a velocity faster than $1\,m\,s^{-1}$ at this level (case 3). For low spout velocities as in case 1, some particles are moving downwards in the Wurster tube, which indicates unwanted back-mixing.

Figure 7.54 shows the time-averaged velocity field of the fluid for the three simulation cases. Jet velocities higher than $14\,m\,s^{-1}$ are cut off and displayed in white color in the graphic. It can be seen that the nozzle jet has a low injection depth. Even at the highest injection velocity of $160\,m\,s^{-1}$ at the nozzle tip (case 3), the fluid velocity decays to $14\,m\,s^{-1}$ within less than 30 mm from the tip. The momentum introduced by the jet is immediately transferred to the particles in a relatively small zone above the nozzle tip. In case 1, the penetration depth of the jet injected at $20\,m\,s^{-1}$ is almost invisible. In contrast to the particle velocity distribution, the gas flow field inside the Wurster tube is hardly influenced by the jet velocity. This is because even in case 3 less than 2% of the total gas flow is injected via the nozzle. More than 98% of the gas enters the system via the distributor plate at the bottom of the granulator. In Fig. 7.55, snapshots of the volume fraction of the particle phase are shown. High particle concentrations are observed along the apparatus walls, where the particles slip downwards, and at the center of the Wurster tube around the nozzle shaft.

7.5.4.4 Influence of the Wurster Gap Distance

The gap distance between the distributor plate and the Wurster tube is a parameter that strongly influences the fluid and particle dynamics inside the granulator. Gap heights of 10, 20 and 30 mm were compared.

It can be seen in Fig. 7.56 that a larger gap below the Wurster tube increases the number of particles that are transported into the tube. In case 4, particles are only present at the center of the lower half of the tube. All particles rise at a velocity above $1\,m\,s^{-1}$ which is indicated by green and red color. In contrast, in cases 5 and 6

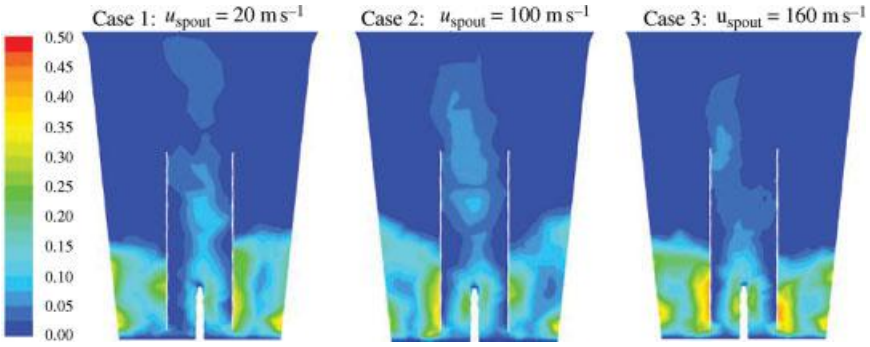

Fig. 7.55 Instantaneous particle volume fraction in the Wurster coater at $t = 1.4$ s.

particles can be found spread over the whole diameter of the Wurster tube. Near the wall of the tube they move at low velocity, indicated by blue color.

For the functionality of a Wurster coater it is important that the particles are coated homogeneously. This can be achieved by a regular fluidization regime with a well defined circulating movement of the particles. The thickness of the coating layer on a particle's surface is controlled by the residence time of the particle inside the spray cone at the nozzle tip. With this perspective, the regime of case 3 seems optimal, as all particles move on similar trajectories and at similar velocity inside the Wurster tube. This will yield a narrow residence time distribution of the particles in the spray zone. Contrary to that, a larger Wurster gap distance, as used in cases 5 and 6, induces a broad residence time distribution of the particles in the Wurster tube and, hence, an irregular coating layer thickness.

Summarizing, it can be stated that a homogenous velocity distribution of the particles inside the Wurster tube was achieved at a high spout velocity of $160\ m\,s^{-1}$ and at low gap distances between the tube and distributor of 5 times the particle

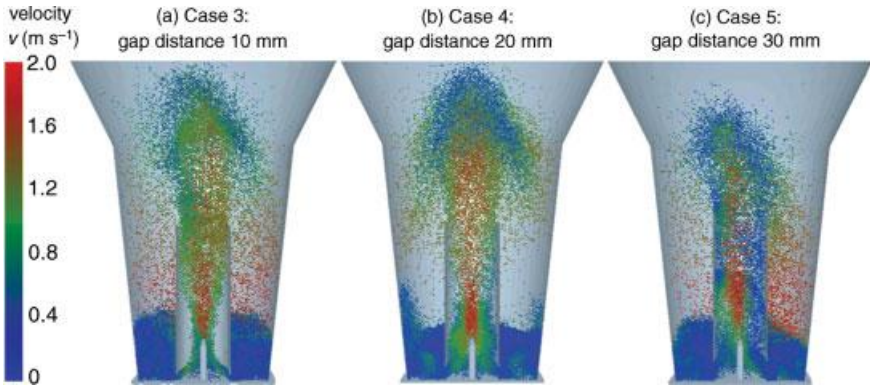

Fig. 7.56 Instantaneous position and velocity distribution of the particles in the Wurster zone for different gap distances at time $t = 1.4$ s.

diameter. This set-up will provide a homogeneous coating quality, as the residence time of the particles inside the spray zone is similar for all particles and relatively short. Internal recirculation in the tube and back-mixing of particles falling down from the expansion zone is avoided.

The results show that the DPM method offers great potential to describe fluidized bed processes on the scale of individual particles using only physically based input parameters. Especially, the exact description of particle–particle interactions using a sophisticated contact model is a strong feature of this method. However, limitations due to the high numerical effort are still important. Process scale granulators cannot be described within a reasonable simulation time.

Therefore, based on the example of fluidized bed granulation, the DPM method should be seen as a tool relevant for obtaining on the micro-scale kinetic rate constants which define the dynamics of the process. For example, the wetting kinetics could be described by approximating the particle moisture content with the residence time of individual particles in the spray zone. Together with this information, results on the collision frequency and collision velocity distributions can enable the definition of physically based aggregation rate terms. Instead of using an empirical kernel, such DPM-based growth kinetics could be implemented in a population balance model to enforce the predictive description of granulation or agglomeration processes on the macro-scale.

7.6
Neural Networks, Encapsulation

Encapsulation of liquids in granular products is an important process used mainly in the food and feed industry to protect valuable ingredients such as flavors, aromatic oils or fragrances against ambient oxygen, to improve the storage stability, and to reduce contamination risks. As discussed in Chapter 6, encapsulation can be conducted by spray drying of an emulsion, where the active ingredient to be retained is in the droplet phase. The same goal can also be achieved by spray fluidized bed granulation, with the additional advantage of a relatively coarse-grained, easy-to-handle product. In the simplest case, the sprayed emulsion is, again, an oil-in-water system, where the water-insoluble active ingredient is homogeneously suspended in an aqueous matrix solution. Spreading of the spray on the surface of the fluidized particles and drying lead to layered growth, so that at the end of the process the remaining solid material (the matrix) contains the dispersed active ingredient. A typical process development task is to assess the influence of operating conditions and formulation parameters on product quality. Since this can hardly be done on first principles, experiments are necessary. However, the number of such experiments should be kept as low as possible, and their results should be organized in a way that enables reliable interpolation. This can be achieved by the use of artificial neural networks, as will be outlined in the following with the help of an example.

This specific example refers to the encapsulation of aromatic oils with different volatility (namely orange, mint or pergamot oil) by spray fluidized bed granulation.

Tab. 7.9 Parameters of influence for spray fluidized bed encapsulation of aromatic oils.

Parameter	Unit	Min.	Median	Max.
Process conditions				
Product temperature	°C	41.0	47.5	82.0
Spray rate	$g\,min^{-1}$	16.0	34.5	49.0
Residence time	min	7.5	19.4	47.6
Formulation of emulsion				
Active ingredient	—	orange, mint, bergamot oil		
Oil	%	10.0	19.0	20.5
Water	%	47.7	48.0	50.0
Maltodextrin type 1	%	0.0	29.0	40.7
Maltodextrin type 2	%	0.0	1.0	29.0
Starch type 1	%	0.0	8.0	30.0
Starch type 2	%	0.0	3.5	40.0
Film forming agent	%	0.0	2.8	3.0
Emulsifier	%	0.0	0.1	3.0

The considered parameters of influence are summarized in Tab. 7.9. They are in total 12, including three operating parameters (product temperature in the process chamber, emulsion spray rate, and average residence time of the solids) and nine quantities that describe possible variations of the emulsion recipe, namely the kind of active ingredient (aromatic oil) considered, the mass fraction of this active ingredient and of water in the spray liquid as well as the kind and mass fraction of matrix materials (two maltodextrins and two starches) and additives (film former, emulsifier) used. Ranges of the variation of these parameters in the experiments are also given in Tab. 7.9. All trials (36 individual experiments) were conducted in a continuously operated, lab-scale ProCell unit (see Section 7.5.1 for a description of this special type of spouted bed equipment) under steady-state conditions. The inlet air temperature was adjusted depending on the target product temperature and the actual spray rate.

Samples taken from the continuous product discharge were subject to manifold physical and chemical analysis, including the determination of particle size distribution, untapped bulk density, water content (by infrared), amount of active ingredient (by water steam extraction), and the observation of sphericity, surface morphology and internal structure by scanning electron microscopy (Fig. 7.57). However, the main focus was on two quantities:

- yield of active ingredient in the product (encapsulation efficiency or retention efficiency), which is the ratio of encapsulated to sprayed mass of active ingredient, and
- average particle size.

This focus results from the desire to find liquid formulations and process conditions that give both a high yield of active ingredient in the product and particle sizes in the right range.

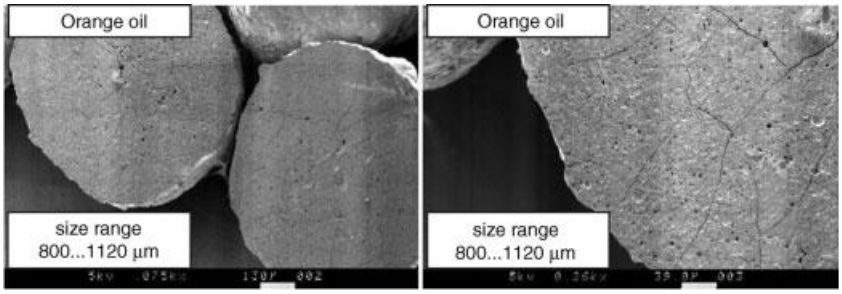

Fig. 7.57 Cross-sections of granules containing encapsulated orange oil.

To correlate the mentioned target quantities with the various parameters of influence the concept of artificial neural networks (for more information on mathematical background and applications see, for example Bärmann and Biegler-König (1992), Braspenning *et al*. (1995)) has been applied. Specifically, a simple three-layer feed-forward network was established using the commercial software "NN-tool 2000" (Bärmann Software, Germany). The scheme of such a network is shown in Fig. 7.58. The mentioned 12 parameters that describe process conditions and the emulsion recipe constitute the input layer, whereas the target indices of product and process quality are placed in the output layer. Hidden layer and connectivities are obtained by training the network with the help of the experimental data, including a cross-validation procedure. The trained network can first be applied to predict the used experimental results. Comparison of predicted values with this data in, for example, scatter plots is a measure of the accuracy with which the method can reproduce the available experimental information. This accuracy was found to be satisfactory for both target parameters – yield and average particle size.

After training and the described control, the artificial neural network can be used to

- evaluate the influence of process and product parameters on product properties,
- optimize yield and formulation costs.

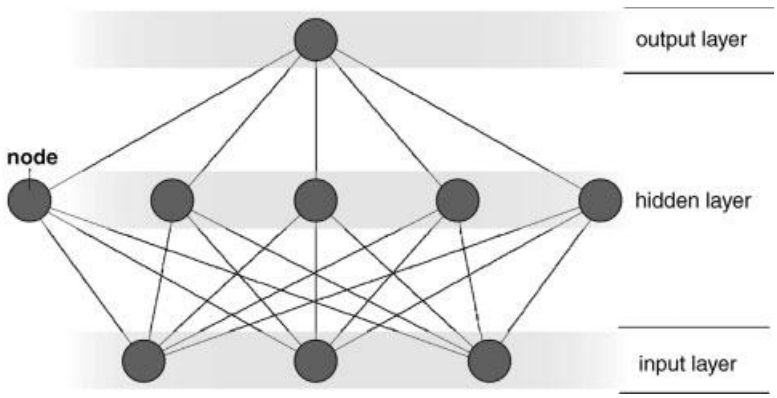

Fig. 7.58 Scheme of three-layer artificial neural network.

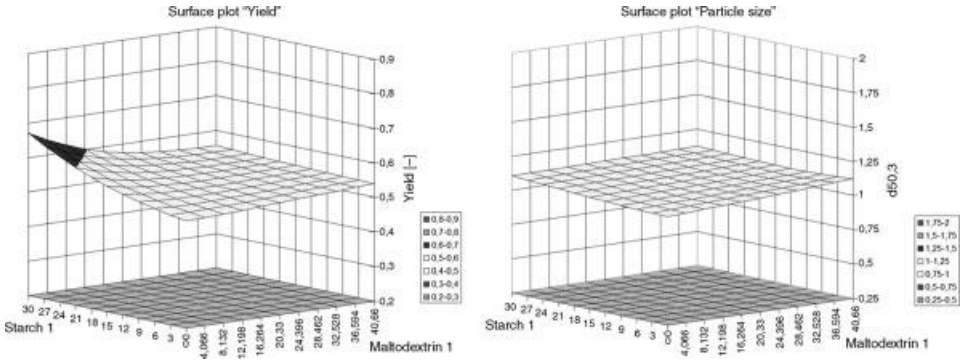

Fig. 7.59 Influence of maltodextrin type 1 and starch type 1 on yield and particle size for orange oil.

Selected results of the parametric study are illustrated in Figs. 7.59–7.61. The surface response plots refer to the influence that changes in the matrix composition (mixtures of maltodextrin type 1 and starch type 1 with different mass fractions of these components) have on the yield and the average particle diameter for the three investigated oils. All other input parameters were set to their median values according to Tab. 7.9. The diagrams show that different encapsulation efficiencies, and also different particle sizes, are obtained for each of the three aromatic oils, which is expected because of differences in the chemical structure and properties of the oils. For instance, the yield of mint (Fig. 7.60) was significantly higher than those of orange (Fig. 7.59) and pergamot (Fig. 7.61). The yield of mint also shows the highest sensitivity to variations in the composition of matrix material in the emulsion.

Concerning the influence of other parameters, the yield was found to increase with increasing spray rate, decreasing product temperature and decreasing residence time. Bigger particles were produced at high spray rates and low temperatures, with a

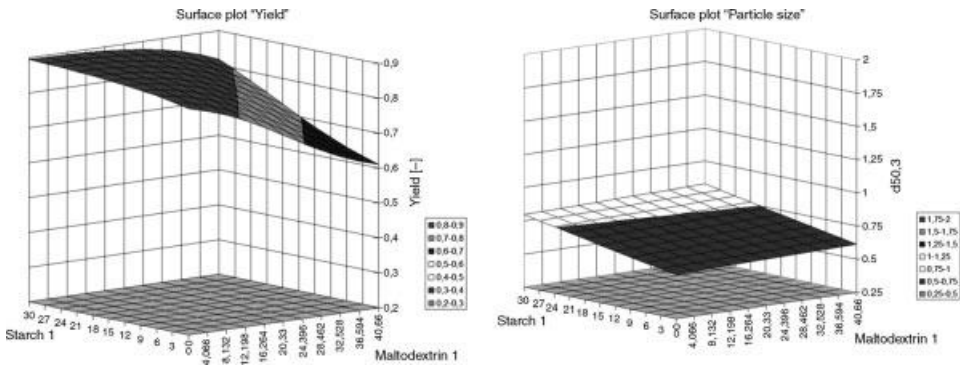

Fig. 7.60 Influence of maltodextrin type 1 and starch type 1 on yield and particle size for mint oil.

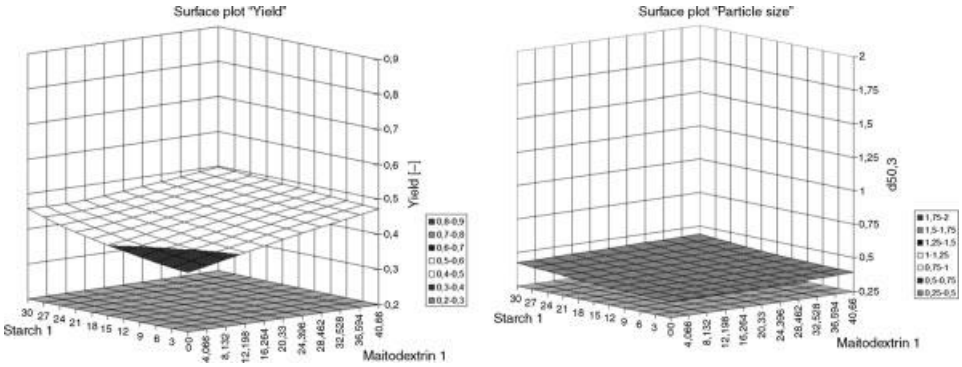

Fig. 7.61 Influence of maltodextrin type 1 and starch type 1 on yield and particle size for pergamot oil.

less clear trend with respect to residence time. All this depends on the choice of active ingredient and the recipe in a complex way that is difficult to express verbally, pictorially or by equations, but can be captured by the artificial neural network.

Consequently, the artificial neural network can be used to optimize the encapsulation process. This capability is demonstrated in Figs. 7.62 and 7.63. Figure 7.62 shows the dependence of retention yield for orange oil on spray rate and residence time. This diagram was calculated for a simplified composition of emulsion containing only maltodextrin type 1, starch type 1, orange oil and water. The mass fractions of water and oil were kept constant at 50% and 20%, respectively. For the case shown in

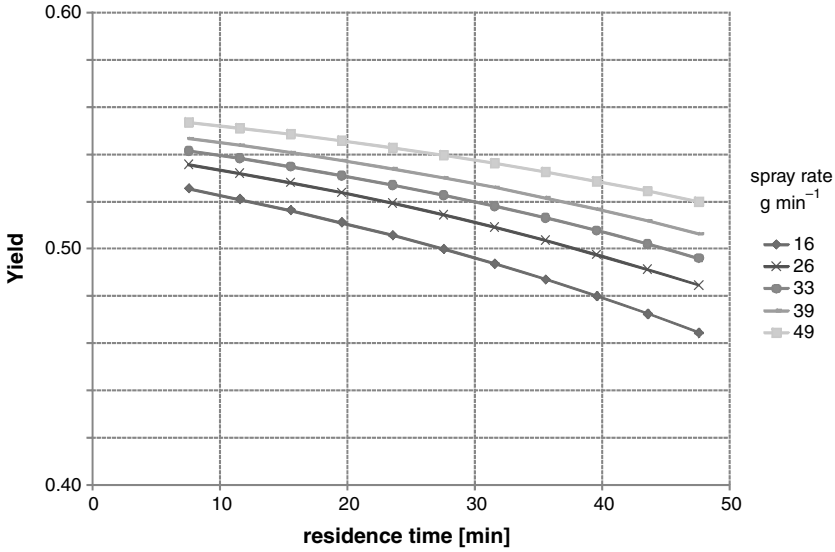

Fig. 7.62 Low yields of encapsulated orange oil for parameter set no. 1.

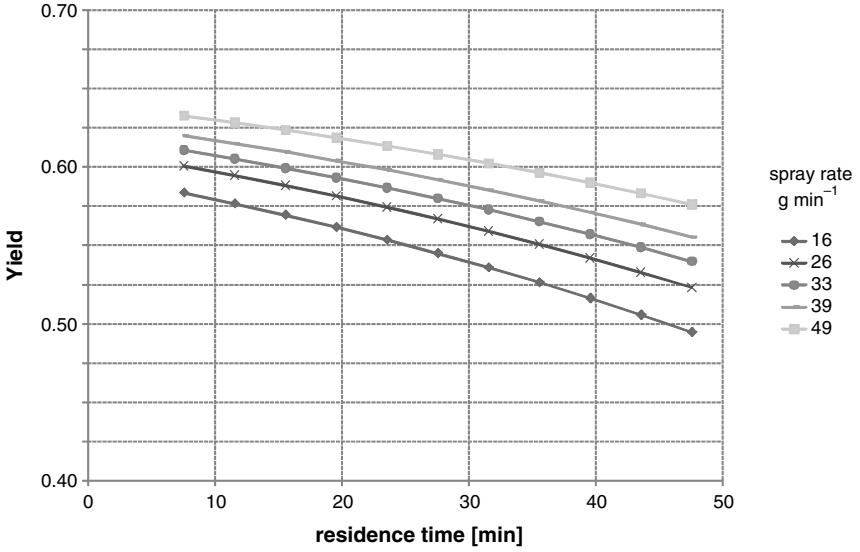

Fig. 7.63 Significantly improved yields of encapsulated orange oil for parameter set no. 2.

Fig. 7.62 the amount of maltodextrin was higher than the amount of starch (parameter set no. 1). The retention of oil according to Fig. 7.62 is so low that an industrial application would be too expensive due to high raw material losses. However, higher yields of oil can be attained by improving the formulation, guided by the artificial neural network. Specifically, the amount of maltodextrin can be decreased and the amount of starch increased. This leads to the results illustrated in Fig. 7.63 (parameter set no. 2). The yield of active ingredient is now significantly higher than for the initial set of parameters. This is because matrices based mainly on starch have, after drying, a lower porosity than matrices based mainly on maltodextrin. The process depicted in Fig. 7.63 would be industrially viable, though for the price of a more expensive raw material.

As both Figs. 7.62 and 7.63 show, low residence times are an advantage when volatile substances have to be encapsulated into a granular structure. Therefore, the ProCell apparatus used in the described investigation was a good choice. As already pointed out in Section 7.5.1, this apparatus allows one to spray on a relatively low bed mass, keeping the residence time of the solids short. Simultaneously, high shear forces in the spout support uniform film formation and minimize the tendency to agglomeration. The use of a conventional fluidized bed for the same application would mean a higher hold-up, longer residence time and, hence, more loss of active ingredient.

In general, it should be borne in mind that artificial neural networks do not consider the physics of processes in any way; they simply reflect the experimental information used for their training. However, if properly applied, they can significantly support the design of processes and formulations.

7.7
Stochastic Discrete Modeling of Agglomeration

7.7.1
General Principles

Stochastic, so-called Monte Carlo (MC), methods use probabilistic tools to simulate the evolution of a finite sample of the particle population during, for example, spray fluidized bed agglomeration. They refrain from a computation of the flow field, so that parameters related to this flow, such as the frequency of collisions between particles, must be treated as known input quantities. In the case of large differences in the flow field between different regions within the apparatus, different particle samples must be considered by combination of a number of interacting MC simulations that run in parallel. Hence, stochastic methods create less information than the DPM (compare with Section 7.5.4), but they are easier to implement and much faster, so that they can be applied over the entire duration of real processes. On the other hand, MC simulations are still discrete. This means that all micro-scale mechanisms with an influence on the overall process behavior – wetting of particles by droplets, the removal of such droplets from the surface of particles by drying or liquid penetration, particle coalescence or agglomerate breakage – can be captured and described on a physical basis. Distributed properties such as the particle size can be continuously monitored in this way without having to – more or less arbitrarily – choose coalescence or breakage kernels. Consequently, MC simulations provide much more profound insight into particle formulation processes than macroscopic population balance equations (PBE), for the price of more computational effort. In this sense, MC is placed somewhere between DPM and PBE. The ability of MC to provide stochastic numerical solutions of the PBE has been discussed by Ramkrishna (1981).

Monte Carlo methods are classified into two main groups according to the treatment of the time step: time driven and event driven methods. In the time driven approach, first a time step is specified and then all the possible events within this time step are implemented (Haibo *et al.*, 2005). In the event-driven approach, an event is designed to happen and then time runs by a previously designated amount (Shah *et al.*, 1977). The MC methods can be further distinguished according to the kind of particle number regulation in methods with continuous or periodical regulation. Continuous regulation means that once a particle appears or disappears from the simulation box, another is randomly copied or erased to maintain the number of particles N_p constant and equal to a value $N_{p,0}$ specified at the beginning of the simulation. Under periodic regulation, once the total number of particles reaches $^1/_2 N_{p,0}$, the number of particles is doubled by taking an additional identical control volume. The choice of the method should be based on the mechanism that governs during the process. It has been found that the event-driven method with periodical particle regulation (constant volume Monte Carlo method, CVMC) is more suitable for coalescence dominated processes such as agglomeration (Zhao *et al.*, 2007). The connection between CVMC and the real particulate system arises from the event-driven nature of the method.

In the following, an implementation of the CVMC method for spray fluidized bed agglomeration and respective results will be discussed based on work by Terrazas (Terrazas-Velarde *et al.*, 2009, 2011); Terrazas-Velarde, 2010). In this work an "event" is defined as a collision among the particles within the fluidized bed. The number of events k is given at the beginning of the simulation and the time step is calculated on the basis of collision frequency.

7.7.2 Computational Method

As already pointed out, the frequency of collisions among particles in the fluidized bed, f_{coll}, must be known in order to apply the MC method. To this purpose the empirical equation

$$f_{\mathrm{coll}} = F_{\mathrm{coll}}\left[1-\left(\frac{1-\varepsilon}{1-\varepsilon_{\mathrm{mf}}}\right)\right]\left(\frac{1-\varepsilon}{1-\varepsilon_{\mathrm{mf}}}\right)^{2} u_0 \tag{7.48}$$

proposed by Buffière and Moletta (2000), was used. This equation provides reasonable trends regarding the influence of fluidization velocity u_0 and expanded bed porosity ε, whereby $\varepsilon_{\mathrm{mf}}$ is the porosity at minimal fluidization. For a given material, the collision frequency pre-factor F_{coll} was fitted to the results of one spray fluidized bed agglomeration experiment conducted under mild thermal conditions, as will be discussed later.

With known collision frequency, the length of the time step of the MC method – distance in time between one and the next event – can be calculated to be

$$t_{\mathrm{step}} = \frac{1}{f_{\mathrm{coll}}} \tag{7.49}$$

so that the real time elapsed after k events sums to

$$t_{\mathrm{real}} = \sum_{k=1}^{k} t_{\mathrm{step}} \tag{7.50}$$

Continuous droplet addition in the model is accomplished by calculating the number of droplets per primary particle per second that are introduced to the real system

$$\gamma = \frac{\dot{M}_{\mathrm{l}}}{M_{\mathrm{bed}}}\frac{\varrho_{\mathrm{p,0}}}{\varrho_{\mathrm{l}}}\left(\frac{d_0}{d_{\mathrm{d}}}\right)^{3} \tag{7.51}$$

Here, $\dot{M}_{\mathrm{l}}$ is the mass flow rate of sprayed liquid, ϱ_{l} the liquid density, d_{d} the droplet diameter and M_{bed} the mass of the bed; $\varrho_{\mathrm{p,0}}$ and d_0 are primary particle density and diameter, respectively. Notice that the droplet addition rate γ is equal for both the real process and the simulation. From the value of γ and the initial number of particles (primary particles) within the simulation box $N_{\mathrm{p,0}}$ the droplet addition

time t_{ad}, which is the time necessary to add one single droplet to the simulation box, is calculated to be

$$t_{ad} = \frac{1}{2^N \gamma N_{p,0}} \tag{7.52}$$

where N is the number of doublings that the simulation system undergoes. The particles to be wetted are chosen randomly among the population. Once a droplet is ready to deposit on a particle it is assumed to take the shape of a spherical cap with volume V_{cap}, base radius a, and height h that fulfills the relationships

$$a = \left(\frac{3V_{cap}}{\pi} \frac{\sin^3 \theta}{2 - 3\cos\theta + \cos^3\theta} \right)^{1/3} \tag{7.53}$$

$$h = a \frac{1 - \cos\theta}{\sin\theta} \tag{7.54}$$

where θ is the solid–liquid equilibrium contact angle.

Immediately after droplet capture and particle wetting, the deposited droplet is available to potentially form a liquid bridge and produce coalescence with another particle or agglomerate. However, the deposited droplet is going to age until a successful coalescence has taken place due to two mechanisms, namely drying and penetration ("imbibition"). Drying is necessary for solid particle formation and takes place anyway, on compact or on porous particles, whereas imbibition by capillary suction takes place only on a porous substrate. Consequently, droplets age only by drying on compact particles, and by a combination of drying and imbibition on a porous substrate.

The drying mechanism reduces the height and increases the viscosity of deposited droplets that consist of a volatile solvent (usually water) and a binder. As the agglomeration process proceeds, existing droplets which have not experienced a successful coalescence are becoming older until they solidify. The kinetics of the height reduction of droplets deposited on compact particles by drying can be estimated easily by neglecting the influence of the binder on the drying rate, and assuming that the contact angle remains constant during the decrease in height and radius (Erbil *et al.*, 2002). In this way, the following equation is obtained (Terrazas-Velarde *et al.*, 2011):

$$h_{dry} = h_0 - \frac{2}{3} \frac{\varrho_g}{\varrho_w} \frac{\tilde{M}_w}{\tilde{M}_g} \frac{\beta}{1 - \cos\theta} \left(\frac{P_v^*}{P} - \tilde{y}_v \right) \left[\frac{1}{1 - \cos\theta} - \frac{1}{3} \right]^{-1} t \tag{7.55}$$

Here, P_v^* is the saturation pressure of the solvent (water) at the surface of the particles, $\tilde{y}_v$ is the respective molar fraction in the gas phase, and β is the gas-side mass transfer coefficient.

In analogous manner (Terrazas-Velarde, 2010), the penetration of solvent into the pores of the primary particle can be described by the relationship

$$h_{\mathrm{imb}} = h_0 - \frac{2}{3}\varepsilon_{\mathrm{p}}\left(\frac{\sin\theta}{1-\cos\theta}\right)^2\left[\frac{1}{1-\cos\theta}-\frac{1}{3}\right]^{-1}\sqrt{\frac{\gamma\cos\theta\, r_{\mathrm{pore}}}{8\,\mu_{\mathrm{l}}}}\,t^{1/2} \tag{7.56}$$

Equation 7.55 can be applied with reasonable estimates of gas-side state variables in a fluidized bed and combined with Eq. 7.56 to capture the simultaneous influence of drying and imbibition. Notice that a drying time and a wetting time can be derived from Eqs. 7.55 and 7.56, respectively. These time constants have a similar meaning to that of the time constants used in Section 7.4.2, but they are more specific, because they do not refer to the whole particle, but to one deposited droplet. Another difference to Section 7.4.2 is that drying and imbibition are not antagonistic in the case of agglomeration: both contribute to a decrease in the availability of surface liquid for coalescence, so that both tend to decrease the experimentally observable agglomeration rate.

Successful coalescence presupposes the collision of two particles at, at least, one wet – or still wet – spot. Additionally, the liquid must be able to dissipate, by viscous forces, the kinetic energy of the collision – otherwise the particles will not stick together, but rebound. This second condition can be quantified by application of the so-called Stokes criterion, which was derived by Ennis *et al.* (1991). According to this criterion a collision is assumed to be successful in the sense of agglomeration when the inequality $St_{\mathrm{coal}} < St_{\mathrm{coal}}^{*}$ is fulfilled, with

$$St_{\mathrm{coal}} = \frac{2\,M\,u_{\mathrm{coll}}}{3\pi\,\mu_{\mathrm{l}}\,d^2} \tag{7.57}$$

$$St_{\mathrm{coal}}^{*} = \left(1+\frac{1}{e}\right)\ln\left(\frac{h}{h_{\mathrm{a}}}\right) \tag{7.58}$$

In the framework of the Stokes criterion the influence of several process parameters can be quantified. A reduction in the coalescence Stokes number St_{coal} and, thus, a higher probability of agglomeration, is achieved by smaller collision velocities u_{coll}, which depend directly on the fluidization gas velocity. Higher liquid viscosities μ_{l} – either by more binder in the sprayed liquid or by droplet aging due to drying – have a similar effect. An increase in the thickness h of the liquid layer that can be attained by using larger droplets will shift the agglomeration limit towards bigger particles (larger value of the critical Stokes number St_{coal}^{*}). In contrast, smaller droplets inhibit agglomeration and favor layering granulation or coating. Smaller droplets can be realized by the use of appropriate nozzles and spraying systems, but they can also result from strong drying and fast imbibition in the process. Additional quantities with an influence on the Stokes criterion are the height of asperities on the surface of particles, h_{a}, and the restitution coefficient, e. Averages considering both colliding particles are used for the mass, M, and the diameter, d, in Eq. 7.57.

The stochastic approach treats the size enlargement process as an increase in the number of primary particles per agglomerate. In order to be able to compare the model results with a real process, this number is correlated with the agglomerate diameter by assuming a constant agglomerate porosity of 60%. The structure of the primary particles within the agglomerate is based on a concept of fractional

surface coverage and maximum coordination number $K_{max} = 6$. It should be noted, that successful coalescence can block some droplets according to this concept, making them inaccessible to further collision partners. Such droplets cannot produce a liquid bridge, so that they will age to ineffective solidification by drying. In this way, the steric hindrance of some droplets that has already been mentioned in Section 7.3.3 is taken into account in the model. Further details are given in Terrazas-Velarde (2010).

7.7.3 Results

To evaluate the performance of the model, batch experiments were carried out in a lab-scale fluidized bed equipped with a two-fluid nozzle in top-spray configuration. The liquid solution was HPMC in water. Compact glass beads and porous alumina (γ-Al_2O_3) particles were used as the solids, with an initial average diameter d_0 (primary particle diameter) equal to 0.4 and 0.36 mm, respectively. A single selected experiment with glass and a single experiment with alumina, both conducted at mild thermal conditions, were used to adjust the collision frequency pre-factor F_{coll}. In this way, the value of $F_{coll} = 10\,m^{-1}$ ($f_{coll} = 1.6\,s^{-1}$) was obtained for glass, and $F_{coll} = 45\,m^{-1}$ ($f_{coll} = 4.1\,s^{-1}$) for alumina. Once this parameter was fitted, it was used without further change for comparison with all other data gained with the respective material. A deeper discussion on the effect of the number of collisions on model response, more details about equipment and material properties, and a full documentation of the experimental results can be found in Terrazas-Velarde (2010). Here, just a few comparisons with measured data are presented to show that the model can reliably describe the influence of process parameters.

7.7.3.1 Effect of Liquid Flow Rate and Viscosity

Figure 7.64 shows the effect of liquid addition rate, $\dot{M}_l$ on the agglomeration kinetics of glass particles, expressed by the ratio of current to initial particle diameter during the process. As can be seen, agglomeration is faster at high spraying rates. A higher liquid flow rate means more liquid droplets introduced to the system, wetter particle surfaces, more wet collisions and, thus, an increase in agglomeration rate. The number of droplets introduced to the system is of essential importance for the rate of the process.

Regarding the properties of the sprayed solution, it is observed in Fig. 7.65 that faster agglomeration is obtained as the binder mass fraction and, therefore, the viscosity of the liquid increases. This is due to the higher ability of deposited liquid layers to dissipate the kinetic energy of collisions, so that the particles involved tend to stick together rather than to rebound.

7.7.3.2 Thermal Effects

An important advantage of the micro-level approach is that it enables one to analyze mechanisms that cannot be isolated experimentally. As an example, Fig. 7.66 shows

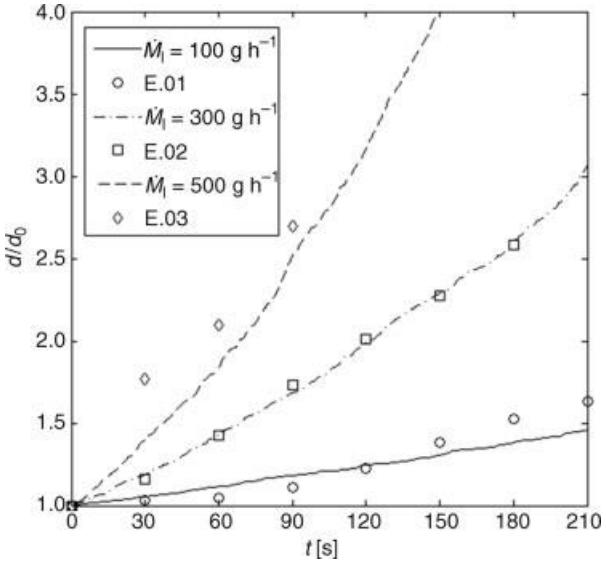

Fig. 7.64 Effect of binder addition rate on the growth of glass particles by agglomeration; (Run numbers refer in this and in the following figures to the documentation of data according to Terrazas-Velarde (2010)).

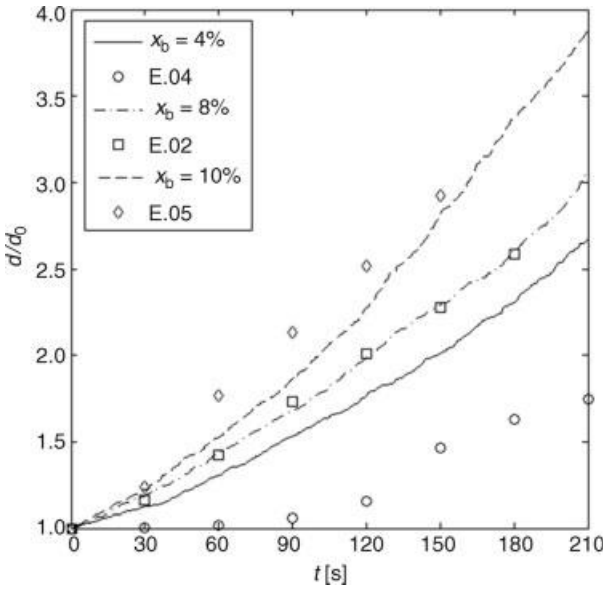

Fig. 7.65 Effect of binder mass fraction in the sprayed droplets (droplet viscosity) on the agglomeration rate of glass particles.

model results computed at different binder mass fractions with and without implementation of the drying mechanism. Two completely opposing tendencies can be recognized in this plot: Drying is predicted to accelerate the agglomeration in the case of low-viscosity binders, but to inhibit the process significantly when the liquid viscosity is relatively high.

When the drying mechanism is not included (denoted by "ND" on the plot) and the liquid viscosity is low ($x_b = 0.02$), the model predicts a total absence of agglomeration (the particle diameter remains constant at its initial value). This is because the liquid deposited on the particles is not able to absorb the kinetic energy of collisions. In reality, granulation by layering would take place under such conditions – with a growth rate which would be much smaller than in the case of agglomeration. However, when the droplets are allowed to dry, the agglomeration process is switched on, under otherwise exactly the same conditions. This is because the viscosity of the liquid is increased by drying to an extent that is sufficient for dissipation of the collision energy and, thus, for coalescence.

At high binder mass fractions in the spray ($x_b = 0.08$ and 0.10), the initial viscosity of the liquid is already large enough for the dissipation of collision energy, so that a further increase in viscosity during drying does not really matter. However, drying also means a reduction in the droplet height and availability – which matters, overriding the influence of the viscosity increase, and reducing the agglomeration rate significantly in these cases.

The results of Fig. 7.66 point out the complex and intimate coupling between drying and agglomeration in spray fluidized beds. The fact that the droplets dry during the process does not necessarily mean less agglomeration, as drying can also be favorable in the case of diluted binder solutions. In practice, the intensity of drying can be manipulated mainly by changing the gas inlet temperature. The effect of gas inlet temperature on the agglomeration behavior is illustrated in Fig. 7.67. The plot shows a decrease in agglomeration rate with increasing gas inlet temperature, which means that the already discussed effect of reduced droplet height and availability in the system prevails for the depicted data.

In total, the application of the MC model enabled one to explain and quantitatively describe the influence of thermal effects on wet agglomeration (Terrazas-Velarde *et al.*, 2011) in a never before achieved way, which is not possible by application of conventional PBE approaches. Drying is the key to this explanation – in combination with the access to micro-scale physical interactions that the model provides.

7.7.3.3 **Effect of Particle Porosity**

The features of the model also allow the simulation of solids which only differ in their porous or non-porous character by accounting, or not, for imbibition (Eq. 7.56). Unfortunately, porous and compact solids with otherwise exactly the same properties (e.g., particle density) do not exist in reality. Therefore, the experimental investigation has stayed with glass as the compact material and alumina as the porous material. However, two fictitious substances, namely porous glass and compact alumina, both with otherwise the same properties as their real counterparts, were added to model evaluation.

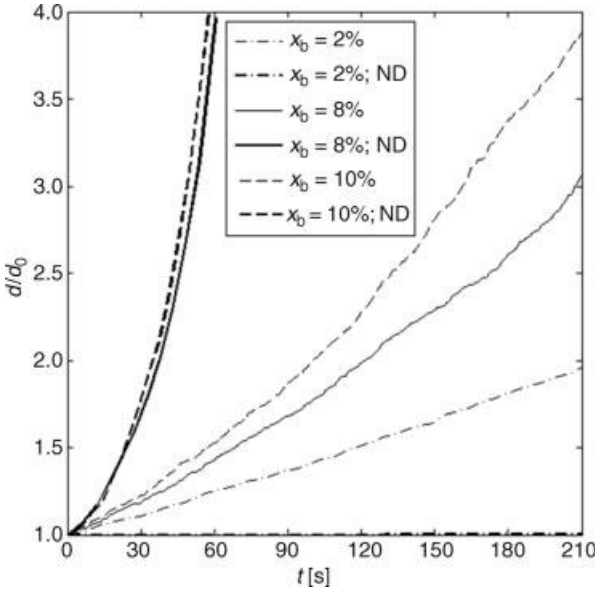

Fig. 7.66 Drying of deposited droplets can trigger agglomeration at low binder mass fractions, but decreases the agglomeration rate when enough binder is contained in the sprayed solution; (simulations conducted without implementation of the drying mechanism are denoted by "ND").

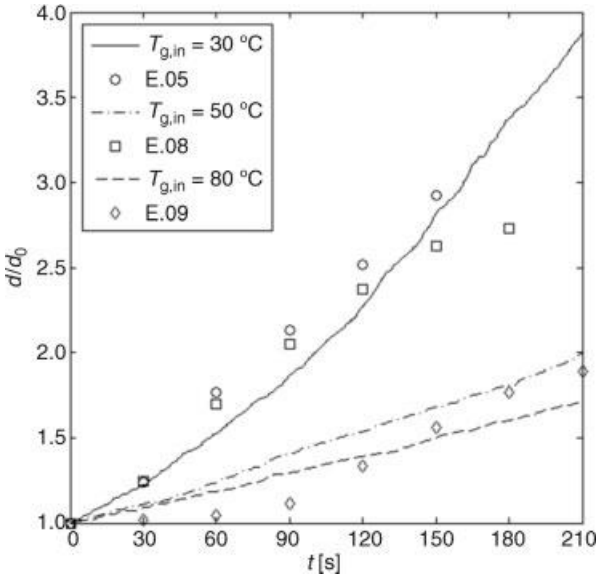

Fig. 7.67 Influence of gas inlet temperature on the agglomeration of glass particles.

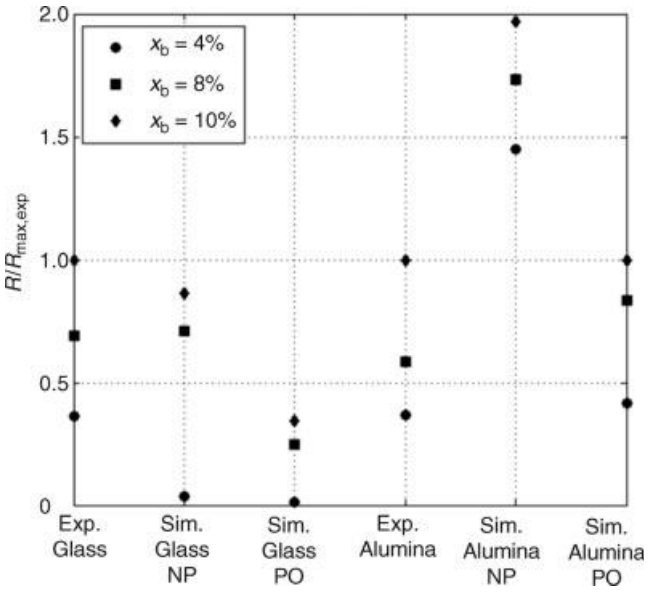

Fig. 7.68 Effect of imbibition at different binder mass fractions; comparison between simulations and experimentally obtained agglomeration rates for real and fictitious materials (NP: non-porous, PO: porous).

The results are summarized in Fig. 7.68. The ordinate of this plot shows average agglomeration rates R, made dimensionless by reference to the maximal agglomeration rate measured for the considered material. The first data column of the plot refers to experiments conducted at different binder mass fractions with glass. The highest agglomeration rate was measured at $x_b = 0.10$, so that the respective value of $R/R_{max,exp}$ is, by definition, unity. On decreasing the binder mass fraction the agglomeration rate decreases, for the previously discussed reasons, so that the two other points for real glass lie lower. The second column refers to simulations for real glass particles. Comparison with the first column shows that the model does not predict the experimental data perfectly, but reflects the right trend and performs reasonably well. The third column makes the glass particles porous in the simulation. Here we see a dramatic decrease in agglomeration rates, because droplets do not get lost only by drying, but also by imbibition in the porous substrate. The fourth column summarizes the results of experiments with γ-Al_2O_3. Concerning the influence of binder mass fraction, these experiments show the same dependence as the experiments with glass. The alumina particles were rendered compact in the simulations of the fifth column. This manipulation increases the agglomeration rates to approximately twice the measured values, because droplets are no longer lost by capillary suction. Finally, comparison of the sixth with the fourth column shows the relatively good agreement between model and experiment for real alumina.

The conclusion of the study is that the imbibition mechanism may cause high droplet losses that reduce the agglomeration rate significantly, so that this

mechanism needs to be accounted for – in combination with drying – in the model when dealing with porous substrates.

7.8 Summary and Outlook

Spray fluidized beds offer unique opportunities to formulate particles with specific properties by agglomeration, granulation or coating. Such opportunities stem from the huge variety of changes in material properties, process parameters and apparatus design with an influence on product structure and quality. The same variety is a challenge, because it makes conventional engineering approaches (for instance the use of correlations of dimensionless numbers) virtually impossible. Several scales that range from the particle system (fluidized bed, apparatus) over the single particle, the porous interior of the particle to the molecular level (e.g., around particle contacts) are present and potentially significant. This requires the use of various computational methods – some of them continuous, such as population balance equations, and some discrete, such as discrete particle modeling and Monte Carlo. None of these methods is a panacea, so that the art of engineering is not to choose the best one, but to combine many of them in an educated way – corresponding to their potentials and limitations. Such combinations and scale transitions have already a remarkable record of success, demonstrating, for example, the strong interconnection that exists between drying and product formulation in the considered class of processes. It is expected that the development described in this chapter will continue in the years to come, towards better products and more efficient processes.

Additional Notation Used in Chapter 7

a	maximal size of defects	m
a	separation distance	m
a	base radius of deposited droplet	m
E	modulus of elasticity	$\mathrm{N\,m^{-2}}$
e	restitution coefficient	–
F	force	N
F	frequency pre-factor	$\mathrm{m^{-1}}$
f	frequency	$\mathrm{s^{-1}}$
G	growth rate	$\mathrm{m\,s^{-1}}$
h	height	m
K	coordination number	–
k	stiffness	$\mathrm{N\,m^{-1}}$
$\dot{N}$	particle flow density	$\mathrm{m^{-1}\,s^{-1}}$
n	number density	$\mathrm{m^{-1}}$
P	probability	–

P	production density	$m^{-1}\,s^{-1}$
R	agglomeration rate	$m\,s^{-1}$
s	meniscus radius of liquid bridge	m
s	displacement	m
T_g	glass transition temperature	K, °C
W_m	mass-related energy consumption	$J\,kg^{-1}$
w	water mass fraction (wet-based water content)	–
x	diameter of contact area, liquid bridge	m

Greek Letters

α	volume fraction of spraying zone	–
β	mass transfer coefficient	$m\,s^{-1}$
β	momentum transfer coefficient	$kg\,m^{-3}\,s^{-1}$
β	angle covered by liquid bridge	rad
γ	surface tension	$N\,m^{-1}$
γ	droplet addition rate	s^{-1}
$\dot{\gamma}$	shear rate	s^{-1}
θ	contact angle	rad
λ	superposition weight factors	–
υ	Poisson's ratio	–
σ	normal stress	Pa
τ	residence time	–

Subscripts and Superscripts

a	asperity
ad	droplet addition
agg	agglomerate
B	breakage point
b	binder
br	bridge
cap	spherical cap (deposited droplet)
coal	coalescence
coll	collision
cyl	cylindrical
d	droplet
diss	dissolved
dry	drying
el	elastic
F	yield point
gap	gap
kin	kinetic

imb	imbibition
N	normal
pore	pore
pl	plastic
pp	particle–particle
R	rebound
r	reduced
real	real time
step	time step
sus	solids in suspension
T	tangential
t	tensile
vdW	van der Waals
0	initial
0	superficial

Abbreviations

CFD	computational fluid dynamics
CSTR	continuous stirred tank reactor
CVMC	contact volume Monto Carlo
DE	dextrose equivalent
DEM	discrete element method
DPM	discrete particle model
FB	fluidized bed
HPMC	hydroxypropyl-methylcellulose
MC	Monte Carlo
PBE	population balance equation
PSD	particle size distribution
RH	relative humidity
SB	spouted bed

References

Aguilera, J., Levi, G., Karel, M., 1993. Effect of water content on the glass transition and caking of fish protein hydrolysates. *Biotechnol. Prog.* **9**: 651–654.

Antonyuk, S., Tomas, J., 2008. Deformation and breakage behaviour of dry cylindrical agglomerates. *Proceedings of 4th International Symposium on Reliable Flow of Particulate Solids*, Tromsø, Norway, 507–512.

Antonyuk, S., Heinrich, S., Tomas, J., Deen, N. G., van Buijtenen, M. S., Kuipers, J. A. M., 2010. Energy absorption during compression and impact of dry elastic-plastic spherical granules. *Granular Matter* **12**(1): 15–47.

Antonyuk, S., Palis, S., Heinrich, S., 2011. Breakage behavior of agglomerates and crystals by static loading and impact. *Powder Technol.* **206**: 88–98.

Antonyuk, S., Khanal, M., Tomas, J., Heinrich, S., Mörl, L., 2006. Impact breakage of spherical granules: Experimental study and DEM simulation. *Chem. Eng. Process.* **45**: 838–856.

Avar, B. B., Hudyma, N., Karakouzian, M., 2003. Porosity dependence of the elastic modulus of lithophysae-rich tuff: Numerical and experimental investigations. *Int. J. Rock Mech. Min.* **40**: 919–928.

Bärmann, F., Biegler-König, F., 1992. On a class of efficient learning algorithms for neural networks. *Neural Networks* **5**: 139–144.

Baker, C. G. J., Lababidi, H. M. S., 2010. An improved model of plug-flow fluidized bed dryers with an emphasis on energy conservation. *Drying Technol.* **28**: 730–741.

Beetstra, R., van der Hoef, M. A., Kuipers, J. A. M., 2007. Drag force from lattice Boltzmann simulations of intermediate Reynolds number flow past mono- and bidisperse arrays of spheres. *AIChE J.* **53**(2): 489–501.

Bika, D., Tardos, G. I., Panmai, S., Farber, L., Michaels, J., 2005. Strength and morphology of solid bridges in dry granules of pharmaceutical powders. *Powder Technol.* **150**: 104–116.

Boccaccini, A. R., 1994. *Zur Abhängigkeit der mechanischen Eigenschaften zweiphasiger und poröser Werkstoffe von der Gefüge-bzw. Porositätsstruktur.* Diss., RWTH Aachen, Germany.

Braspenning, P. J., Thuijsman, F., Weijters, A. J. M. P. (eds), 1995. *Artificial neural networks.*, Springer, Berlin, Germany.

Briscoe, B. J., Luckham, P. F., Maung, R., Aydin, I., 1998. Nano and micro-mechanics of agglomerates. *Proceedings of 3rd World Congress on Particle Technology,* Brighton, UK.

Buffière, P., Moletta, R., 2000. Collision frequency and collisional particle pressure in three-phase fluidized beds. *Chem. Eng. Sci.* **55**: 5555–5563.

Coelho, D., Thovert, J.-F., Adler, P. M., 1997. Geometrical and transport properties of random packings of spheres and spherical particles. *Phys. Rev. E* **55**: 1959–1977.

Deen, N. G., van Sint Annaland, M., van der Hoef, M. A., Kuipers, J. A. M., 2007. Review of discrete particle modelling of fluidized beds. *Chem. Eng. Sci.* **62**: 28–44.

Desportes, S., Steinmetz, D., Hemati, M., Philippot, K., Chaudret, B., 2005. Production of supported asymmetric catalysts in a fluidised bed. *Powder Technol.* **157**: 12–19.

Downtown, G., Flores-Luna, J., King, C., 1982. Mechanism of stickiness in hygroscopic, amorphous powders. *Ind. Eng. Chem. Fundam.* **21**: 447–451.

Ennis, B. J., Tardos, G., Pfeffer, R., 1991. A microlevel-based characterization of granulation phenomena. *Powder Technol.* **65**: 257–272.

Erbil, H. Y., McHale, G., Newton, M. I., 2002. Drop evaporation on solid surfaces: Constant contact angle mode. *Langmuir* **18**: 2636–2641.

Ferry, J., 1980. *Visco-elastic properties of polymers.* 3rd edn, Wiley & Sons, New York, USA.

Fisher, R. A., 1926. On the capillary forces in an ideal soil. *J. Agric. Sci.* **16**: 492–505.

Frenkel, J., 1945. Viscous flow of crystalline bodies under action of surface tension. *J. Phys. (USSR)* **9**(5): 385–391.

Fyhr, C., Kemp, I. C., Wimmerstedt, R., 1999. Mathematical modeling of fluidized bed dryers with horizontal dispersion. *Chem. Eng. Process.* **38**: 89–94.

Goldschmidt, M. J. V., Kuipers, J. A. M., 2003. Discrete element modelling of fluidised bed spray granulation. *Powder Technol.* **138**: 39–45.

Gordon, M., Taylor, J. S., 1952. Ideal copolymers and the second order transitions of synthetic rubbers, Part 1: Non-crystalline copolymers. *J. Appl. Chem.* **2**: 493–500.

Haibo, Z., Chuguang, Z., Minghou, X., 2005. Multi-Monte Carlo approach for general dynamic equation considering simultaneous particle coagulation and breakage. *Powder Technol.* **154**: 164–178.

Hamaker, H., 1937. The London-van der Waals attraction between spherical particles. *Physica* **4**(10): 1058–1072.

Hede, P. D., Bach, P., Jensen, A. D., 2009. Batch top-spray fluid bed coating: Scale-up insight using dynamic heat- and mass-transfer modeling. *Chem. Eng. Sci.* **64**: 1293–1317.

Hemati, M., Cherif, R., Saleh, K., Pont, V., 2003. Fluidized bed coating and granulation: Influence of process-related variables and

physicochemical properties on the growth kinetics. *Powder Technol.* **130**: 18–34.
Hemati, M., Steinmetz, D., Chaudret, B., Philippot, K., 2001. Fabrication de catalyseur d'un nouveau type par imprégnation en lit fluidisé. *Brevet EPI-PCT* 2001, FR 02, 01795.
Hertz, H., 1882. Über die Berührung fester elastischer Körper. *J. für Reine und Angew. Mathematik* **92**: 156–171.
Hill, R. J., Koch, D. L., Ladd, J. C., 2001. Moderate-Reynolds-numbers flows in ordered and random arrays of spheres. *J. Fluid Mechanics* **448**: 243–278.
Hoffmann, T., Hailu Bedane, A., Peglow, M., Tsotsas, E., Jacob, M., 2011. Particle-gas mass transfer in a spouted bed with adjustable air inlet. *Drying Technol.* **29**: 257–265.
Hoffmann, T., Peglow, M., Tsotsas, E., 2010. Dynamic behaviour of particle-size distribution in fluidized bed granulation. *Proceedings of the 6th World Congress on Particle Technology,* Nürnberg.
Hoomans, B. P. B., Kuipers, J. A. M., Briels, W. J., van Swaaij, W. P. M., 1996. Discrete particle simulation of bubble and slug formation in a two-dimensional gas-fluidised bed: A hard-sphere approach. *Chem. Eng. Sci.* **51**(1): 99–118.
Iveson, S. M., Page, N. W., 2001. Tensile bond strength development between liquid-bound pellets during compression. *Powder Technol.* **117**: 113–122.
Jacob, M., 2007. Granulation equipment, in *Handbook of powder technology: Granulation* (eds A. D. Salman, M. J. Hounslow, J. P. K. Seville). Elsevier, Amsterdam, Holland, Vol. 11, Chapter 9, 417–476.
Jacob, M., 2009. ProCell technology: Modelling and application. *Powder Technol.* **189**: 332–342.
Kafui, D. K., Thornton, C., 2008. Fully-3D DEM simulation of fluidised bed spray granulation using an exploratory surface-energy based spray zone concept. *Powder Technol.* **184**: 177–188.
Kendall, K., McAlford, N., Birchall, J. D., 1987. Elasticity of particle assemblies as a measure of the surface energy of solids. *Proc. R. Soc. London, Ser. A* **412**(1843): 269–283.
Khanal, M., Schubert, W., Tomas, J., 2008. Compression and impact loading experiments of high strength spherical composites. *Int. J. Miner. Process.* **86** (1–4): 104–113.
Kuczynski, G. C., 1949. Self-diffusion in sintering of metallic particles. *Trans. AIME* **185**: 169–178.
Lifshitz, E. 1956. The theory of molecular attraction forces between solids. *Sov. Phys. (JETP)* **2**(1): 73–83.
Markovitz, H., 1975. Superposition in rheology. *J. Polym. Sci., Polym. Symp.* **50**: 431–456.
Mindlin, R. D., Deresiewicz, H., 1953. Elastic spheres in contact under varying oblique forces. *Trans. ASME, Ser. E, J. Appl. Mechanics* **20**: 327–344.
Mörl, L., Heinrich, S., Krüger, G., Ihlow, M., Jordanova, E., 2002. *Steuerbare Gasanströmeinrichtung für Strahlschichtapparate*. German Patent No. 100 04 939.7-41.
Mörl, L., Heinrich, S., Peglow, M., 2007. Fluidized bed spray granulation, in *Handbook of powder technology: Granulation* (eds A. D. Salman, M. J. Hounslow, J. P. K. Seville). Elsevier, Amsterdam, Holland, Vol. 11, pp. 21–188.
Nilsson, L., Wimmerstedt, R., 1988. Residence time distribution and particle dispersion in a longitudinal-flow fluidized bed. *Chem. Eng. Sci.* **43**: 1153–1160.
Palzer, S., 2005. The effect of glass transition on the desired and undesired agglomeration of amorphous food powders. *Chem. Eng. Sci.* **60**: 3959–3968.
Palzer, S., 2009. Influence of material properties on the agglomeration of water-soluble amorphous particles. *Powder Technol.* **189**: 318–326.
Pepin, X., Simons, S. J. R., Blachon, S., Rossetti, D., Couarraze, G., 2001. Hardness of moist agglomerates in relation to interparticle friction, granule liquid content and nature. *Powder Technol.* **117**: 123–138.
Pierrat, P., Caram, H. S., 1997. Tensile strength of wet granular materials. *Powder Technol.* **91**: 83–93.
Rabinovich, Y., Esayanur, M., Moudgil, B., 2005. Capillary forces between two spheres with a fixed volume liquid bridge: Theory and experiment. *Langmuir* **21** (24): 10992–10997.

Ramkrishna, D., 1981. Analysis of population balance, Part 4: The precise connection between Monte Carlo simulation and population balances. *Chem. Eng. Sci.* **36**: 1203–1209.

Roos, Y., Karel, M., 1991. Plasticising effect of water on thermal behaviour and crystallization of amorphous food models. *J. Sci.* **56**(1): 38–43.

Rumpf, H., 1958. Grundlagen und Methoden des Granulierens. *Chem.-Ing.-Tech.* **30** (3): 144–158.

Rumpf, H., 1970. Zur Theorie der Zugfestigkeit von Agglomeraten bei Kraftübertragung an Kontaktpunkten. *Chem.-Ing.-Tech.* **42**(8): 538–540.

Rumpf, H., Sommer, K., Steier, K., 1976. Mechanismen der Haftkraftverstärkung bei der Partikelhaftung durch plastisches Verformen, Sintern und viskoelastisches Fliessen. *Chem.-Ing.-Tech.* **48**(4): 300–307.

Salman, A. D., Fua, J., Gorham, D. A., Hounslow, M. J., 2003. Impact breakage of fertiliser granules. *Powder Technol.* **130**: 359–366.

Samimi, A., Ghadiri, M., Boerefijn, R., Groot, A., Kohlus, R., 2003. Effect of structural characteristics on impact breakage of agglomerates. *Powder Technol.* **130**: 428–435.

Schatt, W., 1992. *Sintervorgänge: Grundlagen*. VDI Verlag, Düsseldorf, Germany.

Schubert, H., 1975. Tensile strength of agglomerates. *Powder Technol.* **11**: 107–119.

Schubert, H., 1979. Grundlagen des Agglomerierens. *Chem.-Ing.-Tech.* **151**(4): 266–277.

Shah, B. H., Ramkrishna, D., Browanker, J. D., 1977. Simulation of particulate system using the concept of the interval of quiescence. *AIChE J.* **23**: 897–904.

Silva, D. O., Tamiozzo, L. M., Duarte, C. R., Murata, V. V., Barrozo, M. A. S., 2011. Modeling of seed coating in spouted bed. *Drying Technol.* **29**(3) 286–294.

Simon, M., Iveson, S. M., Litster, J. D., Hapgood, K., Ennis, B. J., 2001. Nucleation, growth and breakage phenomena in agitated wet granulation processes: A review. *Powder Technol.* **117**: 3–39.

Slade, L., Levine, H., 1991. Beyond water activity: Recent advances based on an alternative approach to the assessment of food quality and safety. *Crit. Rev. Food Sci. Nutr.* **30**(2–3): 115–360.

Smith, W. O., Foote, P. D., Busang, P. F., 1929. Packing of homogeneous spheres. *Phys. Rev.* **34**: 1271–1274.

Sperling, L., 1986. *Introduction to physical polymer science*. Wiley & Sons, New York, USA, pp. 224–295.

Stepanek, F., Rajniak, P., 2006. Droplet morphologies on particles with macroscopic surface roughness. *Langmuir* **22**: 917–923.

Stepanek, F., Rajniak, P., Mancinelli, C., Chern, R., Ramachandran, R., 2009. Distribution and accessibility of binder in wet granules. *Powder Technol.* **189**: 376–384.

Terrazas-Velarde, K., 2010. *Monte Carlo simulation of fluidized bed spray agglomeration*. Diss., Otto von Guericke University Magdeburg, Germany.

Terrazas-Velarde, K., Peglow, M., Tsotsas, E., 2009. Stochastic simulation of agglomerate formation in fluidized bed spray drying: A micro-level approach. *Chem. Eng. Sci.* **64**: 2631–2643.

Terrazas-Velarde, K., Peglow, M., Tsotsas, E., 2011. Investigation of the kinetics of fluidized bed spray agglomeration based on stochastic methods. *AIChE J.*, doi: 10.1002/aic.12506

Tomas, J., 1983. *Untersuchungen zum Fließverhalten von feuchten und leichtlöslichen Schüttgütern*. Diss., Freiberger Forschungsheft A677, Germany.

Tomas, J., Schreier, M., Gröger, T., Ehlers, S., 1999. Impact crushing of concrete for liberation and recycling. *Powder Technol.* **105**: 39–51.

Tsuji, Y., Tanaka, T., Ishida, T., 1992. Lagrangian numerical simulation of plug flow of cohesionless particles in a horizontal pipe. *Powder Technol.* **71**: 239–250.

Tsuji, Y., Kawaguchi, T., Tanaka, T., 1993. Discrete particle simulation of two-dimensional fluidized bed. *Powder Technol.* **77**(1): 79–87.

Wagner, T., 1997. *Kaltsprühen ein- und mehrphasiger Flüssigkeiten*. Diss., ETH Zürich, Switzerland.

Wallack, D., King, C., 1988. Sticking and agglomeration of hygroscopic, amorphous carbohydrates and food powders. *Biotechnol Prog.* **4**: 31–35.

Weisser, H., 1986. Influence of temperature on sorption isotherms, in *Transport Phenomena* (eds M. Maguer, P. Jelen). Elsevier, London, UK.

Wen, Y. C., Yu, Y. H., 1966. Mechanics of fluidization. *Chem. Eng. Progr. Symp. Series.* **62**: 100–111.

Willett, C. D., Johnson, S. A., Adams, M. J., Seville, J. P. K., 2007. Pendular capillary bridges, in *Handbook of powder technology: Granulation* (eds A. D. Salman, M. J. Hounslow, J. P. K. Seville). Elsevier, Amsterdam, Holland, Vol. 11, pp. 1317–1351.

Williams, M. L., Landel, R. F., Ferry, J. D., 1955. The temperature dependence of relaxation mechanisms in amorphous polymers and other glass-forming liquids. *J. Am. Chem. Soc.* **77** (14): 3701–3707.

Wurster, D. E., 1959. Air suspension technique of coating drug particles. *J. Am. Pharm. Assoc.* **48**: 451–454.

Yang, R. Y., Yu, A. B., Choi, S. K., Coates, M. S., Chan, H. K., 2008. Agglomeration of fine particles subjected to centripetal compaction. *Powder Technol.* **184** (1): 122–129.

Zhao, H., Maisels, A., Matsoukas, T., Zheng, C. G., 2007. Analysis of four Monte Carlo methods for the solution of population balances in dispersed systems. *Powder Technol.* **173**: 38–50.